A Search for $t\bar{t}$ Resonances in the Single Lepton Final State with the ATLAS Experiment

Andrew Altheimer

Submitted in partial fulfillment of the
requirements for the degree
of Doctor of Philosophy
in the Graduate School of Arts and Sciences

COLUMBIA UNIVERSITY

2014

ABSTRACT

A Search for $t\bar{t}$ Resonances in the Single Lepton Final State with the ATLAS Experiment

Andrew Altheimer

A search for undiscovered particles decaying into top-antitop quark pairs produced in proton-proton collisions with the ATLAS experiment at the Large Hadron Collider utilizing 20.3 fb^{-}1 of data collected at $\sqrt{s}$ = 8 TeV center-of-mass energy during the 2012 data taking period is presented. The invariant mass spectrum of events containing multiple jets, exactly one lepton, and missing transverse energy and which are consistent with the decay of a top-antitop quark pair is studied and found to be consistent with that predicted by the Standard Model. Upper limits on the production cross section times branching ratio of several benchmark signal models are set at a 95% confidence level.

Table of Contents

List of Figures **v**

List of Tables **xi**

1 The Standard Model **1**

1.1 Fermions 4

1.2 Gauge Bosons and Fundamental Forces 5

1.2.1 Electroweak Theory and the Higgs Sector 5

1.3 Strong Nuclear Force and Confinement 8

1.4 Top Quark 9

2 $t\bar{t}$ Resonances and Physics Beyond the Standard Model **11**

2.1 Topcolor Z' Model 12

2.2 Randall-Sundrum Models and Kaluza-Klein Bosons 13

3 The Large Hadron Collider **18**

3.1 LHC Layout and Injector Chain 18

3.2 The LHC Machine 20

3.2.1 Radio-Frequency Cavities 20

3.2.2 Superconducting Magnets 20

3.3 Beam Characteristics 21

4 The ATLAS Detector **24**

4.1 The Inner Detector 26

4.1.1 The Pixel Detector and the Semi-Conductor Tracker 27
4.1.2 Transition Radiation Tracker 29
4.2 Calorimeters 30
4.2.1 Particle Showers 31
4.2.2 Liquid Argon Calorimeter 32
4.2.3 Tile Calorimeter 37
4.3 Muon System 38
4.3.1 Precision Muon System 39
4.3.2 Muon Trigger System 41
4.4 Magnets 42
4.5 Forward Detectors 44
4.6 Trigger and Data Acquisition System 44

5 Object Identification and Reconstruction 47

5.1 Tracks and Vertices 47
5.2 Electrons 48
5.3 Photons 50
5.4 Muons 50
5.5 Jets 51
5.5.1 Jet Algorithms 51
5.5.2 Jet Selection 53
5.5.3 *b*-tagging 55
5.5.4 Jet Substructure 55
5.5.5 Jet Trimming 57
5.6 Missing Transverse Energy 59
5.7 Electron-Jet Subtraction and Object Overlap Removal 61

6 Data Taking and Preparation 63

7 Monte Carlo and Physics Simulation 66

7.1 Monte Carlo Generators 67

8 Event Selection and Reconstruction **69**

8.1 Preselection 69

8.2 Leptonic W Boson Reconstruction 72

8.3 Resolved Channel: Selection and Event Reconstruction 72

8.3.1 χ^2 Algorithm 73

8.3.2 Reconstruction Efficiency 76

8.4 Boosted Channel: Selection and Reconstruction 77

9 Background Estimation **81**

9.1 W+Jets Background Estimation 82

9.1.1 W+jets Normalization 83

9.1.2 W+jets Flavor Composition 83

9.2 MultiJet Background Estimate 85

9.2.1 Lepton Efficiency and Fake Rates 88

9.2.2 Matrix Method 93

9.3 Comparison of Data and Expected Backgrounds 93

10 Signal Characteristics **98**

11 Systematic Uncertainties and Corrections **103**

11.1 General Uncertainties 103

11.2 Uncertainties on Data Driven Background Estimates 104

11.3 Uncertainties Impacting the Modeling of the SM $t\bar{t}$ Background 105

11.4 b-tagging Efficiency Scale Factors and Uncertainties 106

11.5 Other Uncertainties on Reconstructed Objects 107

11.6 Summary of Systematic Treatment and Impact 108

12 Results **111**

12.1 Compatibility with the Standard Model 111

12.2 Upper Limits on $t\bar{t}$ Resonance Production Cross Sections 113

12.3 Conclusions and Outlook 122

Bibliography **122**

List of Figures

1.1 Diagram of the fundamental particles of the SM. 2

1.2 Several example Feynman diagrams showing several of the lowest order terms in the production of a top-antitop quark pair from a pair of incoming light quarks or gluons. 3

1.3 Potential energy of the Higgs Field as a function of its value. Its unusual shape gives rise to a non-zero vacuum expectation value which was determined by spontaneous symmetry breaking in the very early universe. . 6

1.4 Feynman diagram showing the decay of a top quark to a bottom quark plus an anti-electron/neutrino pair. 7

1.5 Several example Feynman diagrams showing several of the lowest order terms in the production of a single top quark. 10

2.1 The branching ratios for a topcolor leptophobic Z' boson to decay to each of four flavors of quark/anti-quark pairs in the chosen benchmark model. . . . 14

2.2 The branching ratios for the chosen Bulk-RS KKG benchmark model. . . . 17

3.1 Layout of the LHC and the Injector Chain. Protons are accelerated through the Linac 2 linear accelerator, followed by the Proton Synchrotron Booster, Proton Synchrotron, and the Super Proton Synchrotron. 19

3.2 Schematic detailing the function of an RF cavity. Oscillating electromagnetic fields accelerate proton bunches. 20

4.1 Layout of the ATLAS detector and main sub-components. 25

4.2 Layout of the ATLAS inner detector 27

4.3 Layout of the ATLAS Calorimeter, outside of the ID and solenoid magnets. 31
4.4 Example calorimeter showers instigated by energetic particles in the calorimeter. In the top half of the figure, an incoming electron produces a shower of electrons (solid red lines) and photons (squiggly pink lines.) In the bottom half, a proton initiates a shower of hadronic material (green lines) with each pink oval representing an interaction with the absorber material. A muon is also produced by the decay of a heavy meson. Image thanks to David Bailey at the University of Toronto. 33
4.5 The LAr accordion structure ensures multiple crossings between the active medium and the heavy absorber. 34
4.6 Layout of the ATLAS Liquid Argon EM Calorimeter, showing the three main layers in the Barrel. 35
4.7 Left: total material in front of the presampler and the main electromagnetic calorimeter. Calorimetry resolution is reduced in the crack region between the barrel and endcaps due to the large amount of material there. Right: Depth of each calorimeter layer in the barrel region. 36
4.8 Depth of the calorimeters in terms of the hadronic interaction length 36
4.9 Shape of the output signal in the LAr detector, before and after shaping. . 37
4.10 Layout of the Muon System. Left: Cross section of the barrel perpendicular to the beam axis. Right: Cross section of the muon system along the beam axis. Green and blue boxes represent the MDT, while the CSC is shown in yellow. The muon trigger system is also shown. 40
4.11 Left: Layout of the ATLAS magnets, including the solenioid as well as the barrel and endcap toroids. Right: The ATLAS barrel toroid, before installation of other subsystems. 43
4.12 Layout of the three main forward detectors on ATLAS. 43

5.1 A cross section of the ATLAS detector showing the response of the various subdetectors to observable physics object which may be produced in a collision. Taken in aggregate, the data produced by these subdetectors may be used to identify the nature of these particles. 48

5.2 The resulting jet areas produced by several jet algorithms on the same parton-level event. 54
5.3 b-tagging background rejection shown as a function of efficiency. 56
5.4 Illustration of the jet trimming procedure. 58
5.5 Jet mass as a function of vertex multiplicity before and after applying jet trimming. 59
5.6 Impact of jet trimming on jet mass and Split12/ 60
5.7 Comparison of the leading jet mass between data and Monte Carlo before and after trimming. 60

6.1 Left: Integrated luminosity of proton-proton collisions delivered to and recorded by the ATLAS detector during 2012, as well as the portion considered of high quality for physics analyses. Right: Mean number of interactions per crossing, μ, weighted according to luminosity. The average number of collisions per crossing varies over time, between fills, and between individual proton bunch crossings in a given fill. 64

8.1 Lepton Trigger efficiencies for a SM $t\bar{t}$ sample. 70
8.2 Efficiency of the large-R jet trigger on events passing an inclusive jet selection. Differences between SM $t\bar{t}$ and multijet events (Pythia8) are due to differences in the jet shapes and the use of a smaller jet radius in the level 2 trigger. 71
8.3 Ratio of efficiencies when using lepton triggers only compared to the combination of lepton triggers and the large-R jet trigger. Large-R jet trigger efficiency has been adjusted to reflect the fact that it is available for only 17.3 fb^{-1} of data. 71
8.4 Reconstructed $m_{t\bar{t}}$ compared to the true $t\bar{t}$ invariant mass for simulated SM $t\bar{t}$ events reconstructed with the χ^2 algorithm. 75
8.5 Difference between the true and reconstructed invariant mass for simulated Z' bosons reconstructed with the χ^2 algorithm. 76

8.6 Fraction of semileptonic $t\bar{t}$ events which are determined to be reconstructable (i.e. those for which all truth level objects can be matched to reconstructed object). Also shown is the matching efficiency to hadronically and leptonically decaying top quarks and W bosons individually. 77
8.7 Efficiency to select the correct combination of jets in reconstructable events which pass the resolved selection but fail the boosted selection, by signal type and resonance mass. 78
8.8 Selection efficiency for a Z' boson as a function of the true $m_{t\bar{t}}$ of each event. 80

9.1 Number of events in each jet multiplicity bin in data and background estimates. Shown before (left) and after (right) applying heavy flavor and normalization scale factors to the W+jets background. Exclusive (ex) jet bins include all events containing a particular number of jets, while inclusive (in) jet bins include events containing a minimum number of events. No b-tagging requirement has been applied. 86
9.2 Number of events in each jet multiplicity bin in data and background estimates. Shown before (left) and after (right) applying heavy flavor and normalization scale factors to the W+jets background. At least one b-tagged jet is required. 87
9.3 Efficiencies for loose electrons and muons to be identified as tight in the resolved selection. 90
9.4 Efficiencies for loose electrons and muons to be identified as tight in the boosted selection. 90
9.5 Fake rates for non-prompt loose electrons and muons to be identified as tight in the resolved selection. A one-dimensional parameterization of the fake rate for muons with $\Delta R(\mu, jets) > 0.4$ is used due to inadequate statistics. 91
9.6 Fake rates for non-prompt loose electrons and muons to be identified as tight in the boosted selection. A one-dimensional parameterization of the fake rate for muons with $\Delta R(\mu, jets) > 0.4$ is used due to inadequate statistics. . . . 92
9.7 $m_{t\bar{t}}$ distributions of events containing tight leptons in the $CR0$ control region. 94

9.8 $m_{t\bar{t}}$ distributions of events in the resolved selection. Categories 1, 2 and 3 contain events in which b-tagged jets are associated to both the hadronically and leptonically decaying top quarks, only the hadronically decaying top quark, or only to the leptonically decaying top quark respectively. Systematic and Monte Carlo statistical uncertainties are shown on the background estimates. 96

9.9 $m_{t\bar{t}}$ distributions of events in the boosted selection. Categories 1, 2 and 3 contain events in which b-tagged jets are associated to both the hadronically and leptonically decaying top quarks, only the hadronically decaying top quark, or only to the leptonically decaying top quark respectively. Systematic and Monte Carlo statistical uncertainties are shown on the background predictions. 97

10.1 Mass distributions of generated Z' resonances (red) and the invariant masses of the associated top quarks. The most massive signals prefer to be produced off the mass shell due to the steeply falling PDFs. The difference between the mass of the Z' boson and that of the produced top quark pair is due to final state radiation emitted by those top quark. 99

10.2 Mass distributions of generated KKg resonances (red) and the invariant masses of the associated top quarks. The most massive signals prefer to be produced off the mass shell due to the steeply falling PDFs. The difference between the mass of the KKg and that of the produced top quark pair is due to final state radiation emitted by those top quark. 100

10.3 Shape of the reconstructed $t\bar{t}$ invariant mass expected from a Z' signal for several resonance masses. 101

10.4 Shape of the reconstructed $t\bar{t}$ invariant mass expected from a KKg signal for several resonance masses and widths. 102

11.1 Left: Impact of b-tagging scale factors on the event yield for several Z' samples before applying b-tagging or the χ^2 cut in the resolved selection. Right: b-tagging efficiency measured in Monte Carlo as a function ΔR_{Jfit} compared to the officially estimated efficiency determined by the η and p_T of a jet. 108

12.1 Observed vs expected $m_{t\bar{t}}$ distributions of events after fitting the systematic nuissance parameters to the observed data. Events are summed over all resolved channels (a), all boosted channels (b), and the combination of resolved and boosted channels (c). Also shown is the expected contribution from a 2 TeV Z'. 112

12.2 Best fit values of the nuisance parameters and their uncertainties. 0 denotes the nominal value of each systematic. 114

12.3 Correlation between nuissance parameters in a background only maximum likelihood fit. 115

12.4 Data and expected backgrounds before and after performing maximum likelihood fit in the resolved channel. 116

12.5 Data and expected backgrounds before and after performing maximum likelihood fit in the boosted channel. 117

12.6 Expected and observed upper limits on the cross sections times $t\bar{t}$ branching ratios of the chosen benchmark models. Both the resolved and boosted channels are considered, and both systematic and statistical uncertainties are accounted for. 119

12.7 Expected and observed upper limits on the cross sections times $t\bar{t}$ branching ratios of the chosen benchmark models. Only the resolved channels are considered. Both systematic and statistical uncertainties are accounted for. 120

12.8 Expected and observed upper limits on the cross sections times $t\bar{t}$ branching ratios of the chosen benchmark models. Only the boosted channels are considered. Both systematic and statistical uncertainties are accounted for. 121

List of Tables

2.1 Cross sections times branching ratios of the benchmark Z' model for proton-proton collision at an 8 TeV center of mass energy assuming a width of 1.3%. A K-factor of 1.3 is applied to the cross section to account for next to leading order terms. 13

2.2 Cross sections times branching ratios of the benchmark KKg models for proton-proton collision at an 8 TeV center of mass energy. 15

2.3 Widths and cross sections times branching ratios of the benchmark KKG model for several masses for proton-proton collision at an 8 TeV center of mass energy. 16

4.1 Summary of the design performance and coverage of the inner detector. *Each point in the SCT Barrel consists of a double-layer hit. **Each track is expected to hit an average of 36 straw tubes. 28

4.2 Summary of the coverage of the electromagnetic and hadronic calorimetry systems. *LAr presampler more closely resembles a tracker than a calorimeter due to the absence of an absorber. 38

4.3 Summary of the coverage and performance of the Muon System. Resolution is shown for a single muon chamber. 42

8.1 Summary of parameters used in the χ^2 formula used to reconstruct $t\bar{t}$ candidates in the resolved channel. Values reflect the mean and standard deviation of observed quantities in simulated Z' samples with a range of masses. 74

9.1 W+jets normalization scale factors derived via the charge asymmetry method. 84
9.2 W+jets heavy flavor scale factors. 85
9.3 Data and expected background yields after the full resolved or boosted selection. The associated systematic uncertainties on the yields are also shown. 95

11.1 Impacts of the systematic uncertainty on the multijet background, in the resolved channel. 104
11.2 Impacts of the systematic uncertainty on the multijet background, in the boosted channel. 105
11.3 Impact of considered systematics on the expected yield of each background and on a 1.5 TeV Z' boson in the resolved channel. 109
11.4 Impact of considered systematics on the expected yield of each background and on a 1.5 TeV Z' boson in the boosted channel. 110

Acknowledgments

I would like to thank my supervisor Gustaaf Brooijmans has provided me with years of support, guidance. He has given me many opportunities to work on interesting projects and to challenge myself. In addition, I valued the advice and guidance offered by many members of the Columbia ATLAS group, especially Emily Thompson and Tim Andeen.

I am also grateful to all my colleagues on the $t\bar{t}$ resonance search team, but most especially to Jiahang Zhong for his excellent mentorship. In addition, I feel very fortunate to have worked with the Liquid Argon detector operations team, whose dedication to the smooth operation of the detector is matched only by their welcoming attitude and eagerness to challenge newcomers. I would particularly like to thank Nikiforos Nikiforou who provided me with the countless hours of hands on training in the LAr control room during his time as a graduate student at Columbia.

I would also like to mention those individuals who provided me with mentorship during earlier years of my life. This includes Karl Ecklund, Paul Padley, Jabus Roberts, and Alex Tumanov who offered me advice and guided me through various research opportunities during my time at Rice University. Thanks also to my high school physics teacher Spike Peterson, who challenged and inspired me and with whom I built my first particle detector.

Finally, I would like to give a heartfelt thanks to my parents who have provided me with years of love and support. Without them, I could not be where I am today.

To my parents.

Chapter 1

The Standard Model

Modern particle physics describes the structure of all understood forms of matter in terms of a handful of fundamental particles. Formulated in the early 1970's as a synthesis of theoretical developments over preceding decades, the Standard Model (SM) describes the interactions between these particles in terms of a handful of fundamental forces. Since then, the SM has been used to explain a huge range of physical phenomena, and its successful predictions include the discovery of the top quark in 1995 [1; 2], the tau neutrino in 2000 [3] and the Higgs Boson in 2012 [4; 5]. To date, the SM is the most precisely tested scientific theory ever created, with a range of measurements agreeing with theoretical predictions to an amazing level of precision.[1] The SM is not only our best current description of the fundamental laws of particle physics, but also an underlying framework for future developments in the field.

The Standard Model posits that all understood forms of matter are composed of a limited number of fundamental particles with half integer spin, referred to as fermions. In addition to the fermions, bosons carry integer spin values and perform important functions in the theory. Interactions between particles are mediated by the gauge bosons which are generated by a local gauge invariance built into the theory. These gauge bosons explain all of

[1]For example, the measurement of the anomalous magnetic moment of the electron stands out as one of the high points of the theory, having been measured to 10 digits of accuracy [6]. This is one of many precise measurements which have been made which depends on the fine structure constant. These measurements are in good agreement with each other and with the theory.

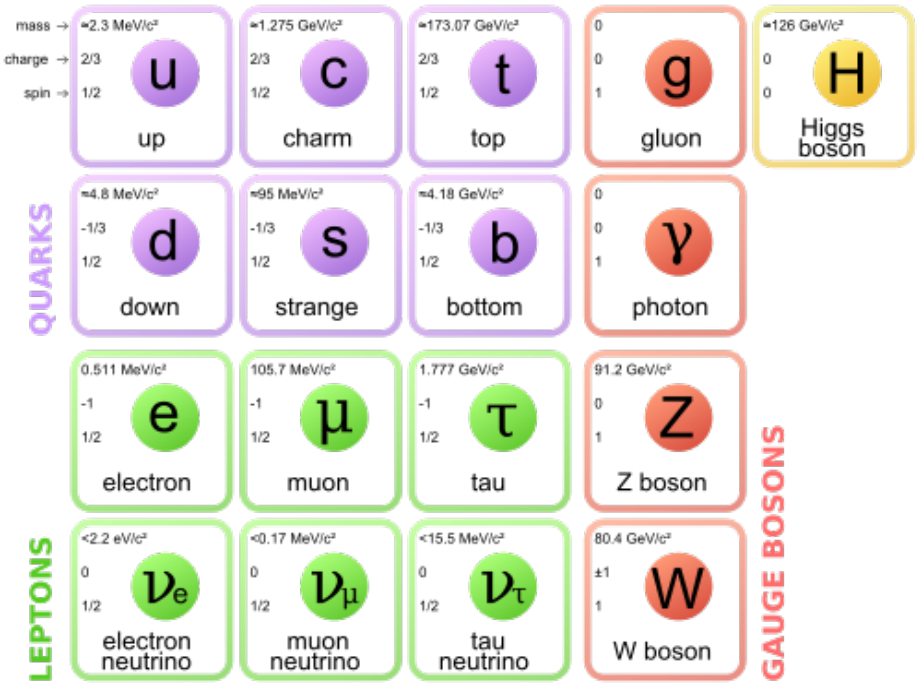

Figure 1.1: Diagram of the fundamental particles of the SM.

the known forces of nature except for gravity.[2] Furthermore, the Higgs boson is believed to be responsible for generating the mass of other particles in the SM. A particle's spin, which behaves like an intrinsic angular momentum, is of fundamental importance in describing the behavior of these particles, a consequence of the Spin-Statistic Theorem which states that particle states must always be anti-symmetric about the exchange of two fermions and symmetric about the exchange of two bosons [7]. Figure 1.1 shows the fundamental particles which form the basic building blocks of the Standard Model.

The Standard Model is an example of a quantum field theory (QFT) which describes fundamental particles as quantized excitations of fields. These fields can in turn be described by complex non-abelian operators. Of central importance in the Standard Model, or indeed any QFT, is the Lagrangian, the analogue of the classical concept first described by Joseph Louis Lagrange in 1788. In principle, the Lagrangian encapsulates all of the knowledge

[2] Attempts to integrate General Relativity, the best current description of gravity, into the framework of the SM in four dimensions produce non-renomalizable divergences.

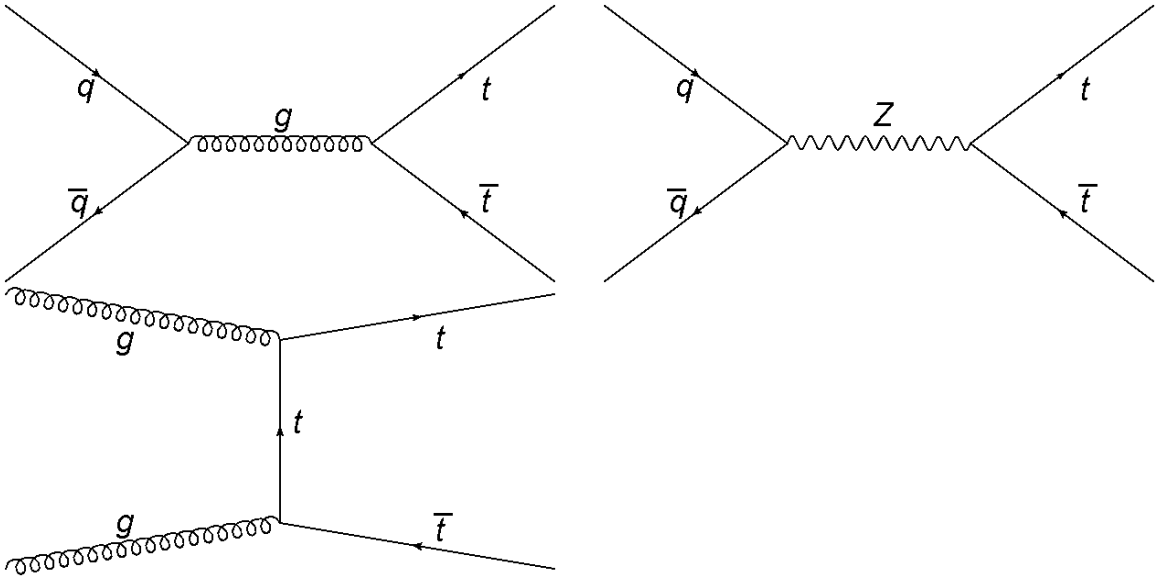

Figure 1.2: Several example Feynman diagrams showing several of the lowest order terms in the production of a top-antitop quark pair from a pair of incoming light quarks or gluons.

about the fundamental particles and their interactions which is required to completely describe the SM.

Performing calculations in a QFT can be highly non-trivial. In practice, many calculations in QFT are done using an approximation method known as perturbation theory. In this approach, a simpler theory with no interactions between particles is solved exactly. Provided that they are not too large, particle interactions may then be calculated as part of an infinite sequence of correction terms, with the accuracy of the theory improving as more terms are calculated. Feynman diagrams, in which a series of lines and vertices are drawn to represent particles and their interactions, are used as a mnemonic device for easily writing down terms in a perturbative expansion. Figure 1.2 shows several example Feynman diagrams corresponding to the production of a top-antitop quark pair from a pair of incoming light quarks or gluons.

1.1 Fermions

The fermions of the SM are arranged in three generations, each containing four particles: two quarks, one charged lepton and one neutral lepton. In addition, each fermion is partnered to an antiparticle, which has similar properties but opposite charges.[3]

The quarks are tightly bound together into composite particles by the strong nuclear force, as described more carefully in Section 1.3. The most common examples are protons and neutrons, which are composed of up and down type quarks from the first generation. The quarks carry electrical charge of $\frac{2}{3}$ or $-\frac{1}{3}$ times the charge of an electron, while their bound states carry integer charges.

The leptons can be divided into two types: the massive charged leptons and the nearly massless neutrinos. The presence of leptons in ATLAS is often associated with interesting physics processes, since the production of these particles in a proton-proton collision is rare.

The electron and the muon are the lightest two charged leptons and may be directly observed in the ATLAS detector. The third lepton, the tau, decays to lighter particles too quickly to be directly observed. The neutrinos carry no electrical charge and interact only via the weak nuclear force, making them difficult to detect.

The fermions are arranged such that they have an increasing mass in each generation.[4] Heavier particles in the later generations are generally unstable, decaying to their lighter first generation counterparts in a tiny fraction of a second via the weak nuclear force. Thus the vast majority of the visible universe is composed of fermions from the first generation. However, it may be noted that the second generation charged lepton, the muon, has a relatively long lifetime, with an average decay time of 2.2×10^{-6} seconds, or long enough to escape the ATLAS detector before decaying in most instances.

As half integer spin particles, fermions are subject to the Pauli exclusion principle which dictates that no two fermions may occupy the same state (regardless of whether they are fundamental or composite particles). Remarkably, this fact is responsible for much of the

[3] It is also possible that the neutrino is it's own anti-particle, a so called Majorana particle.

[4] With the possible exception of the neutrinos, whose masses have not been measured.

observed structure in the universe, as for example protons in a nucleus, or electrons in an atom are forced to occupy different states.

1.2 Gauge Bosons and Fundamental Forces

The SM describes the interactions between particles in terms of the electromagnetic, weak and strong nuclear forces. Each of these forces is associated to a local gauge symmetry group. In order to accommodate these gauge symmetries, additional fields must be added to the Lagrangian which interact closely with the fermions. The particles associated with these fields are the vector gauge bosons which act as the force carriers and allow the fundamental forces to propagate.

The weak nuclear force, responsible for nuclear decays and other phenomena, is mediated by the $W^{\pm}$ and Z bosons, while the photon mediates the electromagnetic force. The weak and electromagnetic forces share a common underlying framework in the electroweak sector of the SM. The strong nuclear force is mediated by eight gluons, and is responsible for creating tightly bound composite particles from constituent quarks, as described in Section 1.3anti.

1.2.1 Electroweak Theory and the Higgs Sector

Electroweak theory is the component of the SM which explains both the electromagnetic and weak nuclear forces. It supersedes QED, the quantum field theory of the electromagnetic force. This theory proposes the existence of a $\mathrm{SU}(2)_L \times \mathrm{U}(1)_Y$ gauge symmetry giving rise to four gauge bosons: B^0 is generated by the $\mathrm{U}(1)_Y$ local gauge symmetry and acts on weak hypercharge, while three additional bosons, (W^+, W^0, W^-), are generated by an $\mathrm{SU}(2)_L$ symmetry acting on weak isospin. In order for the gauge symmetry to hold all four of these particles would normally be required to be massless, a theoretical prediction which contradicts experimental observations.

However, the theory can be saved with the introduction of spontaneous symmetry breaking in the form of the Higgs field and associated Higgs boson. Unlike other SM fields, the energy of the Higgs field is minimized for non-zero values, as shown in Figure 1.3.

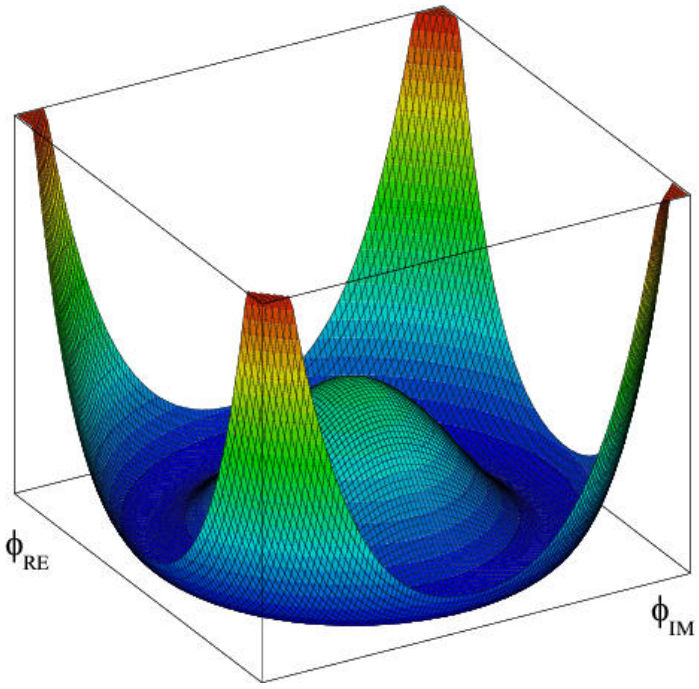

Figure 1.3: Potential energy of the Higgs Field as a function of its value. Its unusual shape gives rise to a non-zero vacuum expectation value which was determined by spontaneous symmetry breaking in the very early universe.

The SM proposes that the Higgs field settled into a minimal energy configuration during the early universe, spontaneously breaking the symmetry of the Higgs potential. The non-zero vacuum expectation value of the Higgs field interacts with the four electroweak bosons generating additional terms in the Lagrangian which behave similarly to a mass and yet do not break gauge invariance.

The existence of the Higgs boson has become one of the most widely publicized predictions of the SM and was confirmed by both the ATLAS and CMS experiments in 2012, 48 years after it was first proposed.

An additional complication arises in the theory, as the B^0 and W^0 bosons may mix with each other, allowing them to be described as orthogonal combinations of boson fields:

$$\begin{pmatrix} \gamma \\ Z^0 \end{pmatrix} = \begin{pmatrix} \cos(\theta_W) & \sin(\theta_W) \\ -\sin(\theta_W) & \cos(\theta_W) \end{pmatrix} \begin{pmatrix} B^0 \\ W^0 \end{pmatrix} \tag{1.1}$$

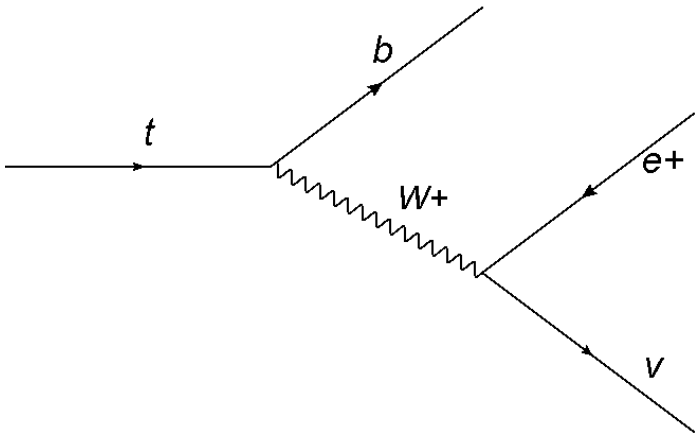

Figure 1.4: Feynman diagram showing the decay of a top quark to a bottom quark plus an anti-electron/neutrino pair.

However, it is possible to pick one linear combination, the photon (γ), which does not interact with the Higgs field, but rather remains massless. The remaining component is then labeled the Z boson with a mass of 91.2 GeV/c^2 while the $W^{\pm}$ bosons acquire a mass of 80.4 GeV/c^2.

As the mediator of the electromagnetic force, the photon interacts with electrical charges. Meanwhile, the Z and $W^{\pm}$ bosons mediate the weak nuclear force, acting on weak isospin. While the Z boson is associated with the creation or annihilation of fermion-antifermion pairs, the $W^{\pm}$ bosons are of special importance as the primary mechanism through which more massive fermions decay into their lighter counterparts. A W boson may decay into either a pair of quarks with different flavors (with charges summing to ± 1) or to a charged lepton/neutrino pair. Conversely, a fermion may change flavor by absorbing or emitting a W boson. Both of these possibilities are shown in Figure 1.4. Most such interactions will involve two fermions of the same generation. However, inter-generational mixing is also possible, with probabilities for quarks given by the Cabibbo-Kobayashi-Maskawa (CKM) matrix. The absence of an analogous flavor-changing neutral current involving a Z boson (a so called tree-level interaction) is not understood, nor is the near diagonality of the CKM matrix.

1.3 Strong Nuclear Force and Confinement

The strong nuclear force is described by the theory of quantum chromodynamics (QCD). An SU(3) local gauge symmetry is imposed on the SM Lagrangian, acting on color charge. As triplets of this color charge, quarks carry one of three colors: 'red,' 'green,' or 'blue,' while antiquarks carry an anticolor. Gluons, the force carriers of the strong nuclear force, form an octet, with each gluon carrying a color-anticolor pair or a linear combination of such pairs.[5]

In comparison to the electroweak sector, QCD is notoriously difficult to calculate. In the electroweak sector, the interaction between charges becomes weaker as the distance between them grows. This ensures that the energy required to separate two charges is always finite. In contrast, the strong forces between color charges does not decrease at large distances, implying that the energy of a system grows astronomically as one attempts to free quarks from a bound state.[6] As the charges become sufficiently separated, it becomes easier to create new quark-antiquark pairs out of the vacuum than to continue pulling the charges apart. This phenomenon prevents color charges from existing in isolation and implies that strongly interacting objects will always bind themselves in color neutral (singlet) states.

The two types of commonly observed bound states are mesons (quark-antiquark pairs) and baryons (sets of three quarks or three antiquarks), together referred to as hadrons. These quarks are then held together by a bundle of gluons and additional quark-antiquark pairs which pop in and out of existence. More exotic bound states, such as pentaquarks or glueballs, may be possible but have never been definitively demonstrated to exist [8].

During collisions between very high energy hadrons, quarks may be knocked out of their bound states and gluons may be radiated at high energy. In such cases, additional fragments of color charge are created and recombined into new hadrons. If the momentum of the emitted quark or gluon is large compared to the fundamental scale of QCD (λ_{QCD})

[5]The ninth state, an equal mixture of red-antired, blue-antiblue, and green-antigreen, is not an allowable state for a gluon as it is a color-neutral (color singlet) state.

[6]Current theory proposes that gluon-gluon interactions cause the color fields between the two charges to bunch up into a string like structure.

then the resulting fragments will form highly collimated bundles of particles known as jets which may be observed by experimenters.

Unlike other forces, strong interactions become very weak at short distances or at high energies, a property known as asymptotic freedom. Thus, it is possible to consider individual quarks in a proton as interacting independently from each other during high energy inelastic collisions, with confinement taking over very quickly afterwards.

1.4 Top Quark

The top quark is especially important to this study. At 173.1 GeV/c^2, the top quark is the heaviest fundamental particle in the SM. It primarily decays into a W boson plus a bottom quark, with a small chance to decay into a down or strange type quark from the first or second generation. The W boson will then decay into either a charged lepton/neutrino pair or into an up/down or charm/strange quark pair. As there are three colors of quarks, each possible decay to a quark-antiquark pair is roughly 3 times more likely than each lepton-neutrino pair. Since there are three accessible leptonic decays and two hadronic ones, roughly two out of three W bosons will decay hadronically. The top quark and W boson both have a very short lifetimes at 5×10^{-25} and 3×10^{-25} seconds respectively [9].

Top quark pairs can be produced in proton-proton collisions primarily via the strong interaction from the annihilation of a light quark-antiquark pair or two gluons. Much less frequently, top quark pairs may be produced through the weak nuclear force through an intermediary Z boson. Several examples of such processes are shown in Figure 1.2. Single top quarks can be also be created through weak interactions involving an exchange of a W boson, as shown in Figure 1.5. Many theories for physics beyond the SM predict an enhancement of top quark pair production, as discussed in the following chapter.

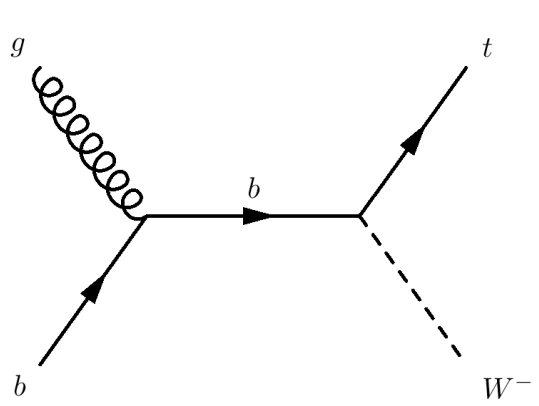

(a) Wt Channel

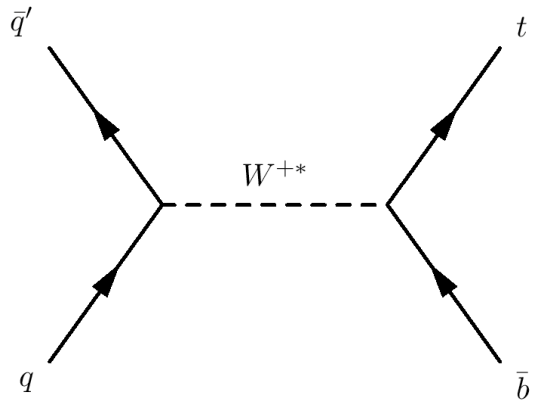

(b) s Channel

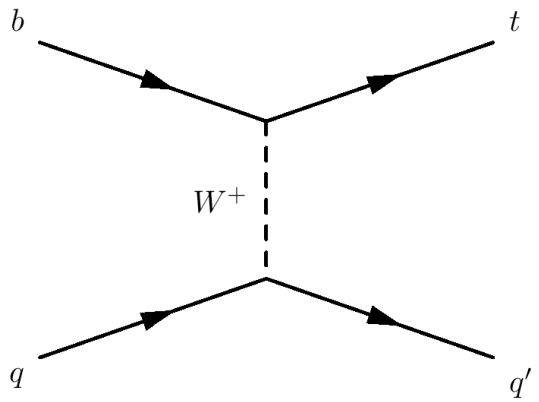

(c) t Channel

Figure 1.5: Several example Feynman diagrams showing several of the lowest order terms in the production of a single top quark.

Chapter 2

$t\bar{t}$ Resonances and Physics Beyond the Standard Model

Despite the incredible success of the SM, several unanswered questions motivate a continuing search for new physics. Some of the more significant shortcomings of the SM include:

- A surprisingly large difference between the strength of the electroweak and gravitational forces.[1] This is especially problematic given that the Higgs boson is required to be light in order to fulfill its role in electroweak symmetry breaking but might otherwise be expected to have a mass at the Planck scale ($m_p = 1.22 \times 10^{19}$ GeV). Correction terms to the Higgs boson mass arise due to the interactions between the Higgs boson and other particles. While it is possible that nearly perfect cancellation between these correction terms ensures that the Higgs mass remains small, the 'fine tunning' required to produce this outcome is considered unlikely. Alternatively, the addition of a new symmetry to the theory can force this cancellation of terms in a more natural way.

- The lack of a description of gravity within the framework of the SM.

[1] the graviational force is factor of 10^{32} times weaker than the electroweak force.

- The lack of a Dark Matter candidate. Only an estimated 4.9% of the mass and energy of the universe is composed of visible matter. The substance forming an additional 26.8% has yet to be observed [10].

- The presence of 30 input parameters (particle masses, mixing angles, and coupling constants) which can not be calculated from first principle, and lack of an explanation for the wide range of masses covered by the three generations of fermions.

- The observed violations of charge-parity symmetry are too small to explain the large matter-antimatter asymmetry observed in the universe.

A number of theories seeking to solve these outstanding issues predict the existence of new heavy particles coupling strongly to top quarks. The leading term in the quadratic divergence of the Higgs mass arises due to a one loop interaction with the top quark, implying that the top sector may be an especially interesting place to look for new physics. In addition, history suggests that the physical world may contain unforeseen surprises, and it is important to search for as wide a variety of possible new physics signatures as possible. Finally, the production and decay of $t\bar{t}$ pairs results in distinctive phenomenological features which may be readily identified in the ATLAS experiment, thus providing a promising search region which may be sensitive to a variety of new physics.

This study is designed to be as model independent as possible. However, in order to estimate the sensitivity of the analysis, several benchmark models are chosen, covering both wide and narrow width resonances and several choices for the spin of the associated heavy particle. The following sections describe these benchmark signal models. Phenomenological features of these models as they relate to a search for $t\bar{t}$ pairs are presented in Chapter 10.

2.1 Topcolor Z' Model

Topcolor assisted technicolor(TC2) is an alternative model of electroweak symmetry breaking [11]. In this model, a new strong force couples preferentially to four point interactions occurring primarily between quarks in the third generation ($t\bar{t}t\bar{t}$, $t\bar{t}b\bar{b}$, or $b\bar{b}b\bar{b}$). The coupling constant in this new interaction is sufficiently strong to give rise to a top quark

Mass [GeV]	$\sigma_{LO}(Z'_{\mathrm{TC2}})\times$ BR $\times 1.3$ [pb]
400 GeV	45.66
500 GeV	24.63
750 GeV	5.65
1000 GeV	1.66
1250 GeV	0.566
1500 GeV	0.213
1750 GeV	0.0853
2000 GeV	0.0357
2500 GeV	0.00687
3000 GeV	0.00147

Table 2.1: Cross sections times branching ratios of the benchmark Z' model for proton-proton collision at an 8 TeV center of mass energy assuming a width of 1.3%. A K-factor of 1.3 is applied to the cross section to account for next to leading order terms.

pair condensate, which plays a similar role as the Higgs boson in electroweak symmetry breaking. Additionally, the theory predicts a new spin-1 heavy boson, the Z', decaying preferentially to top quark pairs.

A leptophobic Z' boson is chosen as a benchmark [12; 13]. The cross section is calculated at leading order and a K-factor of 1.3 is applied to account for next to leading order terms [14; 15]. The cross sections and resonance widths predicted by this model are shown in Table 2.1 for several possible signal masses, while Figure 2.1 shows the branching ratios to different decay products.

2.2 Randall-Sundrum Models and Kaluza-Klein Bosons

The current theory describes the universe in terms of the 3+1 dimensional space-time of Special Relativity. However, a number of BSM theories postulate the existence of extra small dimensions which are not easily observable.

One class of such models is the Randall-Sundrum (RS) models, in which the universe is composed of a 4+1 dimensional bulk space separating two four dimensional branes, the TeV and Planck branes respectively (sometimes referred to as the IR and UV branes) [16].

While the two branes are nearly flat, the space in between is highly warped in the extra dimension.

In the original RS model, the SM particles described in Chapter 1 are strictly confined to propagate in the TeV brane. Gravitons are allowed to occupy the bulk, but with a wavefunction which grows exponentially weaker farther away from the Planck brane. The separation between gravitons and other particles explains the weakness of the gravitational force.

This search considers an extension of the RS class of models, in which SM particles are also allowed to propagate through the bulk [17]. These so called Bulk-RS models are not subject to certain flavor changing neutral currents which are problematic in the original models while improving agreement with precision electroweak measurements. Additionally,

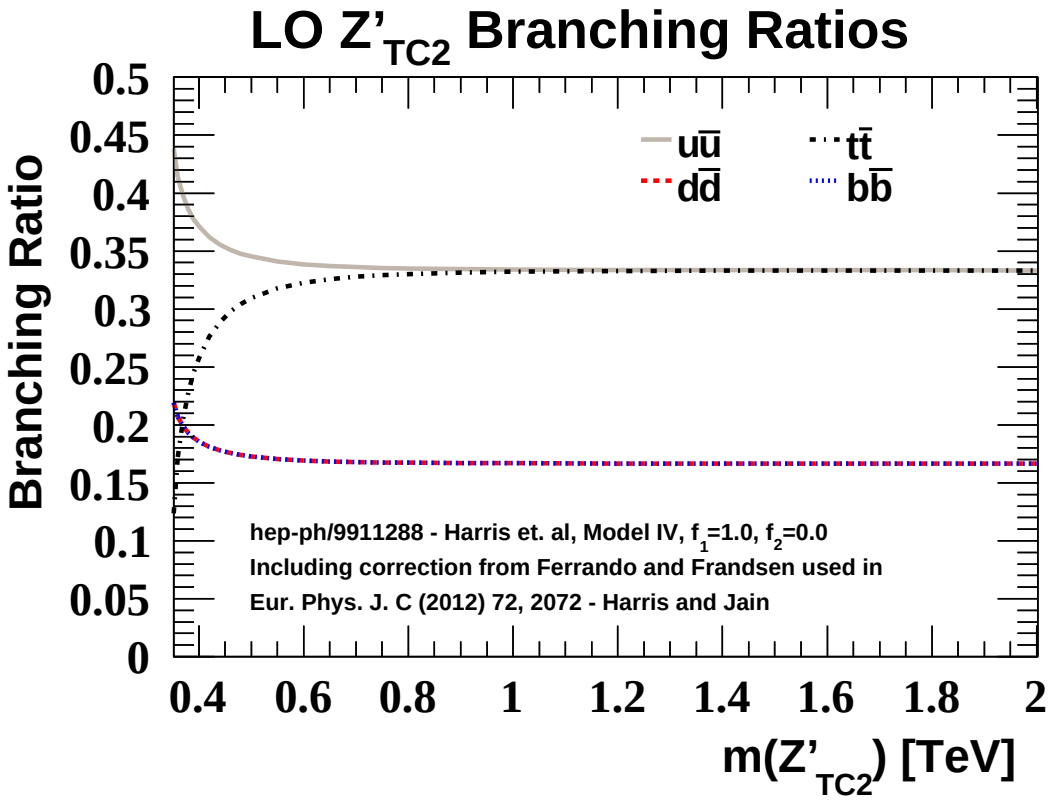

Figure 2.1: The branching ratios for a topcolor leptophobic Z' boson to decay to each of four flavors of quark/anti-quark pairs in the chosen benchmark model.

Mass [GeV]	Width [%]	$\sigma\times$ BR [pb]
400 GeV	15.3	112.2
500 GeV	15.3	81.9
600 GeV	15.3	45.0
700 GeV	15.3	25.2
800 GeV	15.3	14.6
900 GeV	15.3	8.81
1000 GeV	10	3.61
	15	5.37
	15.3	5.47
	20	7.08
	25	8.72
	30	10.3
	35	11.7
	40	13.1
1150 GeV	15.3	2.82
1300 GeV	15.3	1.52
1600 GeV	15.3	0.500
1800 GeV	15.3	0.255
2000 GeV	10	0.080
	15	0.133
	15.3	0.137
	20	0.193
	25	0.257
	30	0.324
	35	0.393
	40	0.461
2250 GeV	15.3	0.0670
2500 GeV	15.3	0.0351
2750 GeV	15.3	0.0196
3000 GeV	10	0.0057
	15	0.0113
	15.3	0.0120
	20	0.0184
	25	0.0268
	30	0.0361
	35	0.0462
	40	0.0568

Table 2.2: Cross sections times branching ratios of the benchmark KKg models for proton-proton collision at an 8 TeV center of mass energy.

Mass [GeV]	Width [%]	$\sigma\times$ BR [pb]
400 GeV	2.810	1.943
500 GeV	3.674	1.342
600 GeV	4.337	0.622
700 GeV	4.799	0.2859
800 GeV	5.125	0.1368
900 GeV	5.361	0.06838
1000 GeV	5.535	0.03569
1200 GeV	5.769	0.01077
1400 GeV	5.915	0.003578
1600 GeV	6.011	0.001288
1800 GeV	6.078	0.0004936
2000 GeV	6.125	0.0001978
2500 GeV	6.199	0.00002345

Table 2.3: Widths and cross sections times branching ratios of the benchmark KKG model for several masses for proton-proton collision at an 8 TeV center of mass energy.

the large mass of the top quark is explained as a consequence of its location near the Plank brane, while the remaining SM particles are preferentially located near the TeV brane.

However, it also predicts the existence of a series of Kaluza-Klein (KK) excitations of each SM particle. These excited states manifest themselves as KK particles in a corresponding 3+1 dimensional theory. KK particles are also located closer to the Planck brain, meaning that they decay preferentially to top quarks.

Two possible KK particles are considered in this search. The KK gluon(KKg) would have a relatively large production cross section at the LHC due to its coupling to the strong force, providing a wide width spin 1 vector boson [17]. In addition, a KK graviton (KKG) model provides a spin-2 resonance [18]. Tables 2.2 and 2.3 give the cross sections and widths of the chosen benchmark scenarios for KKg and KKG signals calculated at leading order. No consensus exists on the appropriate K-factor to apply to these models to approximate next to leading order terms and therefore none is applied. A KKG decays predominately to $t\bar{t}$, WW, ZZ, and HH, with branching ratios given in Figure 2.2.

f

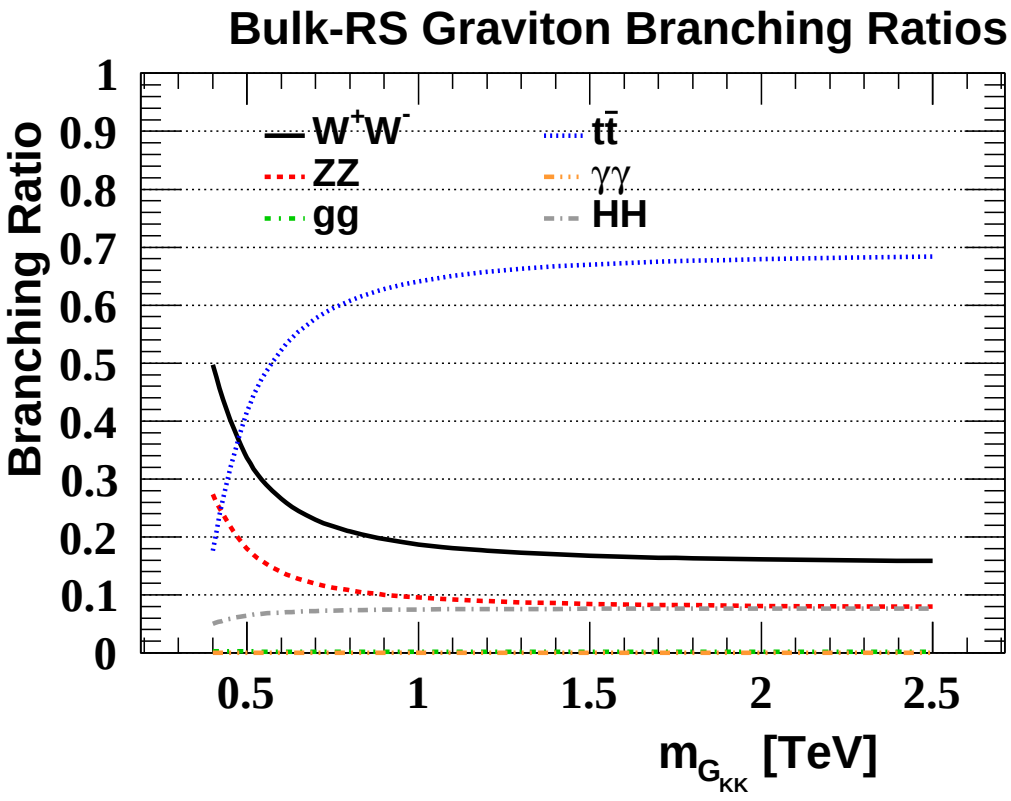

Figure 2.2: The branching ratios for the chosen Bulk-RS KKG benchmark model.

Chapter 3

The Large Hadron Collider

Since beginning operations near the end of 2009, the Large Hadron Collider (LHC) [19; 20] has become the most advanced particle accelerator ever built. As the latest in a long history of proton-proton (or proton-antiproton) accelerators [21; 22] built for the purpose of studying the fundamental laws governing the interactions between subatomic particles, the LHC represents a substantial advance in accelerator physics in two key dimensions. The LHC collided protons at 8 TeV of energy during the 2012 data taking period and is scheduled to reach a design energy of 14 TeV in 2015 surpassing the capabilities of any previous machine. Additionally, by producing nearly 1 billion collisions per second, the LHC is capable of producing data at a far higher rate than any previous particle collider. This allows physicists to probe increasingly rare phenomena with greater precision.

3.1 LHC Layout and Injector Chain

The LHC is located in the 27 km circular tunnel originally built for the Large Electron-Positron Collider (LEP) [23]. Both the machine and its host institute, the European Organization for Nuclear Research (CERN), straddle the border between France and Switzerland near the city of Geneva. Bunches of protons are accelerated in opposite directions through this tunnel before colliding at 4 interaction regions surrounded by the four primary experimental detectors (ATLAS, ALICE, CMS, and LHCb). Due to the difficulty of focusing proton beams and maintaining them in a stable orbit through a wide range

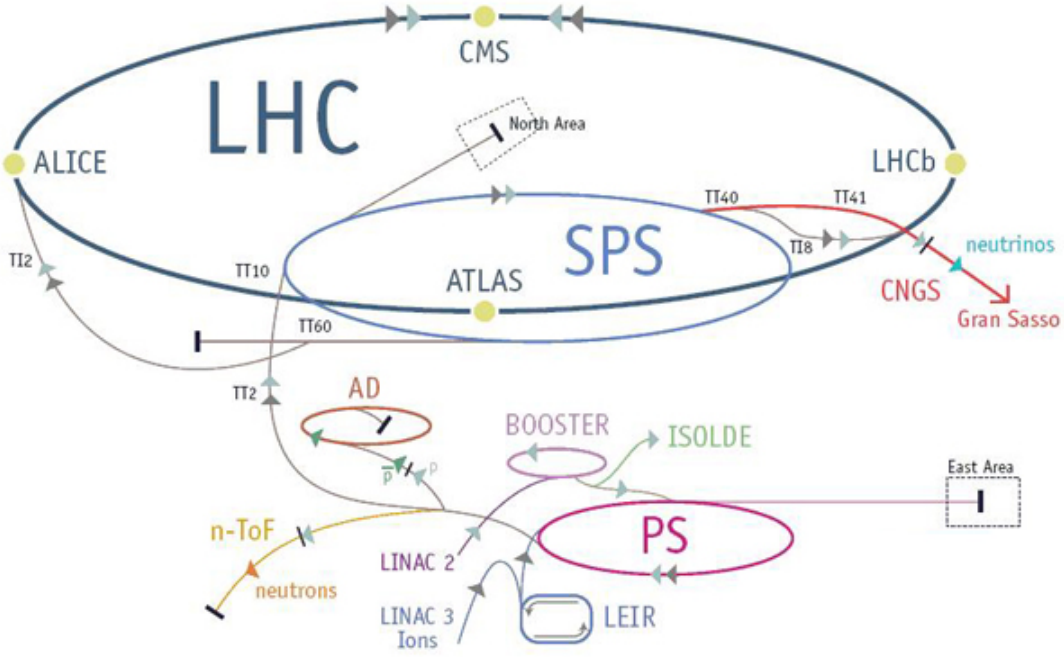

Figure 3.1: Layout of the LHC and the Injector Chain. Protons are accelerated through the Linac 2 linear accelerator, followed by the Proton Synchrotron Booster, Proton Synchrotron, and the Super Proton Synchrotron.

of energies in a single machine, it is necessary to accelerate protons in several stages [20]. Protons are prepared by stripping electrons off of hydrogen atoms before injecting them into the Linac 2 linear accelerator for an initial kick. They are then accelerated in stages through 3 circular accelerators: the Proton Synchrotron Booster, Proton Synchrotron, and the Super Proton Synchrotron. Finally, after reaching 450 GeV the protons are be injected into the LHC, where the beam may be ramped to the intended energy (4 TeV per proton in 2012). The layout of the LHC and it's injector chain is shown in Figure 3.1.

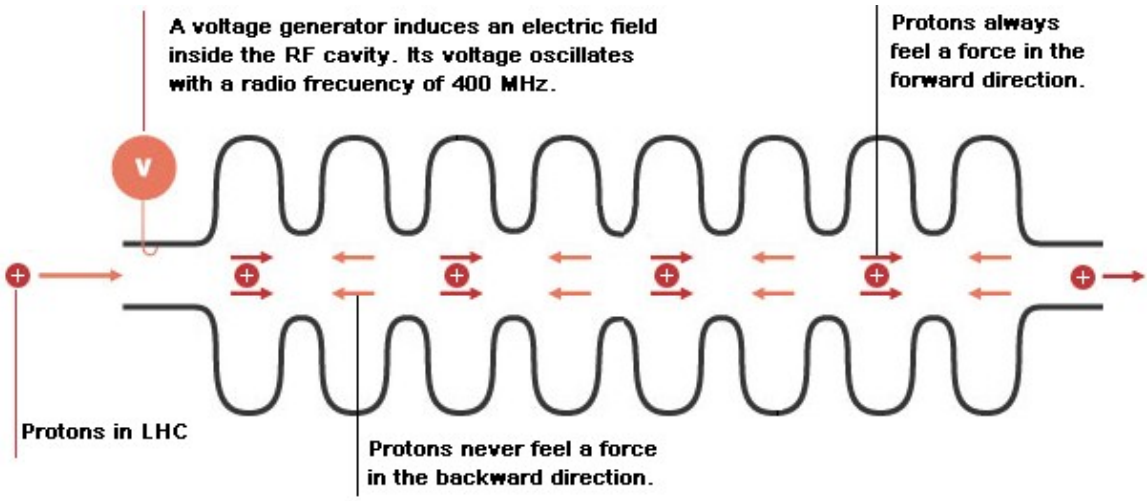

Figure 3.2: Schematic detailing the function of an RF cavity. Oscillating electromagnetic fields accelerate proton bunches.

3.2 The LHC Machine

3.2.1 Radio-Frequency Cavities

After entering the LHC, proton bunches are accelerated on each pass through the circular tunnel by a series of metal radio-frequency (RF) cavities, shown in Figure 3.2. Oscillating electromagnetic fields are driven at a resonance frequency of 400 MHz inside the cavities and are timed such as to provide an additional kick to passing proton bunches with 25 ns spacing (though not every bunch is filled with protons). The proton bunches are able to surf the generated electromagnetic waves, gaining energy on each pass through the LHC tunnel. It takes approximately 20 minutes to accelerate the protons from the 450 GeV injection energy to the 4 TeV operation energy used in 2012, with the protons completing their orbits 11,245 times per second.

3.2.2 Superconducting Magnets

In addition to accelerating protons, it is also necessary to keep the protons tightly focused and in a circular orbit through the machine. Thus, the energy attainable at the

LHC is currently limited by the strength of the super conducting magnets which are used for this purpose.

The LHC contains a total of 1232 main dipole magnets used for the purpose of bending the beam into a circular orbit. These magnets carry up to 11,850 amperes in order to generate an impressive 8.4 T magnetic field covering the majority of the 27 km tunnel.

In addition to the dipole magnets, 392 superconducting quadrupole magnets are used to focus the beam at regular intervals, while additional magnets squeeze the beam just before they collide in order to maximize the number of collisions.

The LHC magnets are formed from cables of niobium-titanium, a common type II superconductor used by several previous accelerators. The LHC uses superfluid helium to cool these cables to 1.9 kelvin, significantly below the 9.5 kelvin critical temperature of niobium-titanium [24].

Unfortunately, an accident occurred in late 2008 when several of the magnets quenched[1], causing substantial damage to a number of dipole magnets. As a result, the superconducting dipole magnets were operated below their design strength, limiting the machine to 4 TeV during 2012 data taking period. Ongoing repairs should allow the machine to reach its design energy soon after it resumes operation in early 2015.

3.3 Beam Characteristics

As mentioned in Section 3.2.2, the energy of the LHC is limited by the strength of the superconducting magnets, as well as the radius of the circular orbit. Both the 2012 operating energy at 4 TeV per beam, and the design energy at 7 TeV per beam represent a substantial increase over the 2 TeV of energy achieved by the LHC's most powerful predecessor, the Fermilab Tevatron Collider.

In principle one should also consider the synchrotron radiation produced by accelerating charged particles to be a limiting factor. However, due to the large mass of the proton and

[1]Quenching occurs when superconducting magnets heat up beyond their critical temperature leading to a loss of superconductivity and subjecting the magnet to rapid heating. In this incident, safety features successfully diverted the current in the magnet to nearby copper cables but failed to prevent a current arc which punctured a helium enclosure.

the large radius of its orbit, synchrotron radiation is not a limiting factor at the LHC. If electrons were to be accelerated rather than protons, the situation would be very different, since the emitted radiation increases with $1/m^4$. The energy loss per revolution of a charged particle due to synchrotron radiation can be given in terms of the particle energy (E), the radius of the circular orbit (r) and several physical constants including the mass of the particle (m):

$$P = \frac{e^2}{6\pi\epsilon_0 c^7 r^2 m^4} E^4. \tag{3.1}$$

For a proton, this works out to an energy loss of roughly 9 KeV per revolution. For a circular electron accelerator of the same energy, the loss per revolution would be $9x10^{-14}$ times larger.

In addition to the collision energy, the rate of collisions is of critical importance in a modern particle collider, since the phenomena being studied are often quite rare. The luminosity is given by Equation 3.2, where N_p is the number of protons per bunch, N_b the number of bunches circulating in the machine, t the time required to complete one orbit, and A is the effective area of the collision zone:

$$\mathcal{L} = \frac{N_p^2 N_b}{tA}. \tag{3.2}$$

While a great deal of effort is taken to optimize these parameters, care must be taken to ensure that the beam remains stable during operation. In general, higher luminosity leads to stronger interactions between the beams and greater repulsion between charges within each beam, increasing the difficulty in keeping the beams focused and in a stable orbit. Thus, a compromise must be continuously sought between optimizing the instantaneous luminosity and the amount of time spent collecting data under stable conditions. Integrating the luminosity over time, one arrives at the integrated luminosity, a measure of the total amount of data produced.

During the 2012 data taking period, the LHC achieved a peak luminosity at 7.73×10^{33} $\text{cm}^{-2}\text{s}^{-1}$, nearly 20 times higher than that achieved at the Tevatron, and an integrated luminosity of more than 20 fb^{-1}. This impressive performance is partly due to the possibility

to collide protons against protons rather than anti-protons, since the difficulty of producing an anti-proton beam was a major limiting factor at the Tevatron. Even higher luminosities are expected in the future.

During the 2012 data taking period, only every second bunch crossing was filled with protons. These filled bunches are then grouped into bunch trains, with larger gaps of unfilled bunches in between. These gaps are necessary to operate the injection magnets and beam dump magnets.

In order to maintain such a high luminosity, an average of 20 or more proton collisions may take place per bunch crossing. While this is necessary in order to achieve the required statistics in a manageable time frame, it also creates complications for the experimenters who need to account for the byproducts of these extra collisions (referred to as pile-up) when analyzing a particular collision of interest.

Chapter 4

The ATLAS Detector

The ATLAS detector is a nearly hermetic particle detector surrounding one of the four LHC interaction points where the two beams of protons collide head on[25]. With the ability to detect and measure nearly every outgoing particle produced in a collision and nearly 4π radians of coverage around the interaction point, ATLAS is sensitive to a wide range of physics processes. The detector has been carefully designed to take high quality data in the presence of higher levels of radiation, particle multiplicities, interaction rates, and collision energies than has been seen in earlier collider experiments.

With a length of 44 m and a diameter of 25 m ATLAS is also the largest colliding-beam detector ever built.[1] Roughly cylindrical in shape, it surrounds the two proton beams, with the collision point located in the center. The detector is composed of many layered sub-detectors, with each layer designed to detect and measure different combinations of outgoing particles. These sub-detectors are grouped into four main detector subsystems: the inner detector, the calorimeters, the muon system, and the forward detectors. In addition, the solenoid and toroid magnets are layered after the inner tracker and calorimeter respectively. The main cylindrical body of the detector (the barrel) is enclosed on either side by a series of disk-like endcaps which help to complete the detector coverage in the region close to the beam pipe. Finally, the trigger system must make decisions in real time on which events are sufficiently interesting to record. The detector layout is shown in Figure 4.1.

[1] Although ATLAS's sister experiment, Compact Muon Solenoid, is actually heavier.

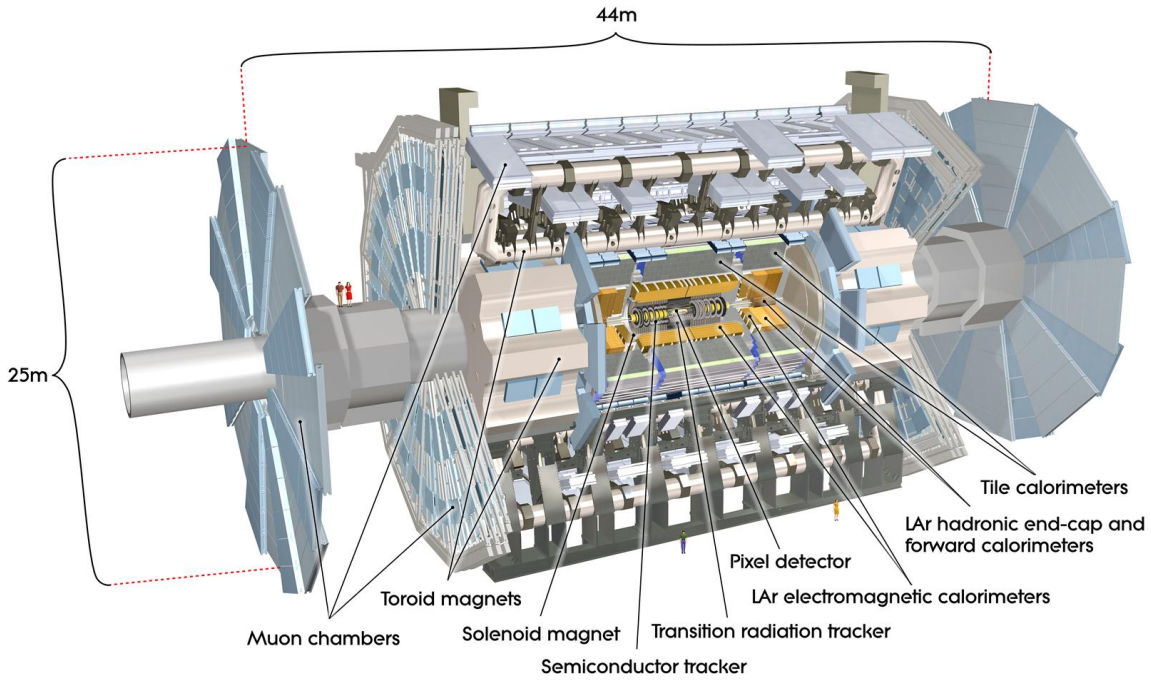

Figure 4.1: Layout of the ATLAS detector and main sub-components.

In order to simplify the description of the detector and of the observed physics, a common coordinate system is defined with the interaction point situated at the origin and the z-axis aligned with the beams. The polar angle, θ, is then defined relative to the beam axis, while the azimuthal angle ϕ describes the angular position in the perpendicular plane.

It is also convenient to define the rapidity of an outgoing particle, $y = \frac{1}{2}\ln[(E+p_z)/(E-p_z)]$. The difference in rapidity between two particles is invariant under Lorentz boosts along the z-axis, providing a convenient physics handle when considering the separation between particles.

When a particle's energy far exceeds its mass (as is generally the case at the LHC,) the rapidity may be approximated by the pseudorapidity, $\eta = -\ln(\tan(\theta/2))$. Thus, η, ϕ and $r = \sqrt{x^2+y^2}$, the radial distance from the beam axis, provide a convenient coordinate system for understanding the detector layout, coverage and resolution. Additionally,

the position of physics objects observed in the detector are generally measured in these coordinates, as is the distance between two objects, $\Delta R(r_1, r_2) = \sqrt{\Delta\eta^2 + \Delta\phi^2}$.

The portion of the detector at small values of $|\eta|$ is generally referred to as the central region. The interior portions of the endcaps, located at large $|\eta|$, are referred to as the forward region and are specifically designed to detect particles emitted close to the beam pipe.

4.1 The Inner Detector

The closest subsystem to the interaction point, the inner detector, is a tracking detector designed to make precise position measurements of passing charged particles. By combining several such measurements at different radii it becomes possible to reconstruct the path of a charged particle and to extrapolate it to other detector subsystems and to the point of origin in the collision region. Additionally, the tracker is immersed in a 2 T magnetic field produced by the central solenoid, allowing the charge and transverse momentum[2] (p_T) of charged particles to be measured from the track curvature.

Accurate track measurement close to the interaction region is especially important in a high luminosity environment as it allows for the association of tracks to individual vertices in interaction zone, thus allowing us to determine which physics objects originated from which collision in a single bunch crossing. With a mean of more than 20 proton-proton collisions occurring per bunch crossing, vetoing physics objects which resulted from a secondary collision is extremely important for background rejection. Additionally, the presence of decay vertices near the primary one may be indicative of the decay of a particle with a moderate lifetime and is of a special interest (this is a key ingredient in b-tagging, as described in a later section).

In addition to precise angular resolution, the inner detector must satisfy three additional requirements:

- Fine granularity is required close to the interaction point in order to distinguish the high multiplicity of particle tracks.

[2]The portion of the particles momentum which is perpendicular to the beam axis.

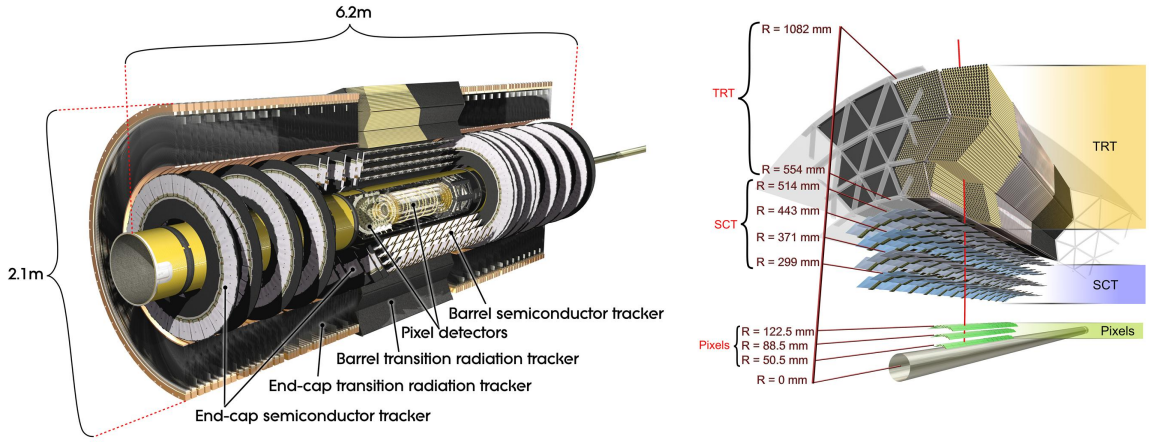

Figure 4.2: Layout of the ATLAS inner detector

- Tracks must be observed over a large enough distance to allow for an accurate measurement of their curvature.
- A limited material budget (the amount of material that a particle must pass through on its way out of the detector) should be maintained in order to minimize scattering and energy loss of passing particles which would otherwise degrade subsequent measurements.
- Sufficient radiation hardness to survive the environment close to the interaction zone for an extended period of time.

In order to accomplish these requirements, the inner detector is composed of 3 sub-detectors with increasing distance from the origin: the Pixel Detector, Semi-Conductor Tracker (SCT) and the Transition Radiation Tracker (TRT). The layout of the inner detector is shown in Figure 4.2. Table 4.1 Gives a summary of the inner detectors coverage and performance characteristics.

4.1.1 The Pixel Detector and the Semi-Conductor Tracker

The Pixel Detector and the SCT are silicon tracking detectors which form the innermost layers of ATLAS. Thin silicon wafers are arranged around the collision zone. A moderate

Subdetector	Coverage	Spatial resolution [μm]	Points per Track
Pixel Barrel	$\|\eta\| < 2.5$	10 (r-ϕ) 115 (z)	3
Pixel Endcap	$2.0 < \|\eta\| < 2.5$	10 (r-ϕ) 115 (r)	3
SCT Barrel	$\|\eta\| < 1.5$	17 (r-ϕ) 580 (z)	4*
SCT Endcap	$1.3 < \|\eta\| < 2.5$	17 (r-ϕ) 580 (r)	9
TRT Barrel	$\|\eta\| < 1.0$	130 (r-ϕ)	36 **
TRT Endcap	$0.8 < \|\eta\| < 2.0$	130 (r-ϕ)	36 **

Table 4.1: Summary of the design performance and coverage of the inner detector. *Each point in the SCT Barrel consists of a double-layer hit. **Each track is expected to hit an average of 36 straw tubes.

voltage is applied across the layer of silicon depleting it of charge carriers and preventing current from flowing.[3] Passing charged particles will then excite electrons out of the valence band into the conduction band, allowing current to flow through the detector. The corresponding charge is then accumulated by sensors arranged along the silicon wafer, and a hit is registered in the detector if the charge accumulated exceeds a given threshold. Collections of these hits may then be reconstructed into charged tracks by the trigger and data processing software.

The silicon is initially prepared with n-type doping, primarily carrying a current via electron holes in the valence band. However, the high radiation environment will damage the silicon over time, changing its behavior to that of a p-type semiconductor after several years of operations. The applied voltage must be adjusted and the readout recalibrated as the silicon sustains increasing radiation damage.

The Pixel Detector represents the finest granularity and most radiation hard technology used in the inner detector. It is composed of three cylindrical layers in the barrel region, with radii 50.5, 88.5 and 122.5 mm from the beam axis respectively. Three disks on either

[3]Silicon tracking detectors are also capable of operating below the depletion voltage with some performance implications

side form the endcap, at 495-650 mm from the detector center. In total, 1.8 m^2 of silicon wafers are divided into 80 million channels, arranged into rectangular pixels with a nominal size of 50x400 μm^2 (some channels are larger). A resolution of 10's of μm in the azimuthal direction and around 100 μm along the z-axis is achieved by comparing the amount of charge deposited in adjacent readout channels.

Due to the increasing size of each layer, constructing additional layers of the inner detector from the technology used in the pixel detector would prove prohibitively expensive. Additionally, the detector requirements in terms of radiation hardness, required spatial resolution, and maximum occupancy can be relaxed as one moves away from the collision zone. Thus, a different compromise between performance, monetary cost, and material budget is sought in the SCT.

The SCT is a much larger detector with a total length of 1492 mm and over 60 m^2 of total area arranged in 4 double layers in the barrel (with radii between 299 and 514 mm) and 9 disks on either endcap. The SCT has much larger and fewer channels than the Pixel Detector, with the channels highly elongated along the z-axis (80 μm x 6 cm). Nevertheless, the excellent azimuthal resolution of the SCT is critical for making precise track momentum measurements. The barrel consists of double layers of silicon wafers, with a 40 mrad angle between the strips providing improved resolution along the z-axis.

4.1.2 Transition Radiation Tracker

Unlike the Pixel detector and SCT, the TRT is a Xenon gas based straw tube detector[26]. The detector is composed of nearly 370,000 single wire straws, running parallel to the beam axis and covering a radius of 563 to 1066 mm in the barrel, while running in a radial direction in the endcap. Each straw is a 4mm diameter Kapton® tube filled primarily with Xenon gas and smaller amounts of CO_2 and O_2. A single gold-plated tungsten wire runs down the center, with a 1530 V potential difference applied between the wire and the straw tube.

Relativistic charged particles entering the medium inside of a tube emit transition radiation due to the changing dielectric permittivity. This radiation will then ionize the Xenon gas inside of the tube, allowing electric current to flow. The charges accumulated on

the wire and tube then flow down the length of the straw. The current produced in each straw can be read out at either end of the barrel, or on the outside of the endcaps.

The amount of transition radiation emitted is strongly dependent on the mass of the charged particle. Thus, unlike the Pixel Detector and SCT, the TRT is able to discriminate between electrons and heavier charged particles such as pions. As electrons produced in the gas are accelerated by the electrical field, they can ionize additional atoms. However, the charge accumulated on the anode and cathode remains proportional to the charge deposited in the bulk of the detector.

4.2 Calorimeters

After passing through the inner detector, emitted particles hit the ATLAS calorimeters, designed to absorb and measure the total energy of a wide variety of incident radiation. There are two calorimeter subdetectors on ATLAS: the Liquid Argon (LAr) and Tile calorimeters. Both subdetectors are built as sampling calorimeters which alternate layers of a dense material (the absorber) designed to break high energy particles into a shower of radiation and layers of active media designed to measure (or sample) the amount of radiation produced.

Since electromagnetic and hadronic particles shower differently, and especially since the stopping distance for electromagnetic particles tends to be considerably shorter, the calorimeter is divided into two regions, with the electromagnetic calorimeter in front of the hadronic calorimeter. Each of these two regions may then be optimized for one type of incident radiation, although there can be significant cross contamination. Hadronic and electromagnetic calorimeters generally differ in the relative sizes of absorbers and the active media, the size of calorimeter cells, and often on the choice of dense material used in the aborber to create the shower, with additional stopping power needed in a hadronic calorimeter. The choice of active medium does not necessarily depend on the type of calorimeter. On ATLAS the Tile calorimeter is a hadronic calorimeter located in the barrel, while the LAr calorimeter serves as both the endcap of the hadronic calorimeter and the electromagnetic calorimeter for the entire detector.

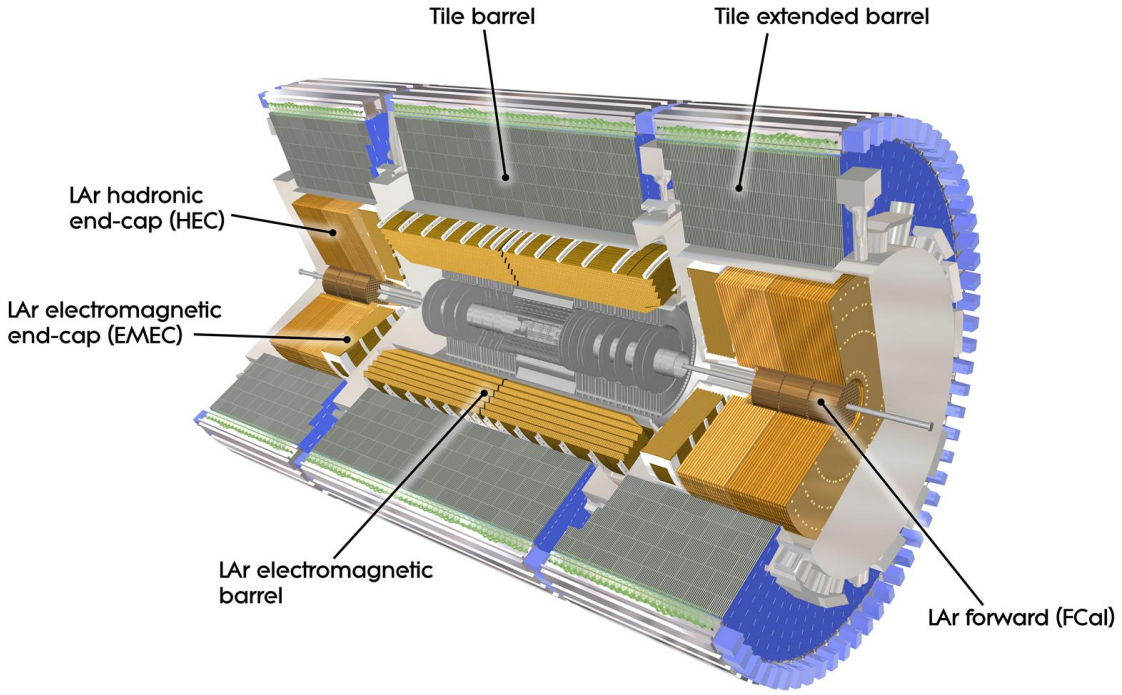

Figure 4.3: Layout of the ATLAS Calorimeter, outside of the ID and solenoid magnets.

Figure 4.3 shows the overall layout of the calorimeter. It is important to note that the ATLAS calorimeters are placed outside of the solenoid magnet, an important design choice which is discussed in Section 4.4.

4.2.1 Particle Showers

Two types of particle showers need to be considered inside of the ATLAS calorimeter. Electromagnetic showers are produced by high energy electrons, positrons, and photons. When passing through a dense material, incident photons will split into an electron-positron pair with roughly equal energy. Electrons and positrons, on the other hand, will radiate high energy photons via the Bremsstrahlung process.

The radiation length, X_0, is a property of the material which describes the characteristic distance traveled by electromagnetic radiation during a shower. Electrons will lose an average of 1/e of their original energy when traveling a distance X_0, while photons have

a mean free path of $\frac{9}{7}X_0$. X_0 is roughly inversely proportional $Z(Z+1)$, where Z is the number of protons in the material's nucleus. E_c, the critical energy at which the energy loss due to ionization and Compton Scattering become significant is also a property of the material and is roughly inversely proportional to the material's Z. The approximate shower depth at which electromagnetic radiation penetrates into the calorimeter is thus given by:

$$X = X_0 \frac{\ln(E_0/E_c)}{\ln 2} \tag{4.1}$$

Hadronic showers are more complex than their electromagnetic counterparts. Hadronic particles produce additional QCD radiation, resulting in the creation of a wide variety of hadronic particles (pions are very common) and with a varying multiplicity per interaction. Much of this radiation may then generate electromagnetic showers by decaying into photons (especially the neutral pion). The incident particles may also interact with the nuclei of the material, causing a release of additional particles. Finally, a large recoil of the target nuclei results in invisible energy being deposited into the absorber. Thus, calorimeter deposits require a different calibration depending on whether incident radiation is electromagnetic or hadronic in nature.

In addition, the characteristic radiation distance is substantially larger for hadronic radiation and generally increases with the cubed root of the number of nuclei per atom in the material. Thus, hadronic calorimeters are generally larger in volume and placed behind the electromagnetic ones, and a different choice may be made for the design of the absorbers used to instigate the showers.

As a result of this showering process, the total amount of radiation produced in a sampling calorimeter, and thus the detector response, is approximately proportional to the energy of the incident particle. Figure 4.4 illustrates example electromagnetic and hadronic showers.

4.2.2 Liquid Argon Calorimeter

The LAr subsystem serves as the electromagnetic calorimeter on ATLAS, as well as the hadronic calorimeter on the endcaps. Liquid Argon was chosen for this purpose due its inert nature, radiation hardness, and intrinsically linear response.

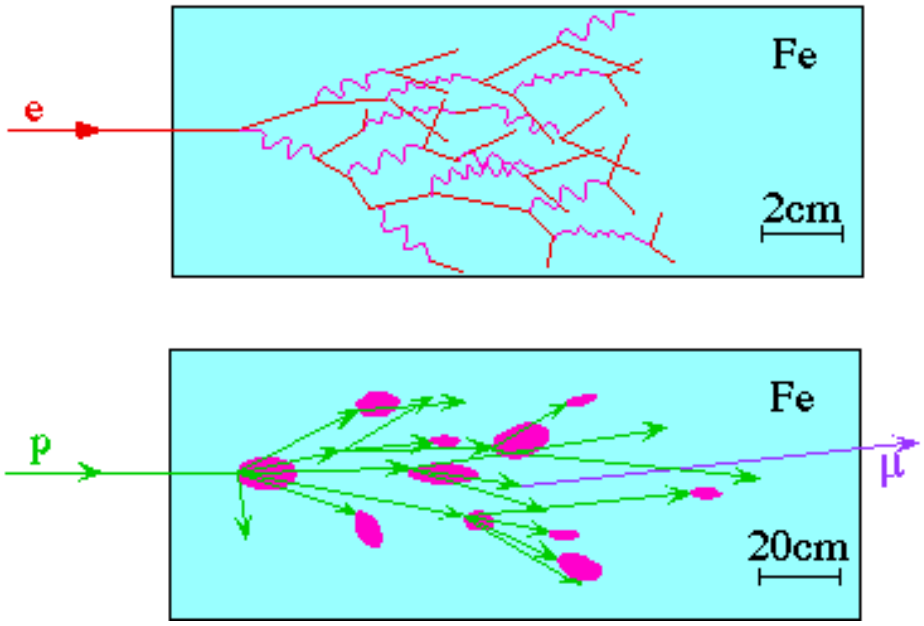

Figure 4.4: Example calorimeter showers instigated by energetic particles in the calorimeter. In the top half of the figure, an incoming electron produces a shower of electrons (solid red lines) and photons (squiggly pink lines.) In the bottom half, a proton initiates a shower of hadronic material (green lines) with each pink oval representing an interaction with the absorber material. A muon is also produced by the decay of a heavy meson. Image thanks to David Bailey at the University of Toronto.

The electromagnetic calorimeter is built with alternating layers of lead and liquid argon, built into an accordion shape which ensures that all particles cross both liquid argon and lead several times with no coverage gaps needed to maintain the detector structure. Thus, the lead absorber layers allow passing radiation to shower, while charged radiation ionizes the liquid argon, allowing charge to flow through the active medium. Figure 4.5 shows the accordion shape of the lead sheets and liquid argon active medium.

The main body of the electromagnetic calorimeter barrel is segmented into three layers of depth. Precise η position measurements provided by the first layer allow for the discrimination between photons and neutral pions decaying into a pair of photons and to the determination of the angle of incident radiation. Although the second layer has a less precise η resolution, its greater depth is needed to absorb the bulk of the incident energy. The final

Figure 4.5: The LAr accordion structure ensures multiple crossings between the active medium and the heavy absorber.

layer is needed to measure the most energetic particles and helps to distinguish between hadronic and electromagnetic deposits, which require different calibrations. Figure 4.6 shows the layout of the three calorimeter layers in the barrel region.

Each electromagnetic endcap (EMEC) is composed of two coaxial wheels and is designed under similar principles as the barrel region. Behind it, the hadronic endcap (HEC) also utilizes a liquid argon active medium, but with copper sheets as the absorber. Inside of the HEC, very close to the endcaps, the Forward Calorimeter (FCAL) is built from both copper and tungston rods and serves as both the electromagnetic and hadronic calorimeter at very high $|\eta|$.

The placement of the calorimeter behind the solenoid and the inner detector implies that particles have already begun to shower before reaching the calorimeter. For this reason, an additional layer, the presampler, is also placed in front of the solenoid magnet. The presampler is a thin layer of liquid argon which provides a handle for understanding incident radiation at an earlier stage in its evolution and for preparing appropriate calibrations of the detector. Figure 4.7 shows the amount of material in front of the electromagnetic calorimeter, as well as the depth of the calorimeter layers themselves in

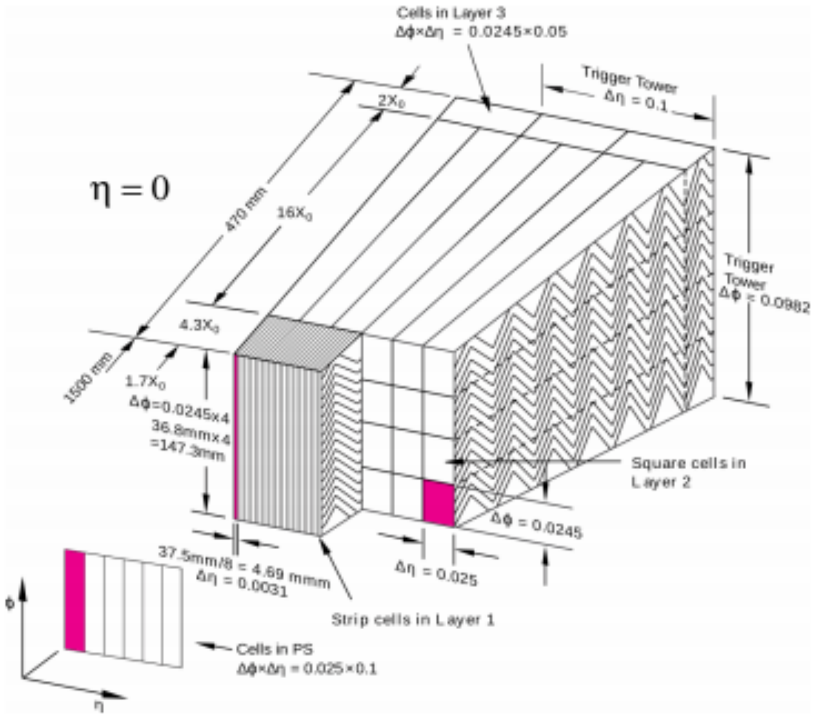

Figure 4.6: Layout of the ATLAS Liquid Argon EM Calorimeter, showing the three main layers in the Barrel.

terms of the electromagnetic radiation lengths. Figure 4.8 shows a similar measure for the hadronic calorimeters in terms of the hadronic interaction length and also includes the Tile calorimeter, described in the following section.

When charge is deposited in the calorimeter, it must drift to the readout to be registered as a current. While the advantages of liquid argon have already been mentioned, the drift time in this medium is particularly slow, at approximately 450ns in the barrel. The response to energy deposits in the detector shows a strong peak, followed by a long tail. Figure 4.9 shows a typical signal in the LAr calorimeter before and after the shaping which is done in the front end electronics by taking the derivative of the current. During normal data taking, 5 sample readings of this signal are taken at 25 ns intervals.

Even after this shaping, the signal peak remains several bunch crossings wide. This means that the LAr calorimeter is especially sensitive to out-of-time pile-up, ie. radiation

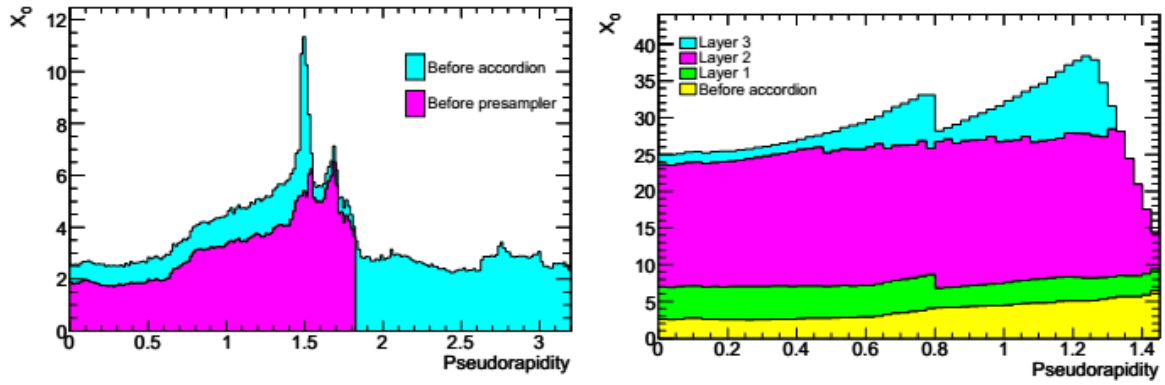

Figure 4.7: Left: total material in front of the presampler and the main electromagnetic calorimeter. Calorimetry resolution is reduced in the crack region between the barrel and endcaps due to the large amount of material there. Right: Depth of each calorimeter layer in the barrel region.

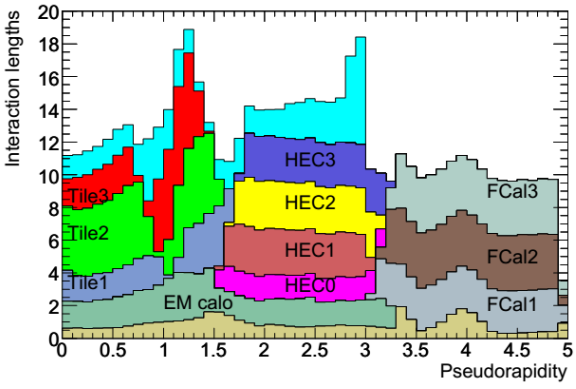

Figure 4.8: Depth of the calorimeters in terms of the hadronic interaction length

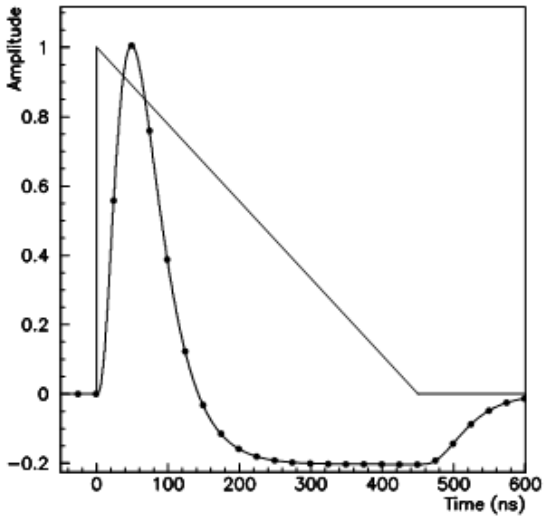

Figure 4.9: Shape of the output signal in the LAr detector, before and after shaping.

which is produced by collisions in bunch crossings slightly before or after the primary collision.[4]

4.2.3 Tile Calorimeter

The Tile calorimeter is the hadronic calorimeter in the barrel region, placed immediately outside of the LAr calorimeter. As with LAr, the Tile Calorimeter is segmented into three main layers in depth, forming a cylinder with inner and outer radii of 2.28 and 4.25 m respectively. It is additionally composed of a main barrel, covering $|\eta| < 1.0$ and two extended barrels surrounding the LAr end caps and covering $0.8 < |\eta| < 1.5$.

In place of a liquid argon medium, the Tile calorimeter uses plastic scintillating tiles[5] as the active medium, while steel plates serve as the absorber. This approach was chosen to be more cost effective for constructing a detector which is several times larger than the LAr detector. Hadronic radiation will typically deposit energy in the electromagnetic as well as hadronic calorimeters, and will also produce charged particle tracks in the ID. Thus,

[4]All ATLAS subdetectors are unavoidably sensitive to in-time pile-up, produced by multiple collisions occurring in the same bunch crossing.

Subdetector	Coverage	Type
LAr Presampler	$\|\eta\| < 1.8$	Electromagnetic*
LAr Barrel	$\|\eta\| < 1.475$	Electromagnetic
LAr EMEC	$1.375 < \|\eta\| < 3.2$	Electromagnetic
Tile Main Barrel	$\|\eta\| < 1.0$	Hadronic
Tile Extended Barrel	$0.8 < \|\eta\| < 1.7$	Hadronic
LAr HEC	$1.5 < \|\eta\| < 3.1$	Hadronic
LAR FCAL	$3.1 < \|\eta\| < 4.9$	Both

Table 4.2: Summary of the coverage of the electromagnetic and hadronic calorimetry systems. *LAr presampler more closely resembles a tracker than a calorimeter due to the absence of an absorber.

the strong spatial resolution of the LAr barrel and ID complement the energy resolution achieved in the Tile detector.

While Tile is not as radiation hard as LAr due to the damage which is accumulated on the scintillating tiles, the accumulated damage over 10 years of operations at the LHC design luminosity is expected to reduce the detector response by less than 10% in the innermost layer.[6]

Table 4.2 shows a summary of the coverage of the calorimetry system.

4.3 Muon System

Two known particles are capable of escaping the calorimetry system at moderate energies.[7] Neutrinos, long lived nearly massless particles which interact only via the weak force, can not be observed directly by ATLAS but must be indirectly inferred from an imbalance of the energy and momenta observed in the detector. Although muons are

[5]Scintilators are materials which produce light when excited my ionizing radiation.

[6]The endcaps are subjected to far higher radiation doses than the barrel, motivating the use of a liquid argon medium there.

[7]Very high energy jets may also punch through the calorimeter.

observable in tracking detectors due to their electric charge, their large mass greatly reduces the bremsstrahlung radiation experienced in a dense medium, meaning that they are not stopped by the calorimeters. Unlike their even heavier counterpart, the tau, muons are sufficiently long lived[8] to escape the detector without decaying.

Although theoretically possible, reconstructing a muon based solely on the ID and the presence of only small calorimeter deposits is complicated by a high multiplicity of tracks and calorimeter deposits, the imprecision in matching tracks to calorimeter hits, and the reduced momentum resolution of the ID at high p_T.[9] Thus, an additional tracker is placed outside of the calorimeters in order to improve muon identification efficiency and resolution.

The muon system is immersed in a weaker magnetic field than to the inner detector, relying on larger distances to improve momentum resolution. An average magnetic field of 0.5 T is provided by a combination of the barrel and endcap toroid magnets. As the magnetic field runs in the azimuthal direction, precise tracking measurements in the radial and z directions are especially important for momentum measurements, while the requirements on ϕ resolution are more relaxed.

The size of the muon system necessitates the use of gas based tracking technologies. The Monitored Drift Tubes (MDT) and Cathode Strip Chambers (CSC's) form the precision muon system, designed for measuring muon momenta with the highest possible precision. Meanwhile the trigger muon system, composed of Resistive Plate Chambers (RPC) and Thin Gap Chambers (TGC), provides a faster detector response in order to satisfy the requirements of the trigger system. The layout of the Muon System is shown in Figure 4.10.

4.3.1 Precision Muon System

The precision muon system is primarily composed of the MDT chambers, which provide precise tracking measurements in the $r - z$ plane (though not in the azimuthal direction). The drift tubes themselves are 30 mm wide tubes filled with a mixture of argon and carbon dioxide gas at a pressure of 3 bar. Passing muons ionize this gas, producing electrons which

[8] With a lifetime of 2.2×10^{-6} seconds in the muon rest frame.

[9] At high p_T, the curvature of tracks approaches 0, reducing the tracker resolution. For electrons, this is compensated by the improving resolution of the calorimeter at high energies.

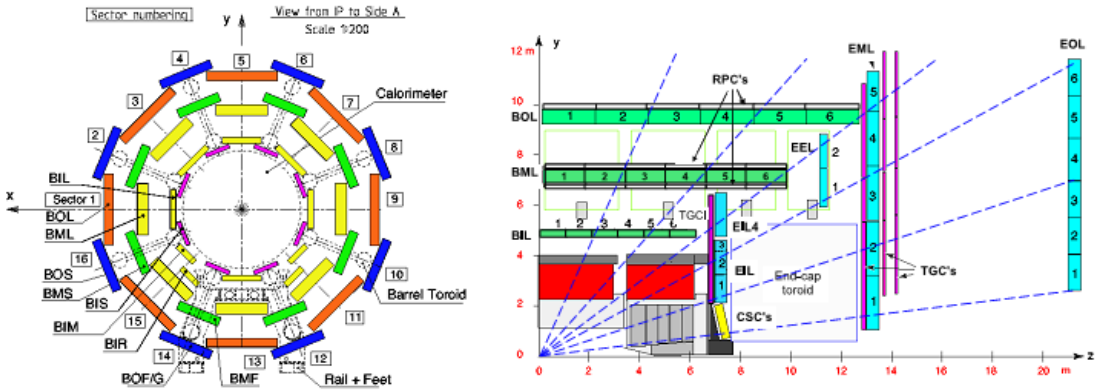

Figure 4.10: Layout of the Muon System. Left: Cross section of the barrel perpendicular to the beam axis. Right: Cross section of the muon system along the beam axis. Green and blue boxes represent the MDT, while the CSC is shown in yellow. The muon trigger system is also shown.

accumulate on a tungsten-rhenium wire in the center of the tube held at a 3080 V potential difference with respect to the walls of the tubes. Each chamber is constructed from a collection of tubes forming 3-8 layers. These chambers are then arranged in three layers covering $|\eta| < 2.7$ as shown in Figure 4.10. Overlap between adjacent chambers ensures an absence of coverage gaps.

The drift time of electrons through the gas medium is also measured, allowing the MDT to measure tracks with a 40 μm resolution in the plane perpendicular to the magnetic field and an angular resolution of 3×10^{-4} radians per chamber (or 80 μm for a single tube layer). However, the readout is unable to resolve multiple hits and the slow drift time (up to 700ns) implies a significant dead time after every hit. This makes it unsuitable in a high occupancy environment with more than 150 muons per cm^2 per second.

Instead of MDT chambers, CSCs are used in the high occupancy region close to the beam pipe ($2.0 < |\eta| < 2.7$) on the innermost layer of the muon system. Each CSC is composed of a series of anode wires with 2.5 mm separation which is also immersed in an argon and carbon dioxide gas mixture. Cathode sheets on either side of the wires are segmented into 1.6 mm strips, with the strips on one cathode perpendicular to those on the other. The distribution of current induced through the cathode is then be used to provide

a tracking resolution of up to 60 μm per CSC layer. This technology exhibits a smaller drift time (40 ns) and the ability to better distinguish multiple hits in a high occupancy environment than the MDT.

As with any tracker, the momentum resolution of the muon system falls with rising momenta as the curvature of the track approaches zero. However, the precision muon tracker maintains adequate resolution for muons up to approximately 3 TeV.

4.3.2 Muon Trigger System

While the MDTs provide excellent track momentum resolution, several problems require them to be complemented by faster detectors. First, the response time is too slow for the ATLAS trigger system which needs to provide real time decisions to save or reject events for full processing and analysis. Second, the large variability in response time makes it difficult to associate hits to particular bunch crossings. Finally, MDT do not provide meaningful resolution in the ϕ direction.

For this purpose, the muon system utilizes two additional technologies: RPCs in the barrel region, and TGCs in the endcaps. RPCs consists of two charged plates segmented into strips (with the strips on each plate perpendicular to each other). Meanwhile, the TGC is a multiwire chamber narrowly sandwiched between two cathode plates. Deposited charge is read out of the wires, unlike the CSC.

The RPCs are filled with a mixture of $C_2H_2F_4$, Iso-C_4H_10, and SF_6, while the TGCs are filled with carbon dioxide and n-pentane(n-C_5H_12). Both gasses allow for faster drift times. Additionally, RPCs operate in avalanche rather than proportional mode like the other ATLAS gas detectors. In avalanche mode, a very strong electrical field (4.9 kV/mm) quickly ionizes the entire volume of the detector in response to deposited charges, leading to a very fast response time. TGCs operate in proportional mode (ionized electrons ionize additional atoms, but not the full volume) but with a very high gain.

		Resolution Per Chamber				
Subdetector	Coverage	z/R	ϕ	time	Hits Per Track	Function
MDT	$\|\eta\| < 2.7$	35 μm (z)	—	—	20	Precision
CSC	$2.0\|\eta\| < 2.7$	40 μm (R)	5 mm	7 ns	4	Precision
RPC	$\|\eta\| < 1.05$	10 mm (z)	10 mm	1.5 ns	6	Trigger
TGC	$1.05\|\eta\| < 2.4$	2-6 mm (R)	3-7 mm	4 ns	9	Trigger

Table 4.3: Summary of the coverage and performance of the Muon System. Resolution is shown for a single muon chamber.

4.4 Magnets

Several magnets in ATLAS curve charged particle tracks, allowing for precise momentum measurements. One of the primary design differences between ATLAS and CMS was the decision to place a solenoid magnet in front of the calorimeter rather than behind it. While this choice adds additional material in front of the calorimeters, it also eases space restrictions in the detector. The ATLAS inner tracker is therefore larger than its CMS counterpart, achieving its design aims with a smaller magnetic field. (The axial field is 2 T in ATLAS, rather than 4 T in CMS.) Meanwhile ATLAS's deeper calorimeter minimizes the risk of the punch-through which occurs when very high energy radiation reaches the end of the calorimeter without dissipating. Lastly, the since the ATLAS calorimeter is outside of the solenoid, it operates in a smaller magnetic field, simplifying the process of modeling particle showers and calibrating the detector response.

Outside of the calorimeters, the barrel and two endcap toroids generate a magnetic field running azimuthally around the detector. Figure 4.11 shows the layout of the ATLAS magnets.

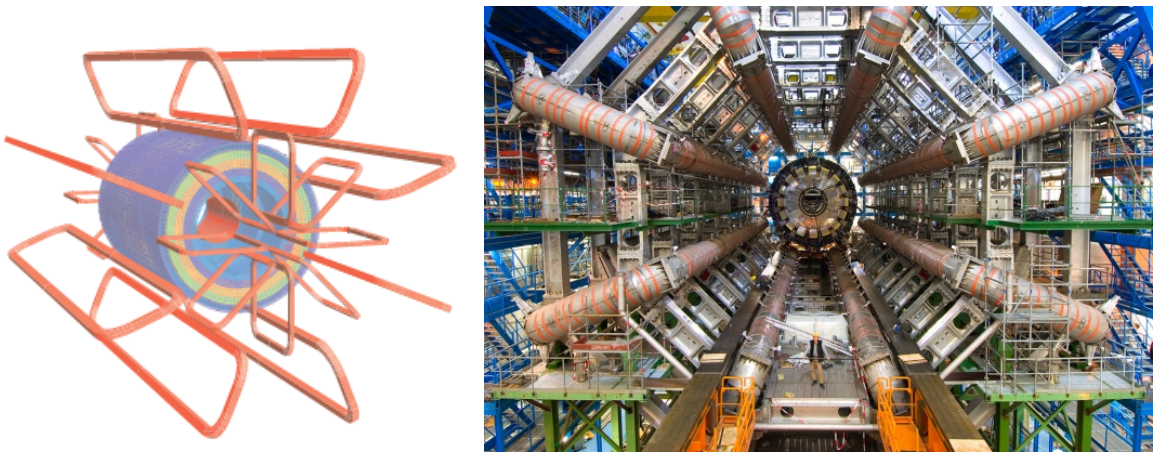

Figure 4.11: Left: Layout of the ATLAS magnets, including the solenioid as well as the barrel and endcap toroids. Right: The ATLAS barrel toroid, before installation of other subsystems.

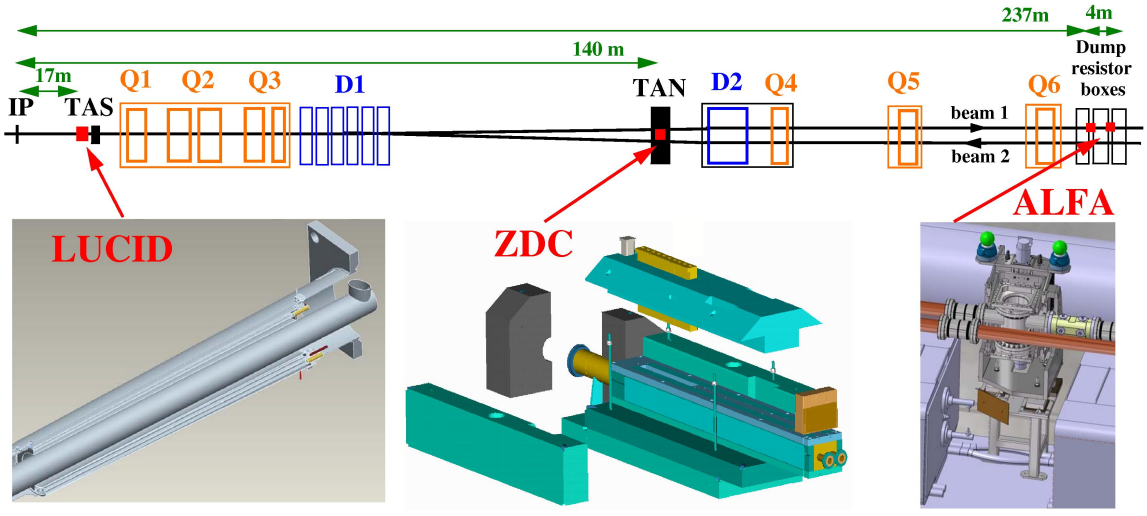

Figure 4.12: Layout of the three main forward detectors on ATLAS.

4.5 Forward Detectors

Several additional detectors are placed in the far forward region on ATLAS. The positioning of LUCID, ALFA, and the Zero Degree Calorimeter(ZDC) are shown in Figure 4.12. ZDC was not used during the 2012 proton-proton data taking period.

LUCID is primarily intended to provide luminosity measurements. LUCID (LUminosity measurement using Cherenkov Ionizing Detector) is a relative luminosity detector[10] which utilizes an array of Cherenkov tubes to detect inelastic p-p scattering in the region $5.6 < |\eta| < 6.0$.

ALFA (Absolute Luminosity For ATLAS), a scintillating-fiber tracker designed to provide an absolute cross section measurement by measuring elastic scattering at a 3 μrad angle from the beam axis. Due to the very small distance, ALFA can be used only during specially prepared beam conditions. For this reason, ALFA is housed in a series of 4 Roman pots, retractable vessels which can be used to bring the ALFA detector as close as 1 mm from the beam axis.

The Beam Condition Monitor (BCM), often considered part of the inner detector, is intended to monitor the beam stability, and can trigger a dump of the beam automatically if it detects instability in order to protect sensitive detector components. Located only 55 mm away from the beam axis (at z=$\pm$1.8 m), the BCM is built from radiation hard diamond sensors.

4.6 Trigger and Data Acquisition System

The LHC is designed to deliver filled bunch crossings with 25 or 50 ns spacing, implying a frequency of 20-40 MHz.[11] With a raw event size of 1.5 megabytes, this implies that several tens of terabytes of data would be produced by ATLAS every second. However, limitations in the data acquisition system prevent reading data from the detector at such a high rate. Instead, a three stage trigger system is integrated into the data readout chain [27].

[10]Relative in that it measures changes in luminosity over time, but it must be calibrated with absolute luminosity measurements from other sources.

This system is capable of making real time decisions on which collision events to record and which to reject, producing a total output of approximately 200 events per second.

The first stage of the trigger system, the Level-1 (L1) trigger is implemented using custom designed configurable hardware to select events at a rate of no more than 75 kHz, with the decision on a particular event arriving less than 2.5 μs after its associated bunch crossing. The L1 trigger utilizes coarse information from the muon trigger system and from dedicated calorimeter trigger towers which sum the inputs from several calorimeter cells. A configurable list of trigger criteria is applied, most of which test for the presence of high p_T physics objects.

Two software based trigger levels form the High Level Trigger system. The Level-2 (L2) trigger reads out more precise data from the detector in the regions of interest determined at L1, reducing the event rate to less than 3.5 kHz with decisions arriving within 40 ms of a bunch crossing. It utilizes a wider range of information from the ID, calorimeter, and muon system.

The final level of the trigger system, the Event Filter (EF), considers fully reconstructed events, selecting approximately 200 events per second within 4 seconds of the relevant bunch crossing.

Triggers with smaller p_T thresholds are used in many analyses and performance studies, especially in order to estimate the efficiency of triggers with higher thresholds. For these triggers, a prescale can be applied to accept only a fraction of events passing the trigger to prevent them from overwhelming the readout chain. Minimum bias triggers are also used to select events as randomly as possible and are used to study pile-up conditions among other things.

Many triggers on ATLAS are designed for monitoring data taking conditions. For example, large numbers of triggers during empty bunches may indicate the presence of noisy cells in the calorimeter, which may then be disconnected from the trigger system in real time. In addition, a dedicated LAr noise burst trigger chain allows for the identification

[11] Although not every bunch crossing is filled.

of noise bursts which create huge amounts of noise over a many channels in the LAr detector, typically lasting hundreds of μs[12].

The trigger configuration is normally adjusted to maintain the targeted trigger rates over time, with lower priority triggers being prescaled or removed at high luminosity. However, the ATLAS front end readout electronics are particularly sensitive to fluctuations in the L1 rate in particular. Thus, a system of both simple and complex deadtimes are used to protect the readout chain from triggering too quickly. Various components of the readout chain may also exert a busy flag, halting data taking across the entire detector if the data flow causes a buffer to fill up or if other problems are encountered.

[12]The cause of noise bursts is not understood.

Chapter 5

Object Identification and Reconstruction

The ATLAS detector is designed to detect and identify a range of physics objects which may be created by a proton-proton collision. While Chapter 4 described the design of the ATLAS detector, this chapter will continue by describing how the data produced by ATLAS may be utilized to identify and reconstruct these physics objects.

Of particular interest for this thesis are the observable decay products of top quarks: electons, muons, neutrinos (seen as 'missing transverse energy'), and jets. Figure 5.1 summarizes the response of the various ATLAS subdetectors to these and other physics objects.

5.1 Tracks and Vertices

Individual hits recorded by the ATLAS tracking detectors may be combined to form particle tracks. Each particle track is then extrapolated towards the center of the detector in order to determine whether it originated from the collision zone, or from the decay of a heavy particle outside of the collision zone (perhaps in the inner detector volume itself). Regions in the collision zone in which at least 3 tracks converge are identified as vertices. The vertex whose tracks have the highest $\sum p_T^2$ is assumed to be the hard scatter primary vertex. The remaining vertices are considered to have resulted from pile-up, described in

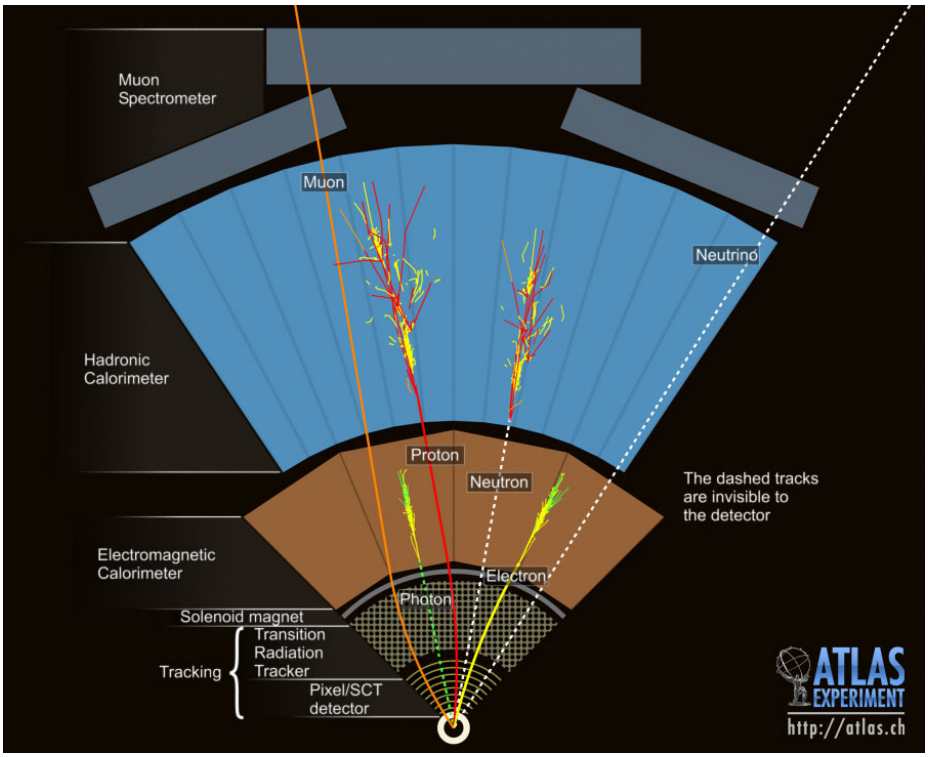

Figure 5.1: A cross section of the ATLAS detector showing the response of the various subdetectors to observable physics object which may be produced in a collision. Taken in aggregate, the data produced by these subdetectors may be used to identify the nature of these particles.

Chapters 3 and 4 as the products of the numerous collisions which occur in addition to the collision of primary interest.

5.2 Electrons

Electrons are identified from a combination of a high p_T charged track in the ID and an associated deposit in the electromagnetic calorimeter system. The electromagnetic calorimeter is divided into a grid of 'towers,' with each tower spanning a square of size 0.025 in $\eta - \phi$ coordinates. A sliding window algorithm [28] then identifies a 5x5 block of towers of the calorimeter where the total energy deposited is greater than 3 GeV, while a smaller region (3x3 towers) is used to locate the position of the cluster.

These energy deposits in the calorimeter are associated with the nearest track from the inner detector if one exists. A range of quality requirements are then imposed on the track and calorimeter cluster to determine whether it is consistent with an electron, with the tighter choices producing greater background rejection at the cost of lower efficiency. The criteria used include:

- The shape and width of the calorimeter energy deposit, as well as the presence of any punch-through to the hadronic calorimeter. For example, the presence of two energy peaks in the first layer of the calorimeter may indicate a pion decaying into two photons.
- The number and quality of tracker hits in the ID. Hits in the Pixel detector may be explicitly required to reduce contributions from photons converting into electrons inside the tracker.
- The distance between the energy deposit in the middle layer calorimeter layer and the extrapolated track from the inner detector.

In this analysis, the tightest quality level, Tight++,[1] is used. Additional requirements are imposed on electrons to further improve quality. The electromagnetic cluster is required to fall into a good region of the calorimeter: $|\eta| < 2.47$ excluding the transition between the barrel and endcaps at $1.37 < |\eta| < 1.52$. The transverse energy of the electron, $E_T = E_{cluster}/\cosh(\eta_{track})$, is reconstructed from the energy of the calorimeter deposit and the position of the track. This transverse energy is required to be at least 25 GeV. Furthermore, the electron track must have a distance of closest approach to the primary vertex, $|Z_0|$, less than 2 mm.

Finally, mini-isolation is applied to reduce the contribution from fake or non-prompt[2] electrons inside of jets. For this purpose, the mini-isolation variable is defined as $MI10 = \sum_{tracks} p_T$ for all tracks within a cone of radius $R < 10\ \text{GeV}/E_T$ around the electron track.

[1] '++' indicates that the selection has been optimized for use in the high pile-up environment seen during the 2012 data taking period.

The requirement that $MI10 < .05 * E_T^{electron}$ is then imposed. Mini-isolation was originally designed by the ATLAS $t\bar{t}$ resonance group to better handle cases where charged leptons are very close to or inside of jets due to the decay kinematics of high energy top quarks.

5.3 Photons

Like electrons, photons can be identified from energy deposits in the electromagnetic calorimeter using the same sliding window algorithm used to identify electrons. Photons which convert into an electron-positron pair in the inner detector produce one or two tracks originating from the tracker volume, while unconverted photons are not associated with charged particle tracks in the inner detector. In either case, the lack of a good track in the innermost layers of the tracker distinguishes photons from electrons. Additionally, photons tend to produce wider calorimeter showers than electrons.

5.4 Muons

Muons are identified on ATLAS from a pair of tracks left on the inner detector and muon tracker respectively. The relatively long lifetime of the muon (2.2×10^{-6} seconds), relatively large mass (105.6 MeV/c^2), and lack of a strong interaction implies that it will escape from the ATLAS calorimetry system and leave tracks in the muon tracker.

This analysis uses the ATLAS tight muon selection, which is based on the quality of the tracks reconstructed in the ID and muon system, and the degree of consistency between the two track fragments.

Muons with $p_T > 25$ GeV are accepted within the region $|\eta| < 2.5$. As with electrons, muon tracks are required to have originated from within 2mm of the primary vertex and to pass the mini isolation requirement $MI10 < 0.05 * p_T^{muon}$.

[2]Non-prompt leptons are those produced from the decay of particles in a jet. Prompt electrons are produced in the primary hard process of a collision.

5.5 Jets

As described in Section 1.3, confinement prevents quarks and gluons (partons) from existing in isolation, causing the creation of collimated showers of hadrons and other particles when high p_T quark or gluon is emitted from a collision. Jets are used to describe the resulting showers of particles which form distinctive patterns in the detector. Jets are reconstructed from tracks in the inner detector (roughly 1/3 to 1/2 of the the jet energy is carried by charged particles) and from energy deposits in the electromagnetic and hadronic calorimeters.

5.5.1 Jet Algorithms

Jets are defined by the jet algorithm chosen to find them, since the choice of jet algorithm is necessary to determination whether two energy deposits belong to the same or different jets [29; 30].

While jets are often described as resulting from the showering of a single parton produced in a collision, the concept of a parton lacks a precise definition and a precise relationship to detector observables, making it useful language but not a good foundation for a jet definition. (In contrast, electrons may be defined in terms of a concrete physical object which exists independently of our ability to identify it.) Additionally, in crowded final states such as a $t\bar{t}$ decay, the particle showers from multiple partons may become merged into a single jet. Final state radiation, in which high p_T particles emit additional particles, results in additional ambiguities which can not be resolved in the absence of a specific choice of algorithm.

All of the jet algorithms used in this analysis can be classified as sequential combination algorithms. These algorithms define a distance measure between two energy clusters and between any single energy cluster and the beam axis as given by Equations 5.1 and 5.3 respectively:

$$d_{ij} = min(p_{Ti}^{2p}, p_{Tj}^{2p})\frac{\Delta R_{ij}^2}{R^2}, \tag{5.1}$$

$$d_{ib} = p_{Ti}^{2p}, \tag{5.2}$$

$$\Delta R_{ij}^2 = (\eta_i - \eta_j)^2 + (\phi_i - \phi_j)^2. \tag{5.3}$$

The radius parameter, R, may be chosen freely and approximately determines the physical size of the jet in $\eta - \phi$ space. The behavior of the jet algorithm is also determined by the variable p, which is generally chosen as -1, 0, or 1.

Once the distance measure is defined, the jet algorithm proceeds by finding the smallest such distances in an event. If this distance is between two energy clusters, they are merged into a single cluster. Between a cluster and the beam axis (d_{ib}), the cluster is removed from the algorithm and defined to be a final state jet.

If $p = 1$ is chosen, this algorithm is called the inclusive k_t algorithm [31], so called because the distance measure is the transverse momentum of the softer cluster with respect to the harder one. Such a choice will result in a jet clustering which tends to merge the softest constituents first, preserving the substructure of a jet. This is an important property which will be taken advantage of in several algorithms presented in Sections 5.5.4 and 5.5.5. Although the k_t algorithm is a natural choice for simplifying cross section measurements, the irregular jet boundaries are strongly influenced by soft radiation in an event. These irregular boundaries can create problems for experimenters in evaluating detector coverage and calibration issues.

A choice of $p = -1$ results in the Anti-k_t [30] algorithm which tends to merge the hardest constituents first. Such an approach hides the substructure of a jet almost immediately. However, it produces roughly conical jets which are favored by experimentalists. Some of the weaknesses of such an approach can be compensated by maintaining a list of jet constituents for further analysis. As an additional benefit, potentially overlapping jet regions are automatically handled in a natural way, with harder jets claiming the greater portion of the overlap. For these reasons, the Anti-k_t algorithm is very widely used in the ATLAS collaboration.

The Cambridge/Aachen algorithm [32], equivalent to a choice of $p = 0$, is also occasionally used on ATLAS (although not in this analysis). This algorithm merges jet constituents based on angular ordering alone.

All three of these algorithms are infrared and collinear safe, a basic theoretical requirement that the final jets should not be strongly influenced by adding additional soft

(infrared) radiation or by splitting a single constituent into two lighter nearly collinear elements due to the difficulty in modeling such effects.

Figure 5.2 shows the jet area produced by several algorithms for an example event. The Siscone algorithm, a cone based jet algorithm, is also shown, although it is rarely used on ATLAS. The jet area is determined by including a homogeneous distribution of ghost particles with negligible energy into the jet clustering algorithm to determine which jet they are eventually associated with. Jet area is also an important variable used in jet calibrations in ATLAS. It is used to correct for the soft semi-homogeneous contributions to a jet's energy which results from pile-up.

5.5.2 Jet Selection

Two types of jets are used in this analysis. Small-R jets, intended to capture the radiation produced from a single high energy parton, are defined by the Anti-k_t algorithm with radius R=0.4. These jets are required to have $p_T > 25$ GeV, and jets with $p_T < 50$ GeV are required to have jet vertex fraction (JVF) > 0.5. The JVF, defined as the p_T-weighted fraction of the tracks associated with a jet which originate from the primary vertex, is useful for rejecting jets which are produced by pile-up.

Large-R jets are defined by the Anti-k_t algorithm with radius R=1.0. In this study they are intended to capture the entirety of a hadronically decaying high p_T (ie. boosted) top quark. A technique known as jet trimming [33] is applied to reduce the dependence on pile-up and several substructure algorithms are used to select jets which are consistent with having originated from a top quark decay. These are described in Sections 5.5.5 and 5.5.4 respectively.

With two different jet algorithms being considered, care must be taken that selected jets do not overlap in order to avoid a double counting of energy. This is achieved by requiring a minimum distance in $\eta - \phi$ space of 1.5 between large-R and small-R jets chosen for the final event reconstruction, as described in Section 5.7.

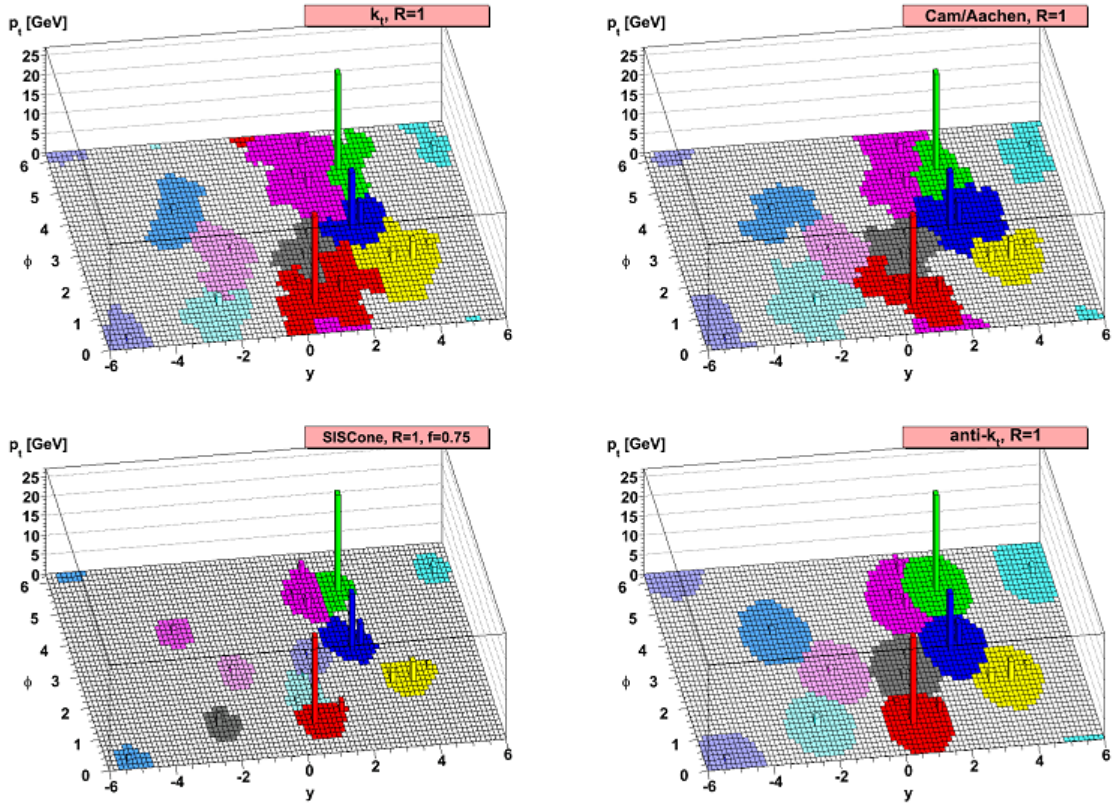

Figure 5.2: The resulting jet areas produced by several jet algorithms on the same parton-level event. The Anti-k_t algorithm produces jets with a roughly conical shape while jets formed by the k_t or Cambridge/Aachen algorithms show a more irregular shape. Jet areas are determined by clustering homogeneously distributed ghost particles along with the event's energy deposits. Figure thanks to Matteo Caccari, Gavin Salam, and Gregory Soyez [30].

5.5.3 b-tagging

Jets which contain a bottom quark (b-jets) are of special interest in this analysis. As top quarks decay primarily into bottom quarks and W bosons, the presence of one or more b-jets in an event increases the likelihood that such an event contained top quarks.

The identification of small-R jets which originated from a bottom quark, or b-tagging, utilizes a combination of calorimeter and tracking information [34; 35; 36; 37]. Such jets should contain one of a number of possible B hadrons: hadrons containing a b quark bound to one or two lighter quarks. Such hadrons have a lifetime of approximately 1.5×10^{-9} seconds, producing a displaced secondary vertex inside of the jet when they decay. In some cases a lepton may also be produced in this secondary vertex. Additionally, bottom quarks generally produce more massive, wider jets.

Several approaches to b-tagging are studied on ATLAS. For example, the SV1 (Secondary Vertex 1) algorithm fits a secondary vertex inside of a jet and produces a weight from several variables related to this vertex. The IP3D (Impact Parameter 3D) algorithm compares the longitudinal and transverse components of track impact parameters relative to the primary vertex to the expected distributions for prompt and non-prompt tracks. Finally, the JetFitter algorithm fits the entire decay chain of a B hadron, including secondary vertices.

This study utilizes the MV1 (MultiVariate 1) algorithm, which combines the outputs of the 3 algorithms mentioned in the previous paragraph using a neural network. The resulting weight then indicates the likelihood that a particular jet is a b-jet. Jets with MV1 value greater than 0.7892 are considered to be b-tagged in this analysis, a working point intended to yield a 70% efficiency. Figure 5.3 shows the b-tagging efficiency and background rejection rates for a range of working points.

5.5.4 Jet Substructure

Recent physics analyses on ATLAS and CMS increasingly focus on the internal 'structure' of jets in order to gain more information about a jet's origins. A jet may, for instance, be associated with a single parton emitted from a collision, or from several nearby

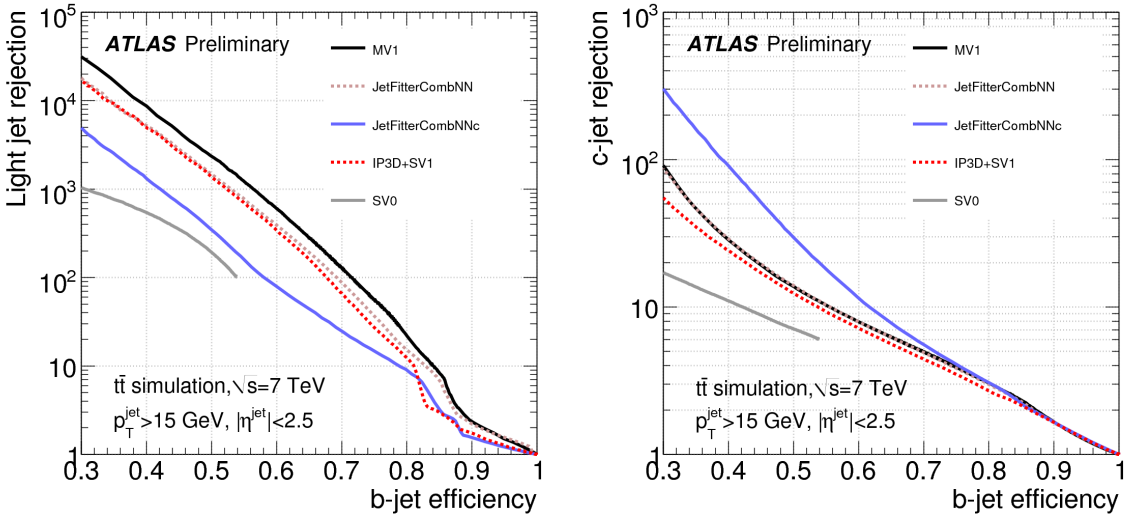

Figure 5.3: b-tagging background rejection shown as a function of efficiency. Left: rejection of light flavored jets. Right: rejection of charm jets. Shown for 2011 data [35].

partons.[3] In the second case, a great deal can be learned by studying the distribution of energy contained inside of a jet. A detailed performance study of the use of jet substructure on ATLAS, including the techniques used in this search, may be found in reference /citeAad:2013gja.

Jet substructure is particularly interesting in the context of identifying massive high p_T particles (such as top quarks and W bosons) decaying into several partons with little separation. In such cases, the radiation produced by multiple partons is likely to be captured inside of a single jet. While a large variety of substructure techniques were studied, two variables were identified as particularly interesting in the context of identifying high p_T top quarks: the jet mass and the first k_t splitting scale (Split12).

The jet mass is reconstructed from summing the four-momenta of each of a jet's constituents. While energy deposits in individual calorimeter cells are considered to be massless, the resulting loss in the mass of a jet is small compared to the contribution which arises from the separation between jet constituents. High p_T particles decaying into multiple partons will tend to produce jets with masses similar to that of the original particle.

[3]However, one must be careful; the concept of a parton and its relationship to a jet is not well defined!

Soft radiation which is widely separated from the hardest jet components will disproportionately impact the mass of a jet while having a minimal impact on that jet's momentum. This implies that pile-up may have a particularly severe effect on a jet's mass, especially those with a large radius. While the impact can remain relatively small for jets containing interesting substructure, this can dramatically increase the apparent mass of 'light' jets resulting from a single parton. The jet trimming technique, described in the following section, is therefore particularly important for studying the mass of large-R jets.

The second variable used in this search is the k_t splitting scale, Split12 [38]. This variable is calculated by reclustering the constituents of a jet using the k_t algorithm until a fixed number of remaining constituents is reached (normally two or three.) As the k_t algorithm clusters the hardest elements last, the final remaining constituents contain valuable information about the distribution of energy in a jet. In particular, the splitting scale is defined as:

$$\text{Split}_{ij} = \min(p_{Ti}, p_{Tj}) \times \Delta R_{ij}, \tag{5.4}$$

where i and j are sequential integers indicating the next subjets to be clustered by the k_t algorithm. Split_{12} thus represents the scale at which a pair of jets are merged into a single jet, while Split_{23} represents the scale at which three jets are merged into two. A large value for the k_t splitting scale therefore indicate the presence of multiple clusters of energy and is a strong indication that the decay products of a heavy boosted particle is contained within a jet.

5.5.5 Jet Trimming

The high pile-up environment experienced at the LHC presents a challenge to jet reconstruction. Although the jet vertex fraction allows for a discrimination between jets originating from the primary hard hard scatter and those generated from pile-up, significant challenges remain. By depositing additional energy in the calorimeter, pile-up contaminates jets, impacting their observable properties. A technique known as pile-up subtraction is used to reduce this impact by estimating the amount of pile-up energy in each event and subtracting energy from each jet according to its jet area. Such an approach substantially

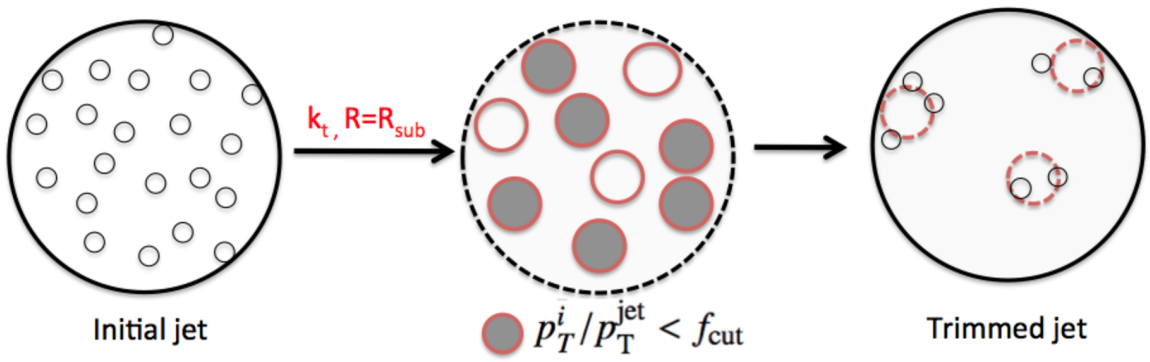

Figure 5.4: Illustration of the jet trimming procedure.

reduces the average dependence of jet properties on pile-up, but can not correct for the loss of resolution introduced to key observables due to local fluctuations in the amount of pile-up.

The impact of pile-up on jet p_T scales linearly with the area of a jet, while the impact on the mass for a jet with no significant substructure scales with R^3, and is thus especially problematic once large-R jets are considered. However, jet trimming may be utilized in order to reduce the effective jet area while maintaining a jet's large reach for capturing hard radiation. The jet trimming procedure is as follows:

- Recluster the constituents of a jet using a k_t algorithm with radius $R_{sub} < R_{jet}$ to obtain a set of subjets.
- Remove all subjets i with $p_{Ti}/p_T^{jet} < f_{cut}$ for some choice of f_{cut}.
- Recombine the remaining subjets into a final trimmed jet.

This procedure, illustrated in Figure 5.4 has been demonstrated to keep the small portions of a jet which contain the hardest radiation which results from the hard process of a collision. Meanwhile, by reducing the effective area of a jet, this algorithm reduces the amount of soft, diffuse pile-up contamination.

This analysis uses $R_{sub} = 0.3$ and $f_{cut} = 0.05$, values which were chosen based on studies of the dependence of jet observables and their resolution on the level of pile-up in an event

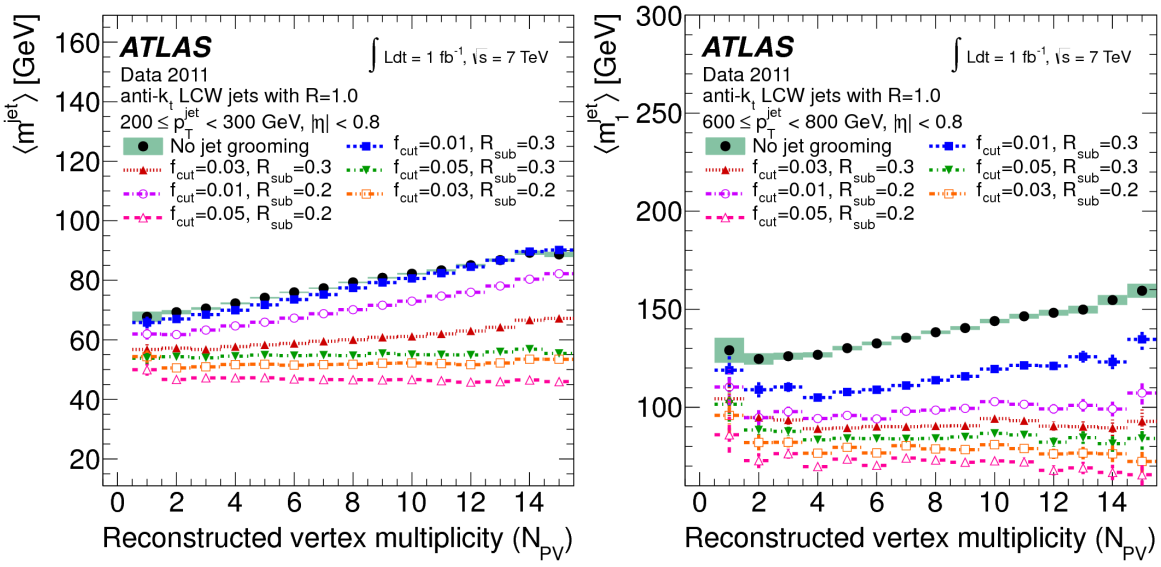

(a) 200 GeV$< p_T^{jet} <$ 300 GeV (b) 600 GeV $< p_T^{jet} <$ 800 GeV

Figure 5.5: Mean jet mass for Anti-k_t R=1.0 jets in the central region $|\eta| < 0.8|$ as a function of the reconstructed vertex multiplicity before and after applying jet trimming for several choices of parameters. Jet trimming significantly reduces the dependence of the jet mass on pileup [39].

[39]. For example, Figure 5.5 shows the evolution of jet mass with the number of vertices in an event for several choices of parameters.

Figure 5.6 demonstrates that jet trimming can improve the jet mass resolution of jets containing a top quark decay while improving the separation between signal and background in relevant jet properties. Figure 5.7 shows a comparison of the impact of trimming on jet mass between data and simulation after applying a $t\bar{t}$ selection.

5.6 Missing Transverse Energy

The final object to be reconstructed on ATLAS is missing transverse energy. As was mentioned in previous sections, neutrinos are the only known particles which can not be directly detected on ATLAS. However, the presence of a neutrino can be inferred indirectly

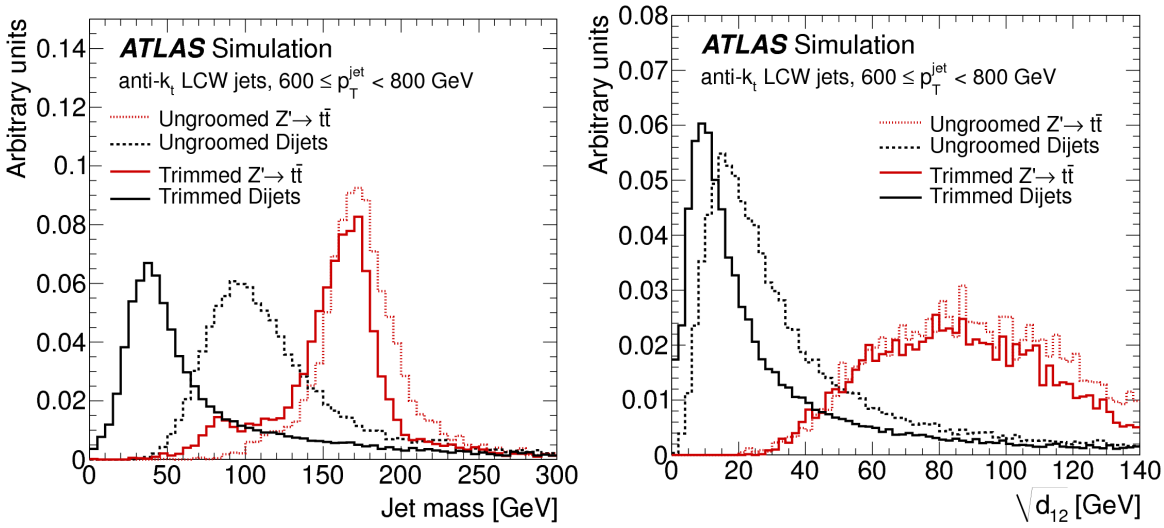

(a) Jet Mass (b) Split12

Figure 5.6: Impact of jet trimming on (a) jet mass and (b) Split12 of leading Anti-k_t R=1.0 jets with 600 GeV $< p_T <$ 800 GeV. Shown for a simulated dijet background (black) and a 1.6 TeV Z' signal (red) before and after applying trimming (solid and dotted lines respectively) [39].

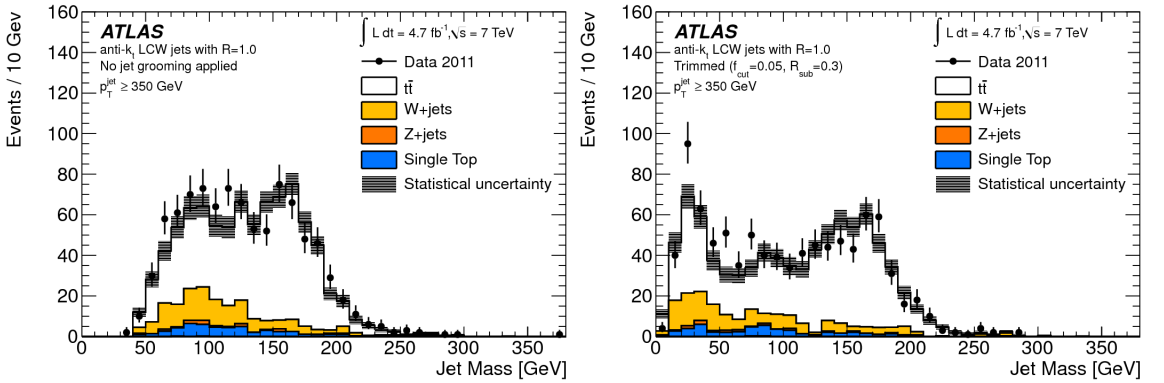

(a) Ungroomed Anti-k_t R=1.0 Jets (b) Trimmed Anti-k_t R=1.0 Jets

Figure 5.7: Comparison of the leading jet mass between data and Monte Carlo simulation for (a) ungroomed jets and (b) trimmed jets ($f_{cut} = 0.05$, $R_{sub} = 0.3$) after applying an early iteration of $t\bar{t}$ selection on 7 TeV data and Monte Carlo simulation. Shown for the Anti-k_t jet algorithm with R=1.0 [39].

through the presence of an imbalance in the transverse energy of an event, referred to as $E_{\mathrm{T}}^{\mathrm{miss}}$.

$E_{\mathrm{T}}^{\mathrm{miss}}$ is calculated from a combination of all observable objects reconstructed in the detector together with specially prepared weights and calibrations to minimize the potential overlap between objects [40].

5.7 Electron-Jet Subtraction and Object Overlap Removal

Since all of the objects described in this chapter are reconstructed from a combination of calorimeter deposits and tracks in the ID and muon system, they can not be considered to be independent from each other and a procedure is needed to remove the overlap between objects. For example, an electron will deposit energy in the calorimeters which will be picked up by jet finding algorithms and included in nearby jets. Meanwhile, jets may produce fake or non-prompt electrons and muons from the decay of heavy hadrons or from electromagnetic radiation. Finally, charged hadrons may leave tracks in the ID and thus fake an electron.

The decay of highly boosted top quarks will tend to produce electrons in very close proximity to or contained inside of jets. This implies that an additional procedure is needed to resolve these two objects in a consistent way while avoiding the loss of efficiency which would result from rejecting electrons or jets which are too close to each other. Thus, the following procedure has been developed to handle the overlap between selected physics objects (all objects are required to have $p_T > 25$ GeV):

- Subtract energy and momentum of each electron from the nearest jet within a distance of 0.4 in $\eta - \phi$ coordinates.
- If the distance between a jet and an electron is less than 0.2 after the electron subtraction and if the jet p_T is still above 25 GeV then return the electron energy and momentum to the jet and reject the electron.
- Re-evaluate the JVF cut on any jet which has had an electron subtracted (since both momentum and the JVF may have changed).

- Reject muons within a distance of 0.1 of a nearby jet.

Chapter 6

Data Taking and Preparation

This study was performed on data taken by the ATLAS detector during the 2012 data taking period. During this period, the LHC delivered proton-proton collisions at a center-of-mass energy of 8 TeV. A total integrated luminosity of 22.8 fb^{-1} of stable collisions were delivered to ATLAS during this time, of which 21.3 fb^{-1} was recorded. Approximately 1.5 fb^{-1} of integrated luminosity was lost due to inefficiency in the data acquisition system or due to the 'warm start:' the time required for the ID to transition to data taking mode after stable beams are achieved in the LHC.[1]

A portion of this data must be rejected due to a variety of circumstances leading to unsatisfactory data taking conditions. For example, LAr noise bursts, high voltage trips or other problems may result in unacceptable levels of noise in the detector. Alternatively, if an unacceptably large portion of an ATLAS subdetector is unable to take high quality data for any reason or if ATLAS magnets are not at their intended strength then data is not used.

Figure 6.1a shows the integrated luminosity delivered to ATLAS in 2012, as well as the portion recorded and considered to be of high quality. During this period, proton bunches were spaced 50 ns apart in the LHC, with some larger gaps between bunch trains. Achieving

[1]In order to avoid damaging the detector, the ID ramps down its high voltage and the pixel detector turns off its preamplifiers during periods when beams are potentially unstable, especially after protons are injected into the LHC but before they achieve a stable orbit many minutes later. Thus, a warm start must be initiated after the LHC declares stable beams.

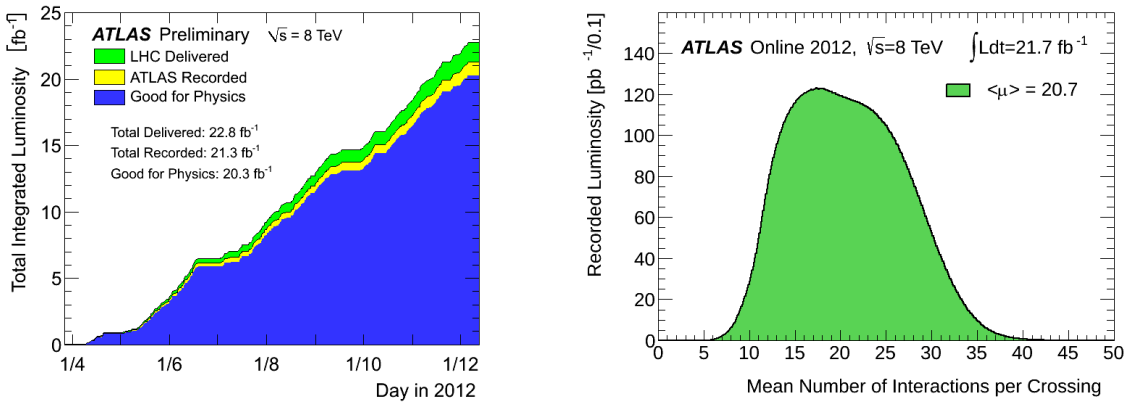

(a) (b)

Figure 6.1: Left: Integrated luminosity of proton-proton collisions delivered to and recorded by the ATLAS detector during 2012, as well as the portion considered of high quality for physics analyses. Right: Mean number of interactions per crossing, μ, weighted according to luminosity. The average number of collisions per crossing varies over time, between fills, and between individual proton bunch crossings in a given fill.

such a high luminosity implies creating large number of collisions per bunch crossing. The the mean number of collisions per bunch crossing, μ, is continuously measured for each pair of filled bunches. The distribution of μ is shown in Figure 6.1b.

As explained in Section 4.6, collisions are only recorded if they are selected by the trigger system. These events are then sorted into one or more data streams depending on the particular trigger items which selected the event. For example, the Muon stream is seeded by triggers intended to select events containing high p_T muons, while the Egamma stream captures events containing electrons or photons. Many of the triggers in these streams were active for essentially all of the 2012 data set.

The final stream used in this analysis, the Delayed stream, is dedicated to lower priority triggers which are enabled or disabled depending on the available bandwidth in the data readout chain at a particular time (ie. depending on the instantaneous luminosity.) These triggers may also be 'prescaled' such that only a fraction of the events passing a given trigger

are kept. For example, the EF_j220_a10tcem_delayed trigger used in this analysis was active during data taking periods corresponding to roughly 17 fb^{-1} of integrated luminosity.

Chapter 7

Monte Carlo and Physics Simulation

Many expected background and signal processes which may be produced in proton-proton collisions as well as the expected response of the ATLAS detector are modeled through the use of Monte Carlo techniques [41]. These simulations are used to guide the optimization of selection and reconstruction procedures described in Chapters 5 and 8. In addition, accurate background estimates are necessary for correct interpretation of the experimental results.

Monte Carlo event generation is commonly performed in several stages. A "matrix element step" models a hard process by evaluating the most significant terms in a perturbative expansion (i.e. via the computation of Feynman diagrams) with a fixed number of incoming and outgoing particles. Additional stages model the parton showering and hadronization. Initial and final state radiation produced by incoming and outgoing particles from the hard process and additional interactions between the remaining fragments of the colliding protons (the "underlying event") are also included.

Once an event is generated, a GEANT4 based simulation is used to model the response of the ATLAS detector as the emitted particles move away from the collision zone [42]. The simulated events are then processed by the ATLAS reconstruction software.

7.1 Monte Carlo Generators

One major challenge facing the production of reliable Monte Carlo events is the large final state jet multiplicity produced in collisions at the LHC, with events containing six or more high transverse momentum (p_T) jets common. In general, any process can be produced with several additional jets.

Traditional Monte Carlo Generators are '$2 \to 2$' generators which model a hard process with exactly two outgoing particles while allowing additional jets to be produced in the parton shower. PYTHIA [43; 44] and Herwig++ [45] are both widely used standalone '$2 \to 2$' generators which are capable of modeling all stages of event production. PYTHIA employs either a virtuality or p_T ordered approach to the parton shower, while Herwig's parton shower uses angular ordering.

While such an approach is successful in modeling many processes, it is generally difficult to accurately describe events with multiple additional hard jets produced during the parton shower stage. More recently, a number generators have been developed which are capable of modeling hard processes with multiple outgoing particles. In order to capture the full range of possible jet multiplicities, these '$2 \to n$' generators combine samples generated with different numbers of outgoing particles in the matrix element. However, this gives rise to an ambiguity as the same jet can be generated by either the parton shower or the matrix element steps. This ambiguity must be resolved in order to prevent a double counting of events.

Two approaches exist for determining which jets should be generated by the matrix element and which by the parton shower. MLM matching, implemented in the ALPGEN generator, allows the event evolution to proceed without restriction but afterwards vetoes events whose hard jets do not match the parton-level quarks and gluons produced in the matrix element step [46]. CKKW matching [47], implemented in SHERPA, suppresses the production of soft jets in the hard process and hard jets during the parton shower phase according to the $k_\perp$ scale of each individual branch splitting as the event is generated [48]. Although CKKW matching has often been considered to be theoretically preferred over MLM matching, in many cases ALPGEN has produced stronger agreement with data than

SHERPA.[1] SHERPA uses its own parton showering and hadronization model similar in nature to PYTHIA. ALPGEN can be partnered with either PYTHIA or Herwig for these stages of event generation.

POWHEG [49] and MC@NLO [50] are both next-to-leading order (NLO) '$2 \rightarrow 2$' generators which are used to improve the modeling of certain hard processes by including higher order Feynman diagrams containing closed loops in the hard process. Likewise, MADGRAPH is a '$2 \rightarrow n$' generator which can model hard processes with several outgoing particles [51; 52]. ACERMC, a leading order '$2 \rightarrow 2$' generator, is occasionally used by the ATLAS collaboration as well [53]. POWHEG, MC@NLO, MADGRAPH, and ACERMC must also be paired with a parton shower model such as PYTHIA or Herwig to model additional stages of the event generation. The particular Monte Carlo samples used in this analysis are described in Chapter 9

[1] However, the accuracy of both generators is likely to be improved with further tuning.

Chapter 8

Event Selection and Reconstruction

This chapter describes how ATLAS collision events are selected, sorted into several channels and reconstructed as semileptonic $t\bar{t}$ candidates. Two sets of selection channels are optimized for reconstructing moderate or high p_T top quarks, referred to as the resolved and boosted channels respectively. In order to avoid overlap, only events which fail the boosted selection are considered in the resolved selection. Additionally, events may contain either an electron or a muon, and may fall into one of three exclusive categories depending on the presence of b-tagged jets.

Thus, $t\bar{t}$ candidates are sorted into one of twelve statistically independent channels. Afterwards, the invariant mass ($m_{t\bar{t}}$) of the $t\bar{t}$ pair is calculated, and statistical tests are applied as described in Chapter 12.

8.1 Preselection

All available events taken during good ATLAS data taking conditions during the 2012 proton-proton data taking period are considered. Incomplete events, events with corrupted data from Tile, or those occurring too close to a noise burst in the LAr calorimeter are removed.

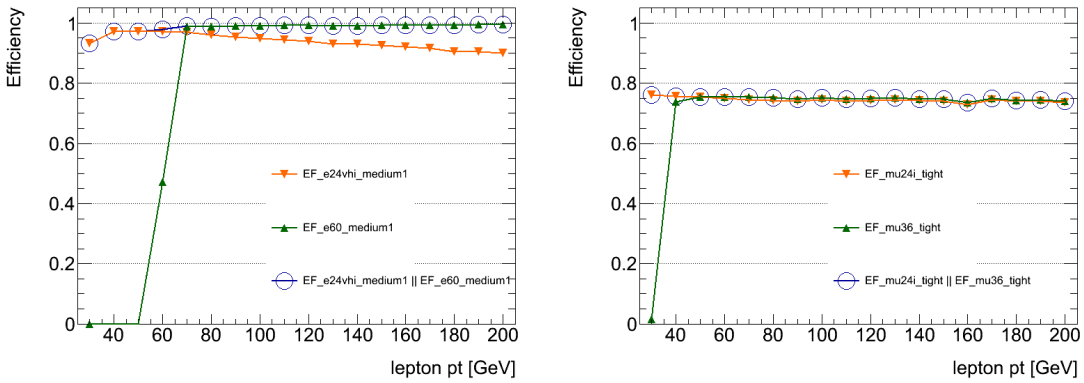

(a) Electron Trigger Efficiency

(b) Muon Trigger Efficiency

Figure 8.1: Lepton Trigger efficiencies for a SM $t\bar{t}$ sample.

In the electron channel, events are required to pass at least one of the EF_e24vhi_medium1 or EF_e60_medium1 trigger items. These triggers are designed to identify events containing an isolated electron with $p_T > 24$ GeV or any electron with $p_T > 60$ GeV. Figure 8.1a shows that the electron trigger efficiency is very high and stable over a wide range in p_T.[1]

The muon channel utilizes three trigger items. Similarly to the electron channel, two triggers are taken: the EF_mu24i_tight and EF_mu36_tight triggers are designed to capture events containing isolated and non-isolated muons with p_T above 24 and 36 GeV respectively.

The muon trigger efficiency, shown in Figure 8.1a, is lower than for electrons due to limitations of the muon trigger system. For this reason, the muon triggers are supplemented by an additional trigger from the ATLAS delayed stream. The EF_j220_a10tcem_delayed trigger selects events containing a large-R (R=1.0) jet with $p_T > 220$ GeV. This trigger item was included during roughly 17.3 fb^{-1} of data taking in 2012. The efficiency of the large-R jet trigger is shown in Figure 8.2, while the gain in selection efficiency is shown in Figure 8.3.

[1]The trigger efficiency is defined as the fraction of good electrons, as defined in in Chapter 5, which may be associated with a trigger object.

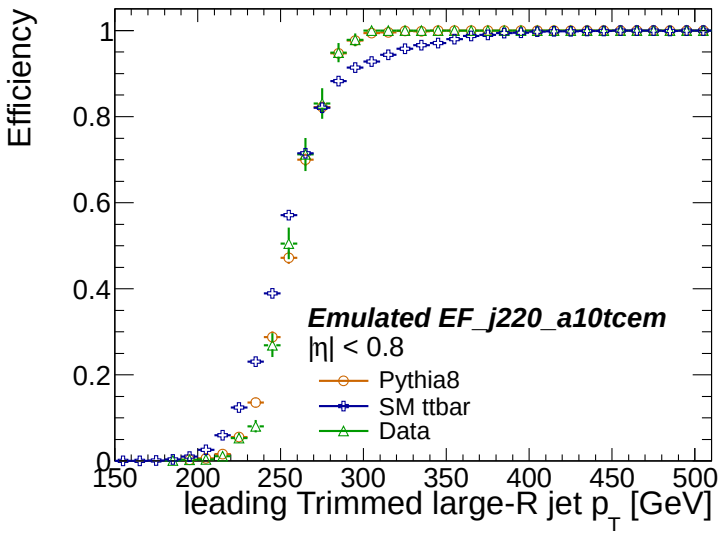

Figure 8.2: Efficiency of the large-R jet trigger on events passing an inclusive jet selection. Differences between SM $t\bar{t}$ and multijet events (PYTHIA8) are due to differences in the jet shapes and the use of a smaller jet radius in the level 2 trigger.

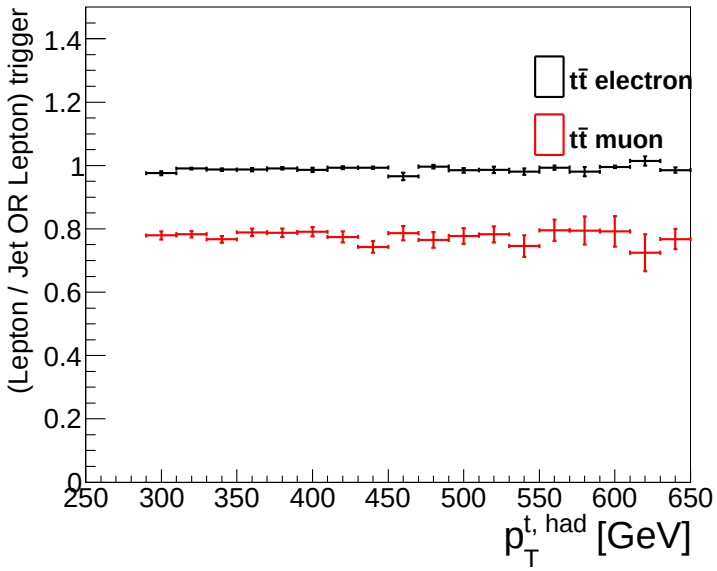

Figure 8.3: Ratio of efficiencies when using lepton triggers only compared to the combination of lepton triggers and the large-R jet trigger. Large-R jet trigger efficiency has been adjusted to reflect the fact that it is available for only 17.3 fb^{-1} of data.

The following selection criteria are applied to all events passing the trigger requirements. Only physics objects surviving the object overlap removal described in Section 5.7 are counted.

- Primary vertex with at least 4 tracks satisfying $p_T > 400$ MeV.
- Exactly one electron or muon with $p_T > 25$ GeV matching a trigger object. No matching is required in events passing the delayed trigger in the muon channel.
- No small-R (anti-k_t R=0.4) jets failing the LooseBadMinus quality criteria.
- $E_T^{miss} > 20$ GeV.
- $M_T^W + E_T^{miss} > 60$ GeV, where M_T^W is the transverse mass of the leptonically decaying W boson, as explained in Section 8.2

8.2 Leptonic W Boson Reconstruction

A leptonic W boson candidate is reconstructed from the selected lepton and missing transverse energy. The E_T^{miss} is assumed to have come from a neutrino, and the z component of the neutrino's momentum is reconstructed by assuming that the W boson has exactly 80.4 GeV of mass. This yields a quadratic equation which can be solved to find $p_{z,nu}$:

$$M_w^2 = (E_{nu} + E_{lepton})^2 - (\vec{P}_{nu} + \vec{P}_{lepton})^2 \tag{8.1}$$

If a single real solution to Equation 8.1 exists, then it is chosen. Otherwise, if two solutions exist the solution with the smallest $|p_z|$ is chosen in the boosted channel, while both solutions are considered in the resolved channel. Finally, if no real solutions are found, then the E_T^{miss} is rotated and scaled to find a solution [54].

8.3 Resolved Channel: Selection and Event Reconstruction

The resolved channel is optimized to search for $t\bar{t}$ resonances with moderate masses in the approximate range of 400 GeV to 1 TeV. This channel searches for the individual

decay products of one hadronically and one leptonically decaying top quark in an event. In addition to the preselection listed above, events are required to contain at least 4 small-R jets with $p_T > 25$ GeV. At least one of these jets is required to be b-tagged ($MV1 > .7892$).

Events satisfying these requirements must then be reconstructed into hadronically and leptonically decaying top quark candidates. The hadronically decaying top quark should be composed of three jets: two associated to a hadronically decaying W boson and a third to the accompanying b quark. The leptonically decaying top quark is reconstructed from a single jet (also assumed to originate from a b quark) and a leptonically decaying W boson candidate. At least one of the selected jets is required to be b-tagged.

8.3.1 χ^2 Algorithm

In order to reconstruct the $t\bar{t}$ pair in an event, it is necessary to identify the combination of objects in the event which are most likely to have resulted from the decay of a $t\bar{t}$ pair. This is especially important because most $t\bar{t}$ events will contain more than the minimum number of jets. In addition, most events contain two possible leptonic W boson candidates, an ambiguity which must be resolved in order to calculate the invariant mass of the $t\bar{t}$ pair. For this purpose, a χ^2 algorithm is used to test every possible combination of jets and W boson candidates. The χ^2 itself is constructed from constraints on the expected properties of the reconstructed top quarks and W bosons:

$$\chi^2 = \left[\frac{m_{jj} - m_W}{\sigma_W}\right]^2 + \left[\frac{m_{jjb} - m_{jj} - m_{th-W}}{\sigma_{th-W}}\right]^2 + \left[\frac{m_{jl\nu} - m_{tl}}{\sigma_{tl}}\right]^2 + \left[\frac{(P_{T,jjb} - P_{T,jl\nu}) - (P_{T,th} - P_{T,tl})}{\sigma_{diffpT}}\right]^2 \quad (8.2)$$

The first two terms represent the mass constraint from the hadronically decaying W boson and top quark candidates respectively, with the second term chosen to minimize the correlation between the two components. Likewise, the third term is the mass constraint from the leptonically decaying top quark, while the fourth term reflects the expectation that a resonance should produce top quarks which are approximately balanced in p_T.

The parameters in Equation 8.2 are determined from studies of simulated Z' resonances with masses ranging from 500 GeV to 2 TeV and are summarized in Table 8.1.

Parameter	Value	Description
m_W	82.4 GeV	Expected mass of reconstructed hadronically decaying W Boson
m_{th-W}	89.0 GeV	Expected mass of reconstructed hadronically decaying top quark, less the W boson
m_{tl}	166.0 GeV	Expected mass of reconstructed leptonically decaying top quark
$p_{T,th} - p_{T,tl}$	0.43 GeV	Expected difference between the hadronically and leptonically decaying top quarks p_T
σ_W	9.6 GeV	Expected standard deviation of hadronically decaying W Boson mass
σ_{th-W}	15.7 GeV	Expected standard deviation of hadronically decaying top quark constraint
σ_{tl}	17.5 GeV	Expected standard deviation of leptonically decaying top quark mass
σ_{diffpT}	46.1 GeV	Expected standard deviation of the p_T difference between the hadronically and leptonically decaying top quarks

Table 8.1: Summary of parameters used in the χ^2 formula used to reconstruct $t\bar{t}$ candidates in the resolved channel. Values reflect the mean and standard deviation of observed quantities in simulated Z' samples with a range of masses.

The χ^2 is then evaluated for every possible permutation of selected jets and W boson candidates which satisfy the requirement that the jet associated to the b quark from at least one of the top quark candidates is b-tagged. The choice which results in the smallest χ^2 value is chosen to assign the detected objects to $t\bar{t}$ decay products. A final cut is then made by requiring $\log_{10}(\chi^2) < 0.9$ to remove badly reconstructed events.

This cut was demonstrated both to reduce background sources which do not result from $t\bar{t}$ events, and to reduce the contribution arising from $t\bar{t}$ events which are not properly reconstructed. In particular, picking the wrong combination of jets may result in a

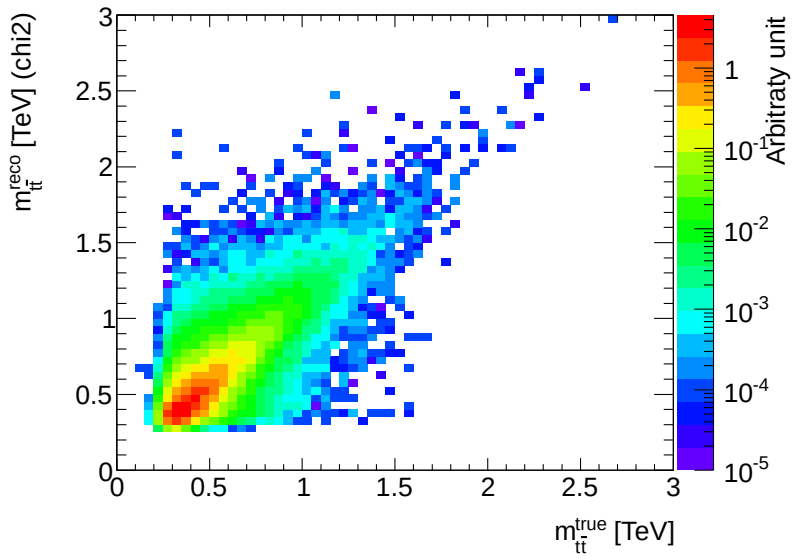

Figure 8.4: Reconstructed $m_{t\bar{t}}$ compared to the true $t\bar{t}$ invariant mass for simulated SM $t\bar{t}$ events reconstructed with the χ^2 algorithm.

reconstructed invariant mass which is much larger than the true value. Since the expected background is steeply falling in $m_t\bar{t}$, this results in a significant increase in the number of events at high $m_t\bar{t}$ where the signal is expected.

The invariant mass of the reconstructed $t\bar{t}$ pair is then calculated from the decay products of the $t\bar{t}$ candidate. Figure 8.4 shows the reconstructed value of $m_{t\bar{t}}$ compared to the true $t\bar{t}$ invariant mass for a SM $t\bar{t}$ sample. The $m_{t\bar{t}}$ resolution is presented in Figure 8.5 for several Z' boson masses.

Once an event has been selected, it is assigned to one of three categories in order to take advantage of different signal to background ratios in each one:

- Category 1: The b-jet associated to both the hadronically and leptonically decaying top quarks is b-tagged.
- Category 2: Only the b-jet associated to the hadronically decaying top quark is b-tagged.
- Category 3: Only the b-jet associated to the leptonically decaying top quark is b-tagged.

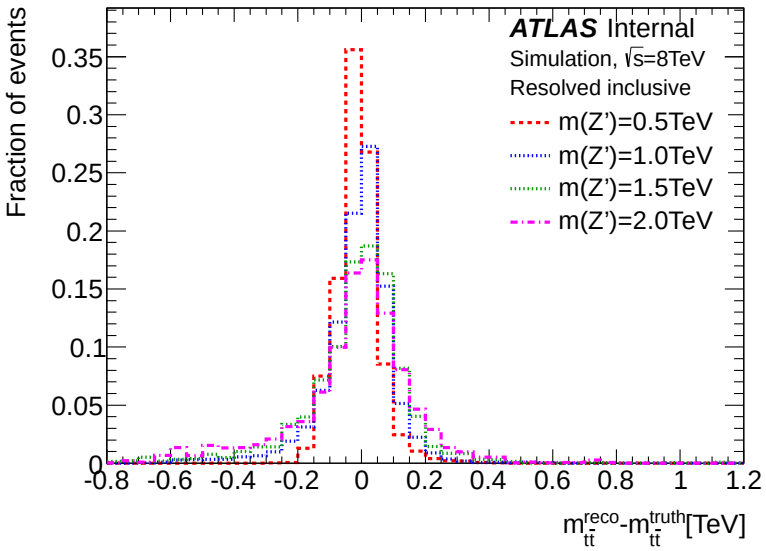

Figure 8.5: Difference between the true and reconstructed invariant mass for simulated Z' bosons reconstructed with the χ^2 algorithm.

8.3.2 Reconstruction Efficiency

The effectiveness of the χ^2 algorithm is evaluated on a SM $t\bar{t}$ sample. 'Reconstructable' semileptonic $t\bar{t}$ events are those in which all of the $t\bar{t}$ decay products are matched to reconstructed objects according to the following criteria:

- Each quark must be matched to a 'truth' jet with $p_T > 4$ GeV and $|\eta| < 5$ within a distance $\Delta R < 0.4$. Truth jets are those which result from applying a jet clustering algorithm to the particles produced by a Monte Carlo generator after the parton shower and hadronization but before applying detector modeling and reconstruction. These truth jets must then be matched to a reconstructed jet, again within $\Delta R < 0.4$. Multiple quarks may be matched to the same jet.

- The truth lepton produced in the Monte Carlo Generator must be matched to a reconstructed lepton within $\Delta R < 0.4$.

- The neutrino must be matched to the $E_{\mathrm{T}}^{\mathrm{miss}}$ within $\Delta\phi < 1.0$.

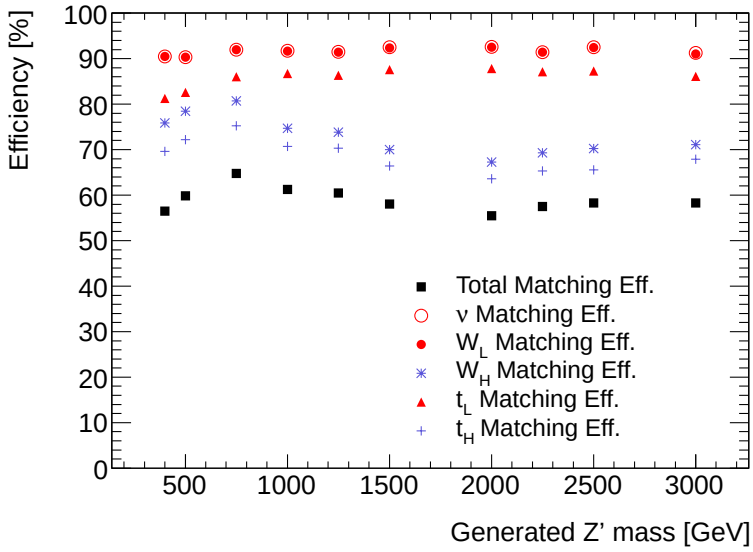

Figure 8.6: Fraction of semileptonic $t\bar{t}$ events which are determined to be reconstructable (i.e. those for which all truth level objects can be matched to reconstructed object). Also shown is the matching efficiency to hadronically and leptonically decaying top quarks and W bosons individually.

Figure 8.6 shows the fraction of events in a SM semileptonic $t\bar{t}$ sample which are determined to be reconstructable. Figure 8.7 shows the efficiency of the χ^2 reconstruction algorithm to identify the correct combination of decay products in reconstructable events.

8.4 Boosted Channel: Selection and Reconstruction

The strategy used in the resolved channel is not adequate for the identification and reconstruction of high mass resonances which decay to pairs of top quarks with high p_T. In such cases, the decay products of high p_T top quarks will be clustered tightly together and it is often not possible to resolve them into separate objects, particularly on the hadronic side of the event. Additionally, final state radiation in which a parton resulting from the decay of a hadronically decaying top quark radiates an extra gluon is increasingly important at higher energies. Including such additional radiation which may not be captured by a small-R jet improves the resolution of reconstructed variables such as the top p_T and mass.

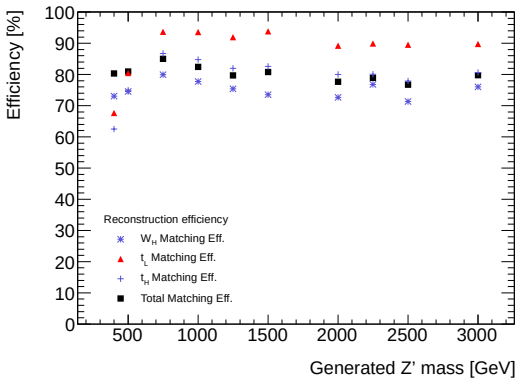

(a) Z'

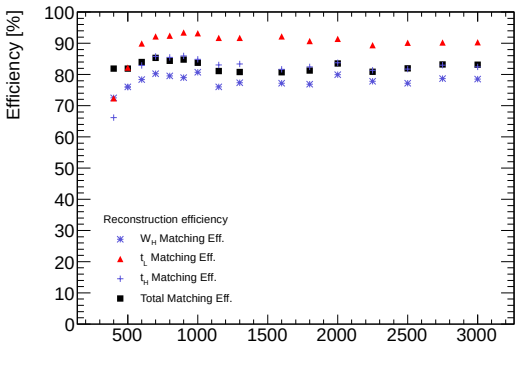

(b) KK Gluon

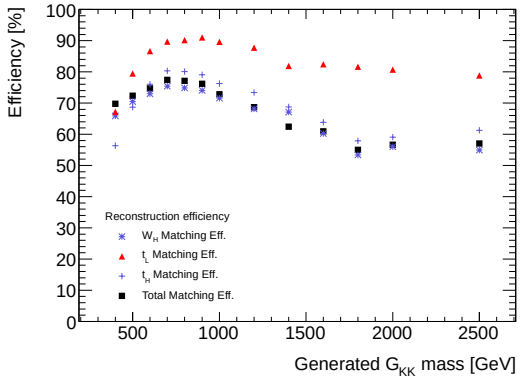

(c) KK Graviton

Figure 8.7: Efficiency to select the correct combination of jets in reconstructable events which pass the resolved selection but fail the boosted selection, by signal type and resonance mass.

Finally, the kinematics of high p_T top quark decays provide additional handles which may be taken advantage of in order to resolve the ambiguities in reconstructing $t\bar{t}$ events.

For this reason, the boosted channel is optimized to search for $t\bar{t}$ resonances with invariant masses greater than roughly 0.75-1 TeV, with each top quark having $p_T > 300$ GeV. This channel provides better $t\bar{t}$ invariant mass resolution and better background rejection compared to the resolved channel for such events.

In addition to the common preselection described in Section 8.1, events are required to have at least one small-R jet with $p_T > 25$ GeV within a distance $\Delta R < 1.5$ from the

lepton. If one or more such jets exists, the one with highest p_T is chosen and assumed to have resulted from the leptonic decay of a top quark, and is labeled as the "leptonic jet."

The hadronically decaying top is then reconstructed with the help of a large-R (Anti-k_t R=1.0) jet algorithm. In order to reduce the dependence on pile-up, jet trimming is applied to all large-R jets in the event, as described in Section 5.5.5.[2] Large-R jets are then required to satisfy the following requirements, with all of the jet properties evaluated after trimming:

- Jet $p_T > 300$ GeV (or 380 GeV if an event fails the leptonic triggers but passes the delayed trigger.)
- Jet mass > 100 GeV.
- $\text{Split}_{12} > 40$ GeV.
- $\eta < 2.0$.
- ΔR(large-R jet,leptonic jet) > 1.5.
- $\Delta\Phi$(large-R jet,lepton) > 2.3.

The last two requirements are imposed to ensure that the leptonically and hadronically decaying tops are widely separated from each other, as expected for a high mass $t\bar{t}$ resonance. The second to last requirement additionally ensures that there is no double counting of energy between the selected small-R and large-R jets. If at least one such large-R jet satisfies the selection the jet with the highest p_T is chosen and assumed to contain the decay products of the hadronically decaying top. If no such jet exists then the event is rejected.

As in the resolved channel, selected events are split into 3 categories, depending on whether b-tagged jets are associated to the leptonically decaying top, hadronically decaying top, or both. A b-tagged jet is associated to the hadronically decaying top if it is within a distance (ΔR) of 1.5 of the selected large-R jet, or the leptonically decaying top if it is the highest p_T jet near the lepton. No ambiguity exists in reconstructing $t\bar{t}$ pairs in the boosted channel.

[2]Large-R jets resulting from top quark decays typically contain 2-4 subjets.

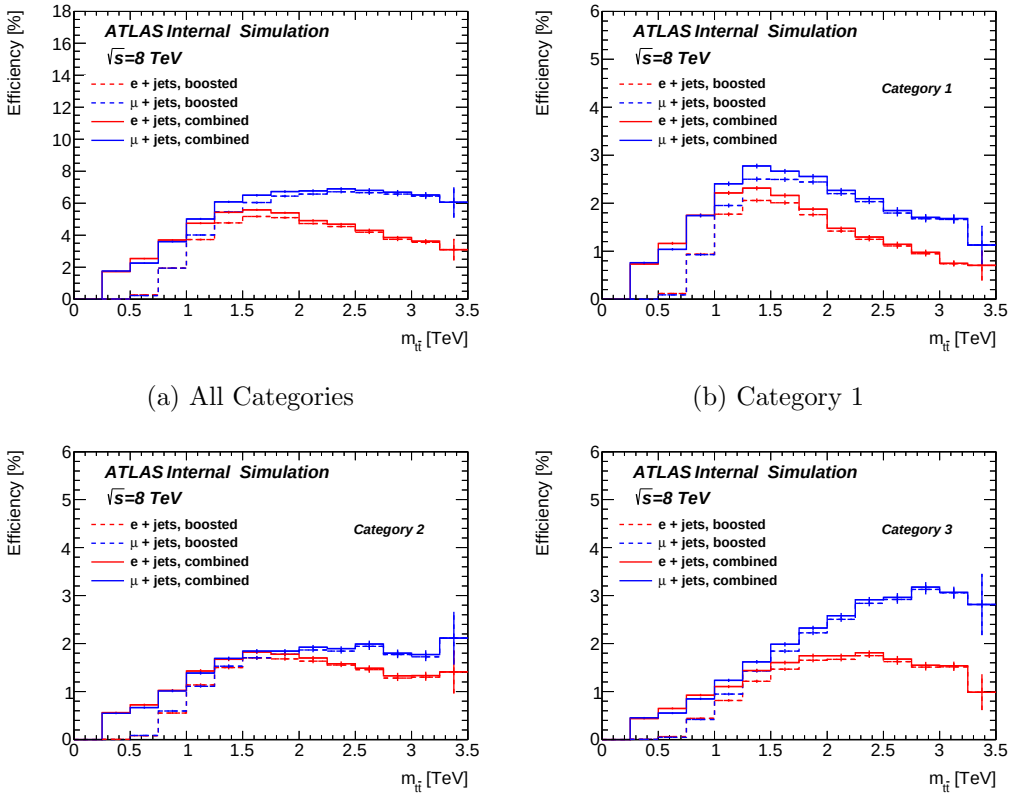

(a) All Categories

(b) Category 1

(c) Category 2

(d) Category 3

Figure 8.8: Selection efficiency for a Z' boson as a function of the true $m_{t\bar{t}}$ of each event.

The selection efficiency of the boosted channel alone and of the combination between the boosted and resolved channels are shown in Figure 8.8. The resolved channel shows a decent selection efficiency for $t\bar{t}$ events at low m_{tt} while the boosted channel primarily selects events above 750 GeV to 1 TeV. Although the electron and muon channels show similar efficiencies at low and moderate masses, the efficiency of the electron channel begins to suffer at high mass due the electron-jet overlap removal procedure. Additionally, efficiency to tag the b-jet resulting from a hadronic top decay suffers at high mass due to the crowded environment, impacting categories 1 and 2. Likewise, the presence of an electron close to a b-jet can negatively impact the b-tagging efficiency. This can be seen in the divergence in the selection efficiency between the electron and muon channels in category 3 at high m_{tt}.

Chapter 9

Background Estimation

The previous chapter described the procedure for selecting and reconstructing collisions resulting in the production of a heavy particle decaying to a pair of top quarks. However, the Standard Model also predicts a number of background processes which may produce significant numbers of events satisfying this selection. These backgrounds are modeled via a combination of Monte Carlo simulation, described in Chapter 7, and data driven methods.

The largest background contribution is SM $t\bar{t}$ events, which are predominately produced via the strong force. In simulation, this background is generated by the POWHEG ME generator while PYTHIA models the parton showering, hadronization and underlying event. Only events in which at least one top quark decays leptonically are simulated, as fully hadronic events are included in the multijet estimate described in Section 9.2. With an effective cross section of 129 pb, $t\bar{t}$ pairs are produced in abundant quantities at the LHC.

This background is considered to be 'irreducible,' meaning that it is difficult to substantially reduce its contribution through improved kinematic cuts as it shares similar features with the signal processes being studied. However, the SM $t\bar{t}$ background shows a steeply falling distribution in m_{tt}, from which a signal contribution can be distinguished as a local excess of events (for a narrow signal) or from it's differing shape (for a wider signal).

SM W+jets and Z+jets production, the second and fifth largest backgrounds respectively, are both simulated in ALPGEN, with PYTHIA again modeling the parton showering, hadronization and underlying event. Separate samples are generated for each multiplicity of light and heavy flavor jets produced in the hard process of the Monte Carlo generator. The

bosons in these events are decayed leptonically. In the boosted channel, specially prepared W+jets Monte Carlo samples requiring a truth level anti-k_t R=1.0 jet with $p_T > 250$ GeV are used to increase the available statistics of such events.

In the case of the W+jets background, scale factors are derived from data and applied to correct both the normalization of the W+jets background and the fraction of events containing a jet originating from a heavy flavor quark, as described in section 9.1. As the contribution from the Z+jets background is small, no such normalization is applied to that sample.

The third largest background, electroweak single top quark production, is produced in three channels. The s-channel (in which a W boson decays to a bottom and top quark) and the Wt-channel (in which a W boson is produced in conjunction with a top quark) are both modeled using POWHEG+PYTHIA. The t-channel, involving the exchange of a flavor changing W boson between two quarks, is generated using ACERMC+PYTHIA. In the s- and t-channels, only leptonically decaying top quarks are considered.

The diboson (WW, WZ and ZZ) and $t\bar{t}$+Boson ($t\bar{t}V$) backgrounds also make modest contributions. Dibosons are modeled using HERWIG while $t\bar{t}V$ is modeled using MADGRAPH+PYTHIA.

All of the above backgrounds contain leptons created in the decay of a vector boson. However, an additional class of backgrounds can result from non-prompt or fake leptons. Such events arise primarily from 'QCD' multijet production. While the multijet cross section is enormous, the difficulty in faking a high quality lepton implies that this background contributes only a moderate number of events. Due to the very large rejection rate, this background cannot be reliably simulated. Instead, the multijet background contribution is estimated directly from data, as described in Section 9.2.

9.1 W+Jets Background Estimation

As mentioned above, the shape and acceptance of the W+jets background is modeled using ALPGEN with PYTHIA. However, the overall normalization and the fraction of this background containing one or more heavy flavor quarks are improved using data. The

appropriate scale factors are derivedby exploiting the charge asymmetry in W+jets events as well as the number of b-jets in lower multiplicity W+jets events.

9.1.1 W+jets Normalization

While other large backgrounds in this study are symmetric in the charge of the lepton, W^+ bosons are expected to be more common at the LHC than their negatively charged counterparts due to the underlying asymmetry of the quark and anti-quark compositions of the colliding protons. The ratio of W^+ to W^- cross sections can be calculated from the various distributions of the quarks and antiquarks in a proton (the so called parton distribution functions, or PDFs) [55]. Thus, the overall normalization of W+jets events can be determined by measuring the fraction of positively or negatively charged W bosons produced.

The normalization of the W+jets background is estimated from a data sample passing a similar selection to the one used in this analysis. In the resolved channel, all cuts described in Chapter 8 are applied except that no b-tagging requirement is imposed. In the boosted channel, b-tagging, $\Delta\Phi$(large-R jet,lepton) > 2.3, jet mass, and Split$_{12}$ cuts are not applied in order to increase the event yield. Small charge asymmetric backgrounds (single-top and diboson) are estimated from Monte Carlo simulation and subtracted from the data. An estimate for the number of W+jets events ($N_{W^+} + N_{W^-}$) is given by the following formula:

$$N_{W^+} + N_{W^-} = \left(\frac{r_{MC}+1}{r_{MC}-1}\right)(D_+ - D_-). \tag{9.1}$$

D_+ and D_- are the number of observed events in data with a positive or negative lepton respectively. r_{MC} is the ratio of W^+ to W^- events predicted by the Monte Carlo after applying the event selection described above. The resulting normalization scale factors are shown in Table 9.1, along with their statistical uncertainties.

9.1.2 W+jets Flavor Composition

The heavy flavor composition of the W+jets background can be determined from the fraction of W+jets events which contain at least one b-tagged jet in data. All cuts in the resolved selection are applied to data except for b-tagging, jet selection, and

Lepton Channel	Normalization Factor (Resolved)	Normalization Factor (Boosted)
Electron	1.08 ± 0.01	0.83 ± 0.06
Muon	0.94 ± 0.01	0.78 ± 0.05

Table 9.1: W+jets normalization scale factors derived via the charge asymmetry method.

the χ^2. All backgrounds except W+jets are subtracted from the data, including the multijet background estimated in Section 9.2. The events are then binned according to jet multiplicity.

The W+jets background is assumed to be composed of four flavor types representing the possible presence of heavy flavor quarks: light flavor, c, cc, and bb. The fractions of W+jets events of each type in the i$^{\text{th}}$ jet multiplicity bin are denoted $F_{\text{xx},i}$ while the probability for an event to be b-tagged is given by $P_{\text{xx},i}$, where 'xx'='light','c','cc', or 'bb.' Finally, the ratio $k_{\text{cctobb}} = F_{\text{cc},i}/F_{\text{bb},i}$ is taken from Monte Carlo. This gives the following relationship between the number of W+jets events before and after applying b-tagging, considered separately for each charge:

$$N^{W\pm,tag} = N^{W\pm,pretag}(F^{\pm}_{\text{light},i}P_{\text{light},i} + F^{\pm}_{\text{c},i}P_{\text{c},i} + F^{\pm}_{\text{cc},i}P_{\text{cc},i} + k_{\text{cctobb}}F^{\pm}_{\text{cc},i}P_{\text{bb},i}), \tag{9.2}$$

where the heavy flavor fractions sum to unity when combined between the two charges:

$$F_{\text{light},i} + F_{\text{c},i} + F_{\text{cc},i} + k_{\text{cctobb}}F_{\text{cc},i} = 1. \tag{9.3}$$

The number of pretagged W+jets events in Monte Carlo is normalized using the charge asymmetry method described in Section 9.1.1. Setting the number of predicted W+jets events predicted by the Monte Carlo equal to the number observed in data allows the fractions $F_{\text{xx},i}$ to be determined. The overall normalization is then updated to reflect the new heavy flavor fractions, and the procedure is repeated until the results approach stable values. In the two jet bin, the heavy flavor scale factors are determined as the ratio of the heavy flavor fractions predicted in Monte Carlo to those observed in data:

$$K_{\text{xx},2} = \frac{F^{\text{data}}_{\text{light},2}}{F^{\text{MC}}_{\text{light},2}}. \tag{9.4}$$

Lepton Channel	K_{light}	K_c	K_{bb} (K_{cc})
Electron	0.80	1.17	1.36
Muon	0.84	0.83	1.50

Table 9.2: W+jets heavy flavor scale factors.

In order to account for the varying flavor fractions in each jet bin and avoid changing the overall normalization, an additional normalization factor must be applied to the scale factors for other jet multiplicity bins:

$$K_{\text{xx},i} = \frac{K_{\text{xx},2}}{A}, \tag{9.5}$$

where

$$A = K_{\text{light},i} F^{MC}_{\text{light},i} + K_{\text{c},i} F^{MC}_{\text{c},i} + K_{\text{cc},i} F^{MC}_{\text{cc},i} + k_{\text{cctobb}} K_{\text{cc},i} F_{\text{cc},i}. \tag{9.6}$$

These scale factors are then validated by confirming that they correctly predict the tagged and pretagged event counts derived via a similar procedure in the higher jet multiplicity bins. The resulting heavy flavor scale factors for the four jet bin are given in Table 9.2. The distribution of jet multiplicities in the resolved selection before and after applying the heavy flavor scale factors and the normalization factor derived in Section 9.1.1 are shown in Figures 9.1 and 9.2, with and without the b-tagging requirement.

9.2 MultiJet Background Estimate

The event selection described in Chapter 8 greatly suppresses backgrounds observed by the ATLAS detector that do not include the production of a prompt lepton (i.e. a lepton produced from the decay of a W or Z boson in the hard process). However, several mechanisms exist for faking prompt leptons. Prompt muons and electrons may both be faked by a non-prompt lepton produced in the decay of a heavy flavor hadron. Alternatively, electrons may also be faked by a high p_T π^0 overlapping with the track of another charged particle, usually inside of a jet, or by the conversion of a photon to an e^+/e^- pair. While

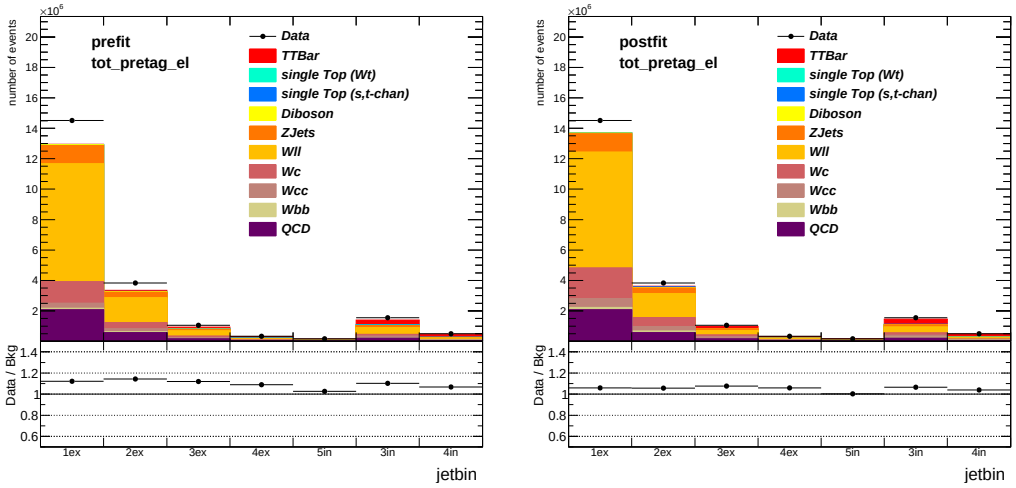

(a) Pre-tag, e channel without scale factors (b) Pre-tag, e channel with scale factors

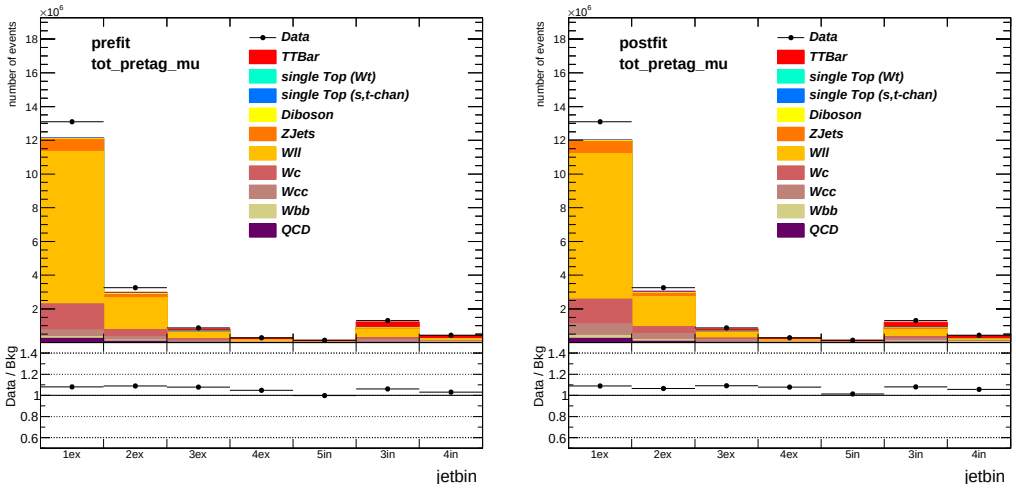

(c) Pre-tag, mu channel without scale factors (d) Pre-tag, mu channel with scale factors

Figure 9.1: Number of events in each jet multiplicity bin in data and background estimates. Shown before (left) and after (right) applying heavy flavor and normalization scale factors to the W+jets background. Exclusive (ex) jet bins include all events containing a particular number of jets, while inclusive (in) jet bins include events containing a minimum number of events. No b-tagging requirement has been applied.

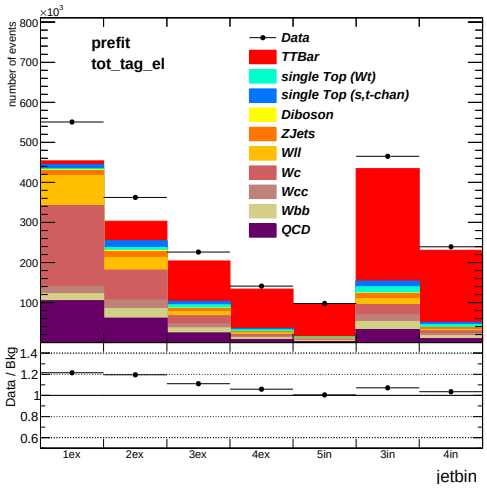

(a) b-tagged, e channel without scale factors

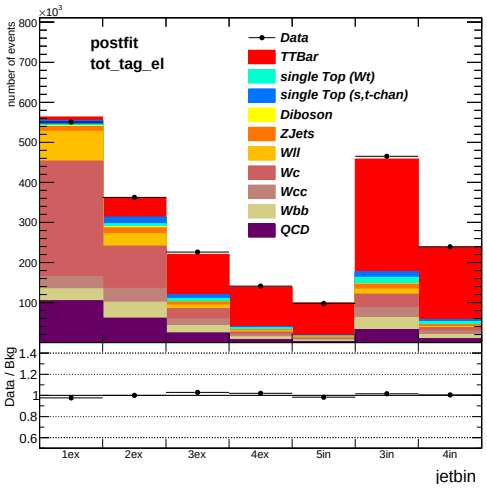

(b) b-tagged, e channel with scale factors

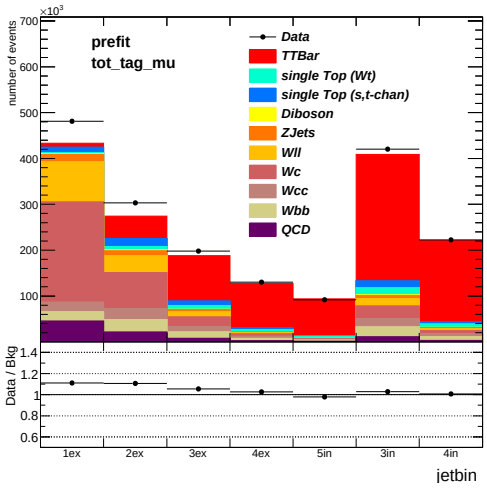

(c) b-tagged, mu channel without scale factors

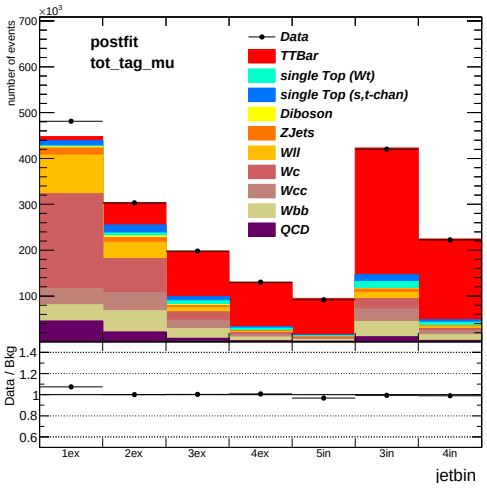

(d) b-tagged, mu channel with scale factors

Figure 9.2: Number of events in each jet multiplicity bin in data and background estimates. Shown before (left) and after (right) applying heavy flavor and normalization scale factors to the W+jets background. At least one b-tagged jet is required.

such leptons do not have a high probability of surviving quality cuts, especially isolation requirements, the very large cross section of the multijet background implies that this contribution must be considered carefully.

The very high rejection rate of of non-prompt or fake lepton sources implies that large systematic uncertainties due to detector effects, object reconstruction, isolation effects, the parton shower modeling and other factors will lead to unreliable simulation of such events. Thus, a data driven approach is used to estimate the background contributions from non-prompt sources by examining events containing lower quality ('loose') leptons. A control region in which contributions from non-prompt background sources is expected to be enhanced is also examined in order to understand the likelihood for such backgrounds to fake a high quality isolated lepton. The estimation of electron efficiencies and fake rates, as well as the distribution of events in signal and control regions is presented in Section 9.2.1. Section 9.2.2 describes the Matrix Method procedure which is used to disentangle the prompt and non-prompt lepton sources in the signal and control regions.

9.2.1 Lepton Efficiency and Fake Rates

The lepton identification efficiencies and fake rates are evaluated by considering the distributions of leptons passing two different quality levels. 'Tight' leptons are those passing all identification and selection criteria described in Chapters 5 and 8, including isolation requirements and the Tight++ quality criterion for electrons. Such tight leptons offer a very high rejection rate of non-prompt leptons. In the 'Loose' electron selection, the Tight++ quality criteria are replaced by Medium++.[1] Additionally, isolation requirements are not applied, but a veto against converted photons is added in the electron channel. Loose muons are not required to pass isolation requirements.

Control regions with enhanced multijet backgrounds are also defined in the resolved and boosted selections (denoted $CR0_{\text{resolved}}$ and $CR0_{\text{boosted}}$ respectively). The event selections in the control regions are similar to those in the signal regions with several differences:

[1] Compared to Tight++, Medium++ utilizes looser requirements on the quality and number of hits in the ID, and the alignment between the ID track and the calorimeter deposit. The Medium++ quality selection also removes certain isolation requirements from the Tight++ selection.

- Cuts on $E_{\mathrm{T}}^{\mathrm{miss}}$and M_TW are inverted:
  - $E_{\mathrm{T}}^{\mathrm{miss}}< 20$ GeV.
  - $E_{\mathrm{T}}^{\mathrm{miss}}+M_TW < 60$ GeV.
- The distance of closest approach of the extrapolated particle track to the primary vertex ($d0$) is required to be larger than that expected for a prompt lepton. In particular, $|d0/\sigma_{d0}| > 2.5$ (3.2) is required in the electron (muon) channel.
- The χ^2 cut is inverted in the resolved channel: $log_{10}(\chi^2) > 0.9$.
- An alternative large-R jet selection is applied in the boosted channel:
  - $p_T > 150$ GeV (rather than 300 GeV).
  - Cut on $\sqrt{d_{12}}$ is removed.
  - Mass cut is inverted: $m \leq 100$ GeV.

The control regions are dominated by multijet events. Thus, the probability for a non-prompt loose lepton to also pass the tight criteria (i.e. the fake rate f) may be measured directly from data. These lepton identification fake rates are measured as a function of the p_T of the loose lepton and that of the nearest jet. In addition, the fake rates are determined separately in the case that the distance to the closest jet, $\Delta R(lepton, jet)$, is less than or greater than 0.4.

The efficiency, ϵ, for a prompt electron to pass the tight selection given that it passes the loose selection is measured from Monte Carlo simulation in the signal regions, and is described as a function of the lepton p_T and the distance to the nearest jet, $\Delta R(lepton, jet)$. These efficiencies are shown in Figures 9.3 and 9.4 for the resolved and boosted channels respectively, while the fake rates are shown in Figures 9.5 and 9.6.

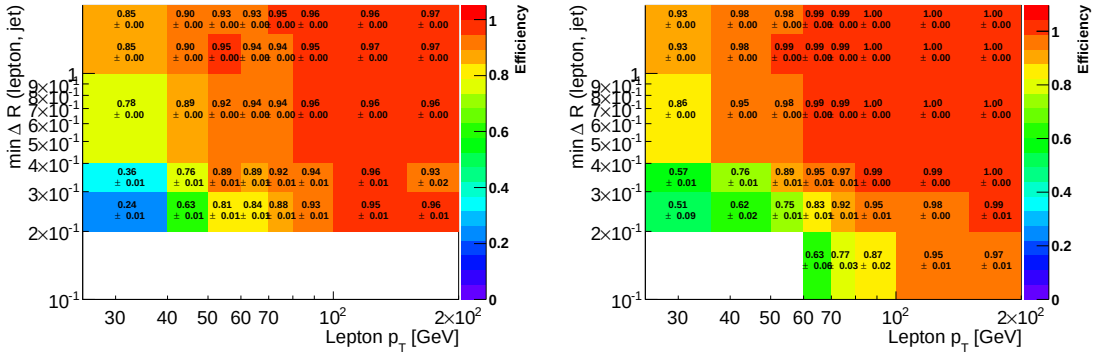

(a) Electron Efficiency (b) Muon Efficiency

Figure 9.3: Efficiencies for loose electrons and muons to be identified as tight in the resolved selection.

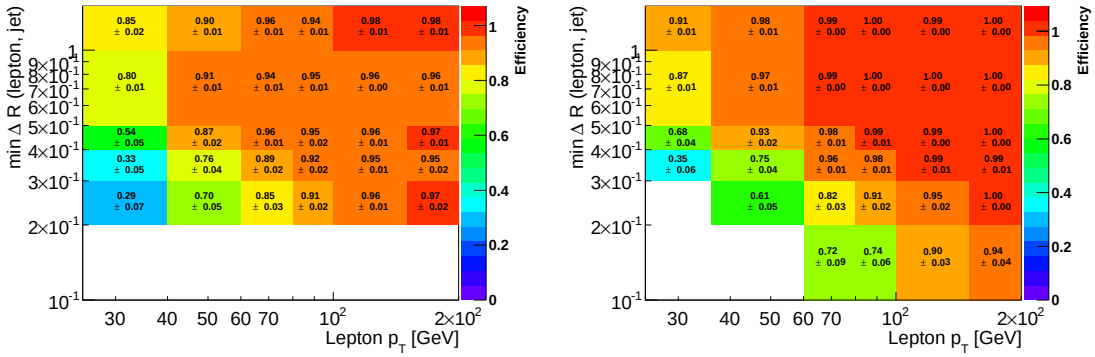

(a) Electron Efficiency (b) Muon Efficiency

Figure 9.4: Efficiencies for loose electrons and muons to be identified as tight in the boosted selection.

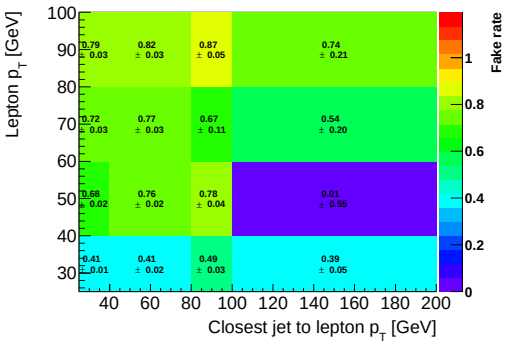

(a) Electron Fake Rate, $\Delta R(el, jets) > 0.4$, $d0 < 3$ sigma

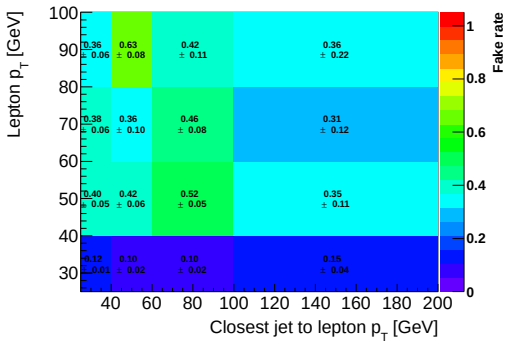

(b) Electron Fake Rate,$\Delta R(el, jets) < 0.4$, $d0 < 3$ sigma

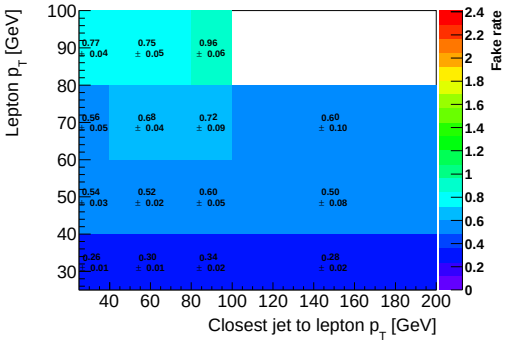

(c) Electron Fake Rate, $\Delta R(el, jets) > 0.4$, $d0 > 3$ sigma

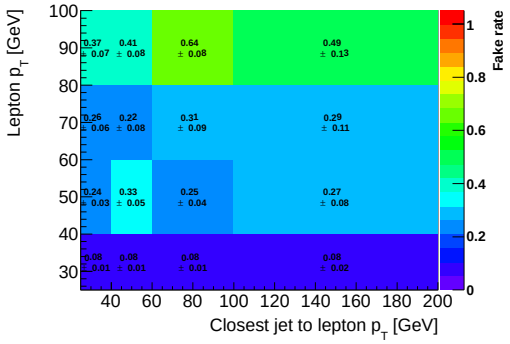

(d) Electron Fake Rate,$\Delta R(el, jets) < 0.4$, $d0 > 3$ sigma

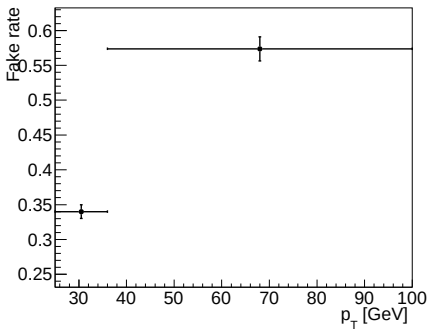

(e) Muon Fake Rate, $\Delta R(\mu, jets) > 0.4$

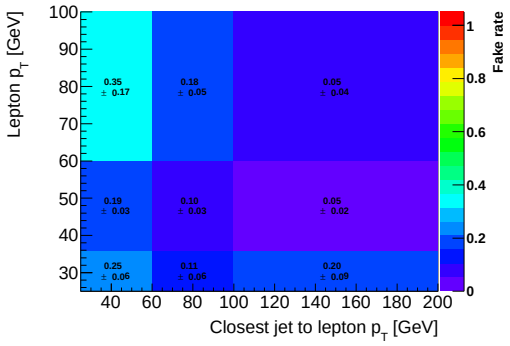

(f) Muon Fake Rate, $\Delta R(\mu, jets) < 0.4$

Figure 9.5: Fake rates for non-prompt loose electrons and muons to be identified as tight in the resolved selection. A one-dimensional parameterization of the fake rate for muons with $\Delta R(\mu, jets) > 0.4$ is used due to inadequate statistics.

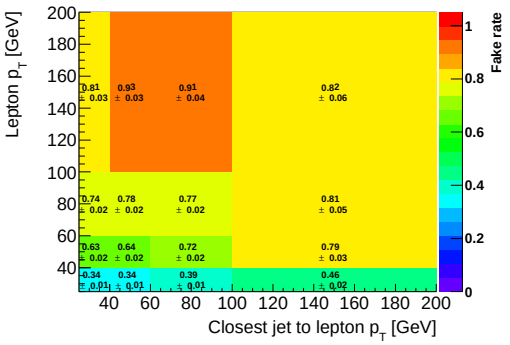

(a) Electron Fake Rate, $\Delta R(el, jets) > 0.4$, $d0 < 3$ sigma

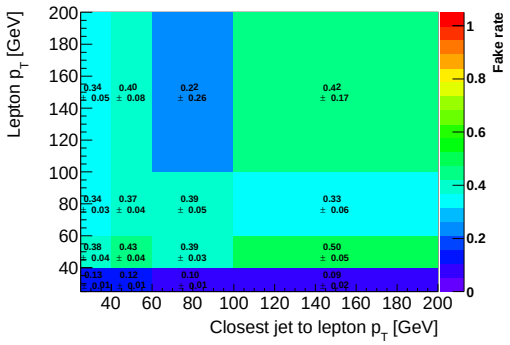

(b) Electron Fake Rate, $\Delta R(\mu, jets) < 0.4$, $d0 < 3$ sigma

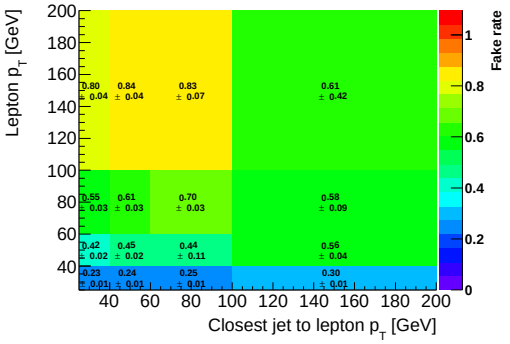

(c) Electron Fake Rate, $\Delta R(el, jets) > 0.4$, $d0 > 3$ sigma

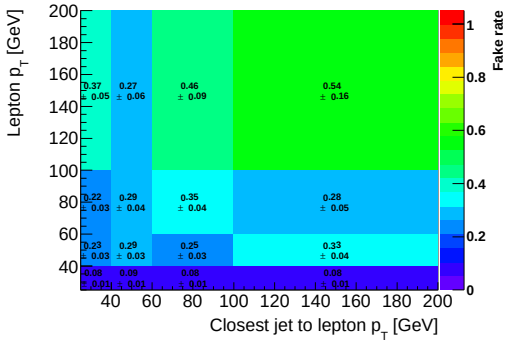

(d) Electron Fake Rate, $\Delta R(\mu, jets) < 0.4$, $d0 > 3$ sigma

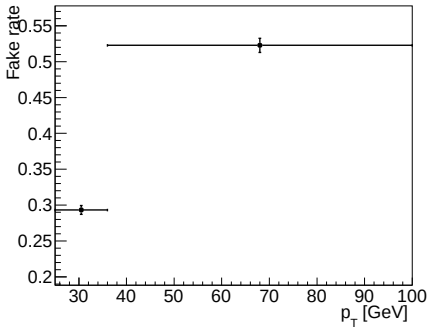

(e) Muon Fake Rate, $\Delta R(\mu, jets) > 0.4$

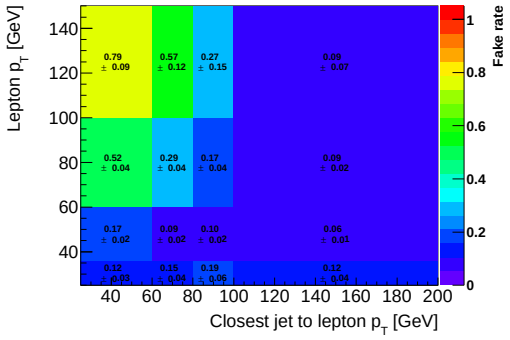

(f) Muon Fake Rate, $\Delta R(\mu, jets) < 0.4$

Figure 9.6: Fake rates for non-prompt loose electrons and muons to be identified as tight in the boosted selection. A one-dimensional parameterization of the fake rate for muons with $\Delta R(\mu, jets) > 0.4$ is used due to inadequate statistics.

9.2.2 Matrix Method

The lepton efficiencies (ϵ) and fake rates (f) measured in the previous section are used to estimate the multijet background in the signal region by use of the Matrix Method. The total number of events containing a tight (loose) lepton, N_T (N_L) is the sum of contributions from prompt and fake (i.e. non-prompt) leptons:

$$\begin{pmatrix} N_T \\ N_L \end{pmatrix} = \begin{pmatrix} \epsilon & f \\ 1 & 1 \end{pmatrix} \begin{pmatrix} N_{\text{real}} \\ N_{\text{fake}} \end{pmatrix}. \tag{9.7}$$

Inverting the matrix gives an estimate for the number of fake tight leptons which contaminate the signal region:

$$N_{T,\text{fake}} = f \times N_{\text{fake}} = \frac{f}{\epsilon - f}(N_L \times \epsilon - N_T) \tag{9.8}$$

$$= \frac{(\epsilon - 1)f}{\epsilon - f} N_T + \frac{\epsilon \times f}{\epsilon - f} N_A, \tag{9.9}$$

Where N_A is the number of events which contain a loose but not tight ('anti-tight') lepton and the lepton efficiencies and fake rates are parameterized according to the event kinematics as described in the previous section. The multijet contribution to the signal region is obtained by taking the loose sample, and assigning to each event a weight, as given in Equation 9.9, depending on whether it is tight or 'anti-tight.'

Modeling of the multijet background via the Matrix Method approach accurately describes the reconstructed $t\bar{t}$ invariant mass in the control regions ($CR0$). Figure 9.7 shows the $m_{t\bar{t}}$ distributions produced by this approach after requiring the presence of a tight lepton in each of the four control regions.

9.3 Comparison of Data and Expected Backgrounds

Table 9.3 shows the number of events observed in data and the expected number of events from each background source in both the boosted and resolved channels. In total, 8164 data events are assigned to the boosted channel and 222504 to the resolved channel.

The invariant mass spectra of the reconstructed $t\bar{t}$ pair are shown in Figure 9.8 for the resolved channel and Figure 9.9 for the boosted channel. The overall agreement between data and expectations is decent.

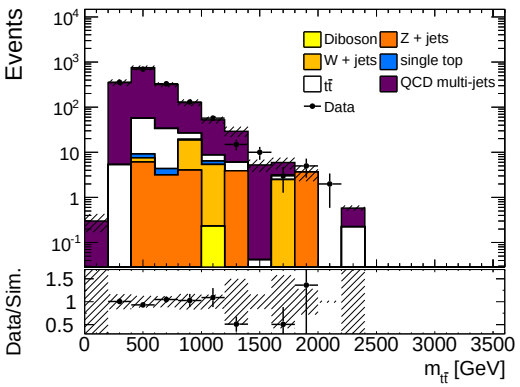

(a) Resolved Electron Channel

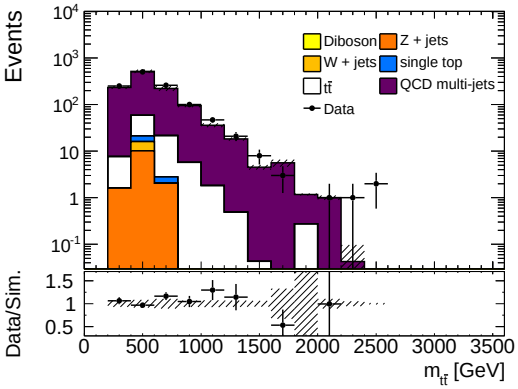

(b) Resolved Muon Channel

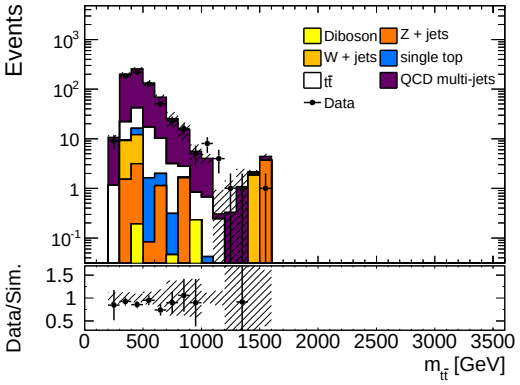

(c) Boosted Electron Channel

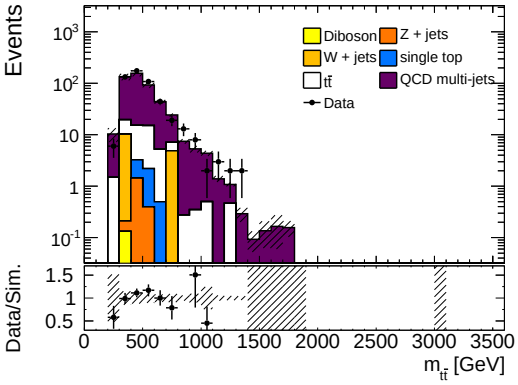

(d) Boosted Muon Channel

Figure 9.7: $m_{t\bar{t}}$ distributions of events containing tight leptons in the $CR0$ control region.

Resolved selection			
Type	e+jets	μ+jets	Sum
ttbar	93000 ± 10000	92000 ± 10000	186000 ± 20000
Single top	3800 ± 400	3800 ± 500	7600 ± 800
ttV	264 ± 15	267 ± 13	531 ± 26
QCD e	4030 ± 90	0.0 ± 0.0	4030 ± 90
QCD mu	0.0 ± 0.0	1243 ± 29	1243 ± 29
W+jets	7700 ± 1400	7100 ± 1200	14900 ± 2600
Z+jets	1400 ± 330	650 ± 130	2050 ± 400
Di-bosons	320 ± 50	310 ± 50	620 ± 100
Total	111000 ± 11000	106000 ± 11000	217000 ± 22000
Data	113736	108768	222504
Boosted selection			
Type	e+jets	μ+jets	Sum
$t\bar{t}$	4200 ± 700	4100 ± 700	8300 ± 1500
Single top	136 ± 21	154 ± 22	290 ± 39
ttV	36 ± 4	38 ± 4	75 ± 7
QCD e	88 ± 20	0.0 ± 0.0	88 ± 20
QCD mu	0.0 ± 0.0	11 ± 5	11 ± 5
W+jets	270 ± 40	290 ± 40	560 ± 70
Z+jets	30 ± 8	17 ± 5	47 ± 10
Di-bosons	21 ± 5	20 ± 4	41 ± 7
Total	4700 ± 800	4700 ± 800	9400 ± 1500
Data	4117	4047	8164

Table 9.3: Data and expected background yields after the full resolved or boosted selection. The associated systematic uncertainties on the yields are also shown.

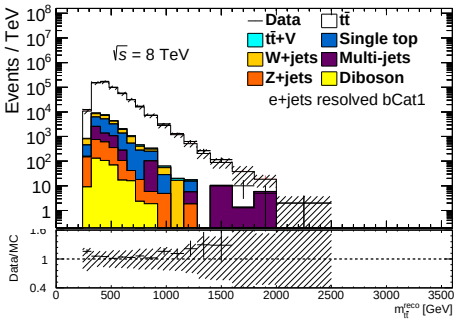

(a) Electron channel, resolved selection, category 1

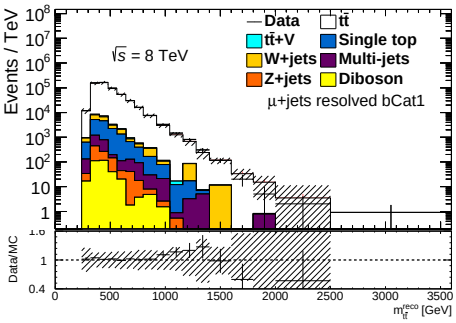

(b) Muon channel, resolved selection, category 1

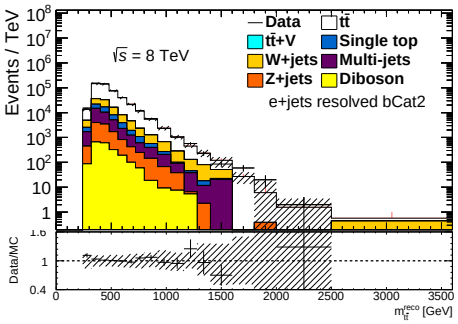

(c) Electron channel, resolved selection, category 2

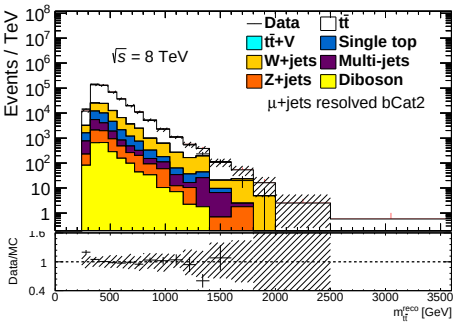

(d) Muon channel, resolved selection, category 2

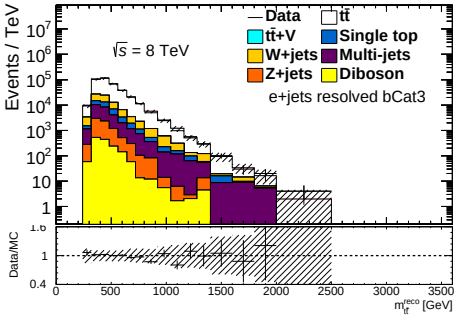

(e) Electron channel, resolved selection, category 3

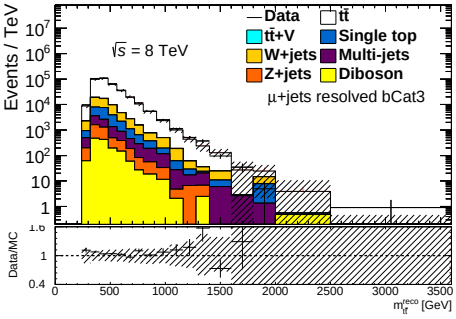

(f) Muon channel, resolved selection, category 3

Figure 9.8: $m_{t\bar{t}}$ distributions of events in the resolved selection. Categories 1, 2 and 3 contain events in which b-tagged jets are associated to both the hadronically and leptonically decaying top quarks, only the hadronically decaying top quark, or only to the leptonically decaying top quark respectively. Systematic and Monte Carlo statistical uncertainties are shown on the background estimates.

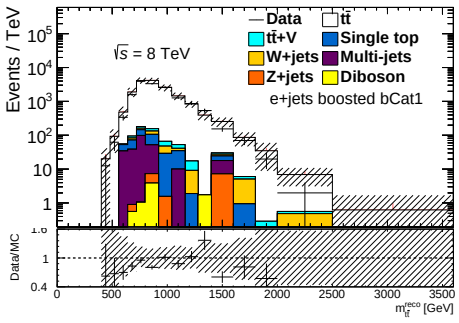

(a) Electron channel, boosted selection, category 1

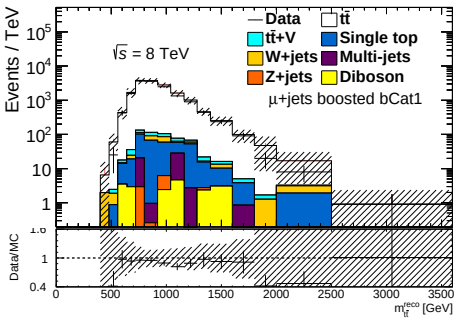

(b) Muon channel, boosted selection, category 1

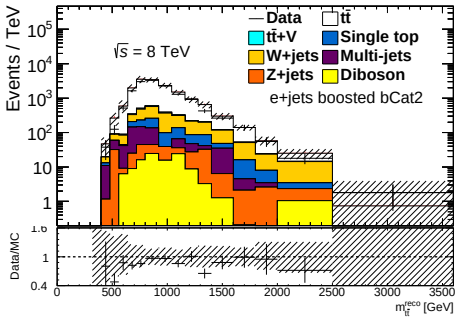

(c) Electron channel, boosted selection, category 2

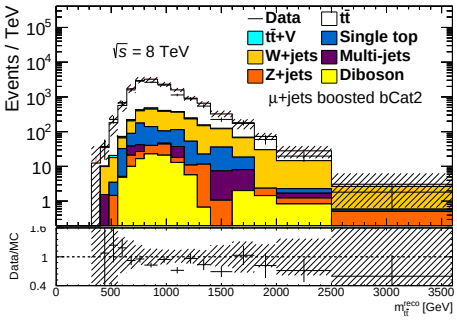

(d) Muon channel, boosted selection, category 2

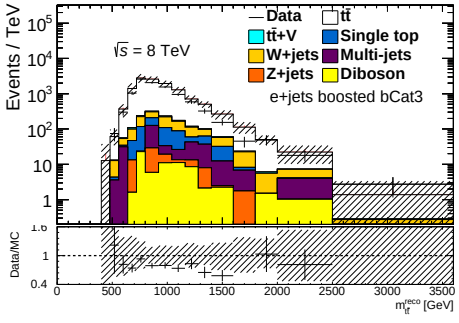

(e) Electron channel, boosted selection, category 3

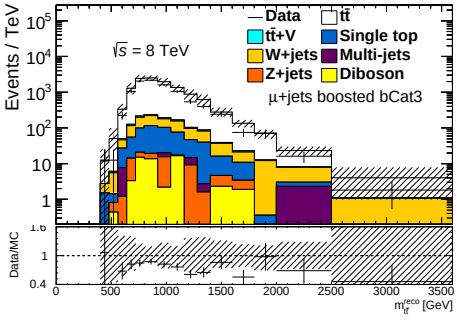

(f) Muon channel, boosted selection, category 3

Figure 9.9: $m_{t\bar{t}}$ distributions of events in the boosted selection. Categories 1, 2 and 3 contain events in which b-tagged jets are associated to both the hadronically and leptonically decaying top quarks, only the hadronically decaying top quark, or only to the leptonically decaying top quark respectively. Systematic and Monte Carlo statistical uncertainties are shown on the background predictions.

Chapter 10

Signal Characteristics

Chapter 2 motivated the search for heavy particles decaying to $t\bar{t}$ pairs and presented several benchmark models. This chapter describes the characteristics of events arising from these models in the ATLAS detector.

The mass distributions of resonances are approximately described by the relativistic Breit-Wigner function. However, both theoretical and experimental effects can modify the shape of this distribution as observed at ATLAS.

This analysis considers potential signals over a very wide range of masses, from 400 GeV to 3 TeV. Each individual quark or gluon carries only a fraction of a proton's energy, with a distribution described by parton distribution functions (PDFs). Collisions between partons with sufficient energy to create the highest mass resonances studied in 8 TeV proton-proton collisions are very rare. Thus, very heavy particles are likely to be produced 'off mass shell,' with a mass significantly below the resonance mass. In addition, highly boosted top quarks tend to radiate, resulting in an invariant mass of the observed $t\bar{t}$ pair which is below that of the parent particle. Figures 10.1 and 10.2 show the theoretical mass distributions of heavy resonances produced by proton-proton collisions at 8 TeV as well as the invariant mass of the $t\bar{t}$ pair produced by the decay.

In addition to theoretical factors, detector level effects, event selection inefficiencies, the event reconstruction procedure, pileup, and other experimental effects will modify the observable shape of a potential signal. Figure 10.3 shows the shape of the reconstructed $t\bar{t}$

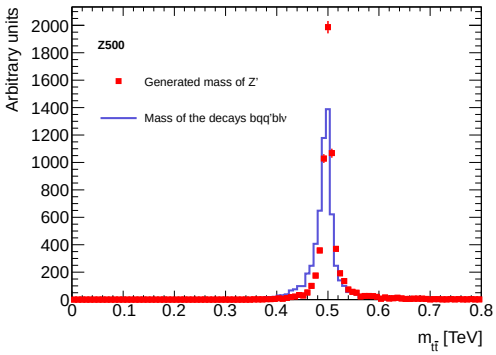

(a) $m_{Z'} = 0.5$TeV

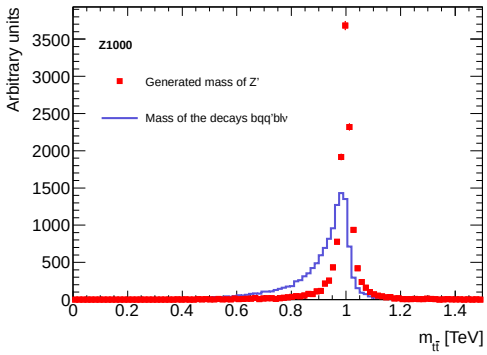

(b) $m_{Z'} = 1.0$TeV

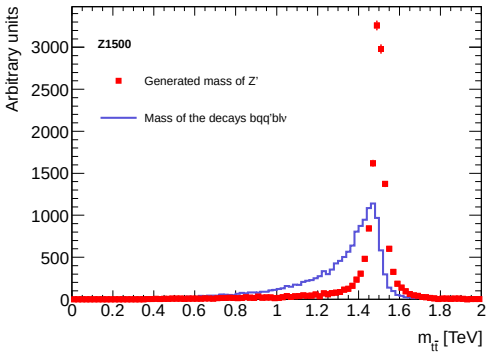

(c) $m_{Z'} = 1.5$TeV

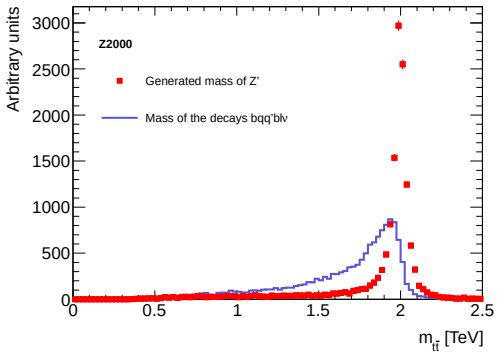

(d) $m_{Z'} = 2.0$TeV

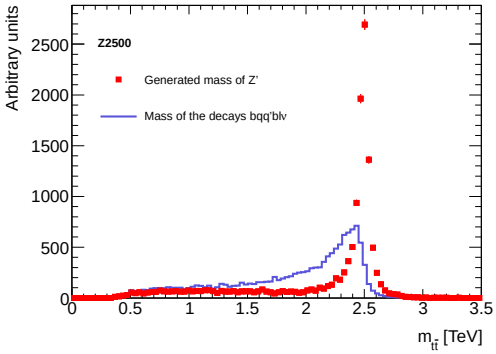

(e) $m_{Z'} = 2.5$TeV

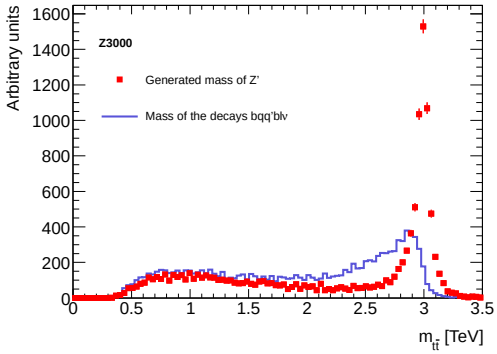

(f) $m_{Z'} = 3.0$TeV

Figure 10.1: Mass distributions of generated Z' resonances (red) and the invariant masses of the associated top quarks. The most massive signals prefer to be produced off the mass shell due to the steeply falling PDFs. The difference between the mass of the Z' boson and that of the produced top quark pair is due to final state radiation emitted by those top quark.

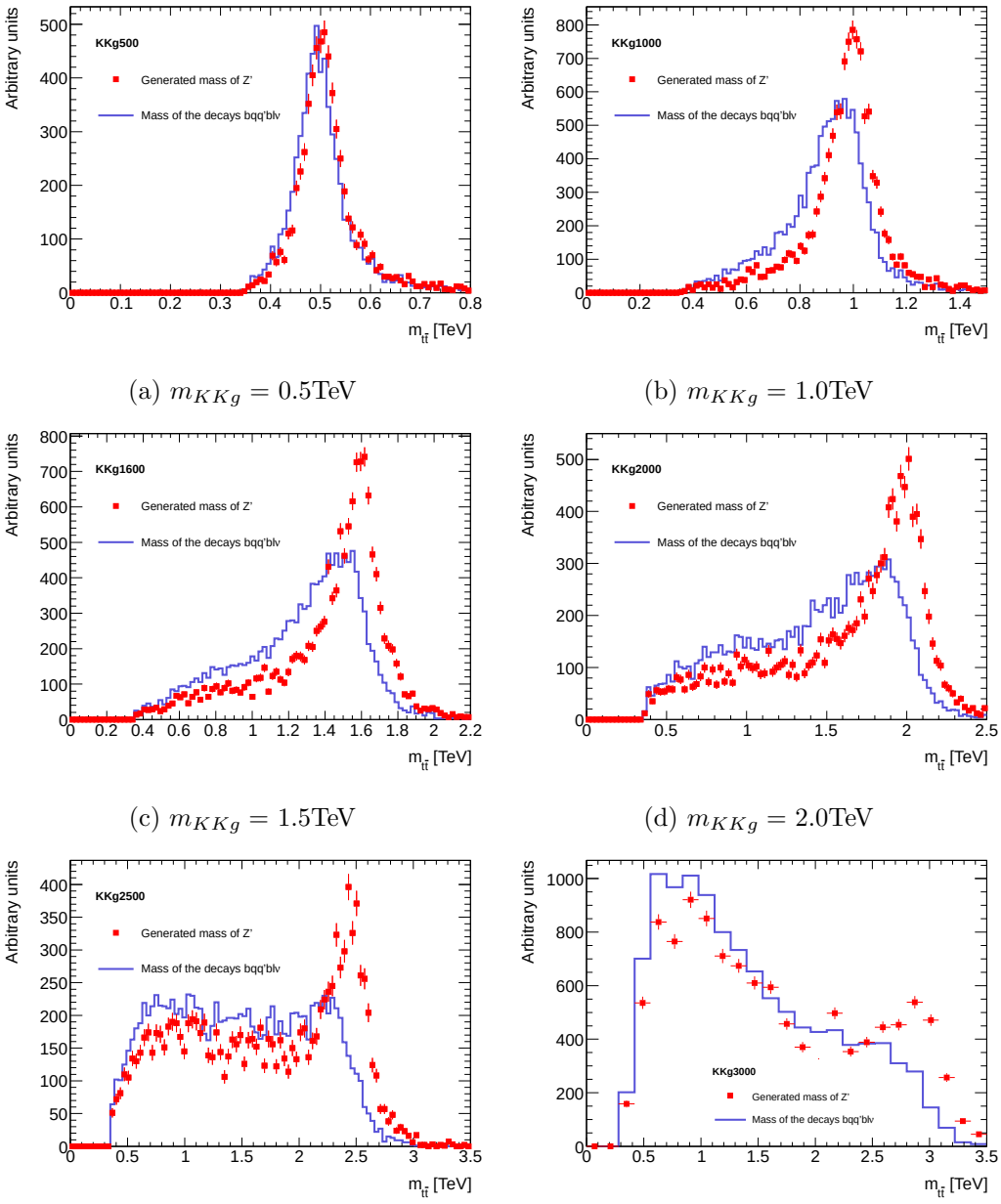

(a) $m_{KKg} = 0.5$TeV

(b) $m_{KKg} = 1.0$TeV

(c) $m_{KKg} = 1.5$TeV

(d) $m_{KKg} = 2.0$TeV

(e) $m_{KKg} = 2.5$TeV

(f) $m_{KKg} = 3.0$TeV

Figure 10.2: Mass distributions of generated KKg resonances (red) and the invariant masses of the associated top quarks. The most massive signals prefer to be produced off the mass shell due to the steeply falling PDFs. The difference between the mass of the KKg and that of the produced top quark pair is due to final state radiation emitted by those top quark.

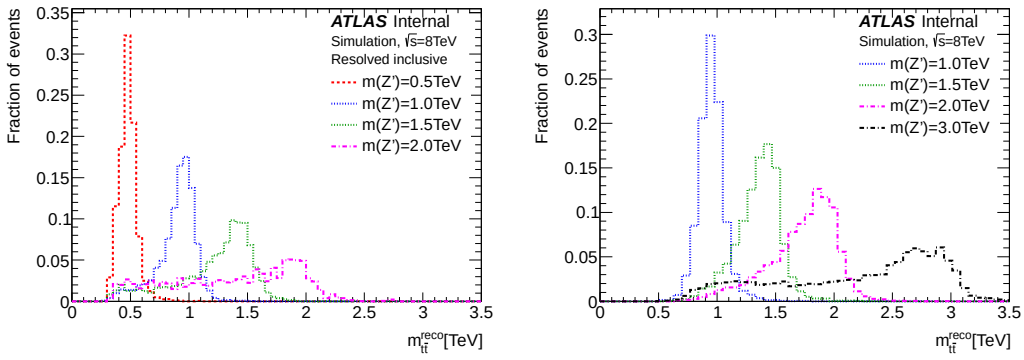

(a) Resolved Channel (b) Boosted Channel

Figure 10.3: Shape of the reconstructed $t\bar{t}$ invariant mass expected from a Z' signal for several resonance masses.

invariant mass for Z' signals at several different masses. Likewise, Figure 10.4 shows how the shape of a KKg sample varies with the resonance width.

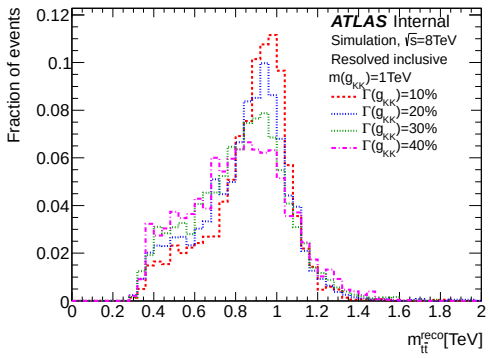

(a) Resolved Channel, $m_{t\bar{t}} = 1$ TeV

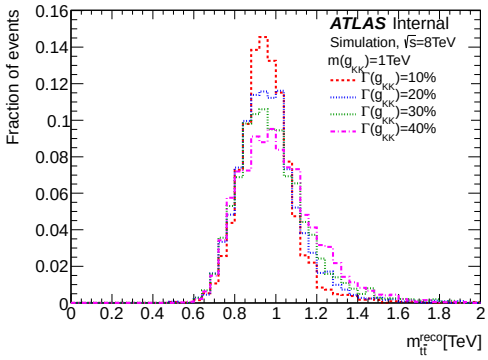

(b) Boosted Channel, $m_{t\bar{t}} = 1$ TeV

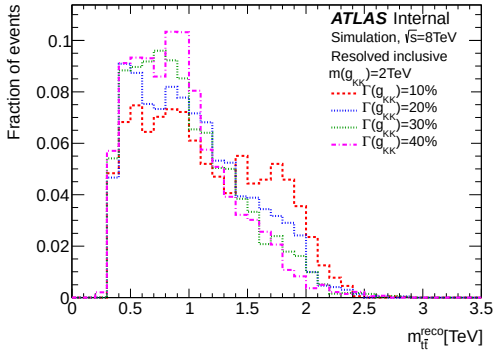

(c) Resolved Channel, $m_{t\bar{t}} = 2$ TeV

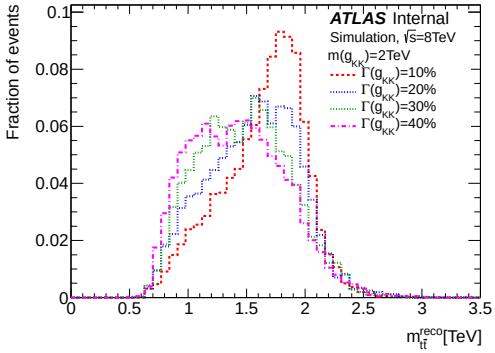

(d) Boosted Channel, $m_{t\bar{t}} = 2$ TeV

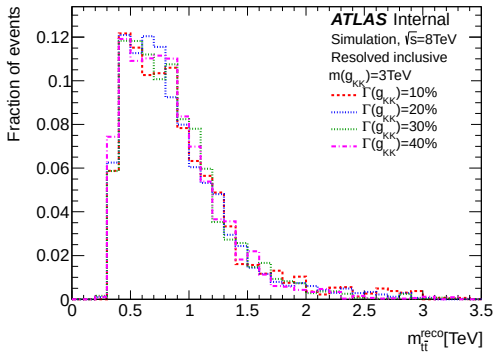

(e) Resolved Channel, $m_{t\bar{t}} = 3$ TeV

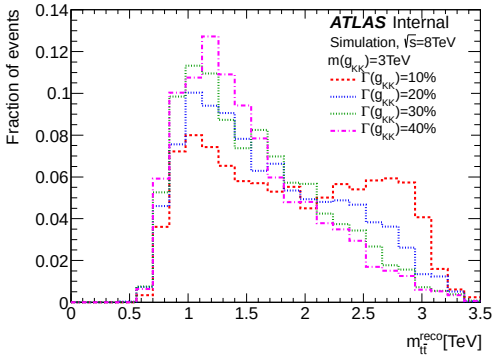

(f) Boosted Channel, $m_{t\bar{t}} = 3$ TeV

Figure 10.4: Shape of the reconstructed $t\bar{t}$ invariant mass expected from a KKg signal for several resonance masses and widths.

Chapter 11

Systematic Uncertainties and Corrections

The high level of experimental complexity in this analysis implies that the inclusion of systematic uncertainties is critical for the proper interpretation of the results. For this purpose, a number of sources of systematic uncertainties have been identified. For each systematic, the potential impact on both the expected yield and shape of each background and signal has been studied.

11.1 General Uncertainties

An uncertainty of 2.8% is applied to the overall normalization of all non-data driven backgrounds to represent the uncertainty on the amount of integrated luminosity delivered by the LHC during 2012 [56].

Uncertainties on the parton distribution functions (PDFs) are evaluated according to the PDF4LHC prescription [57], which combines uncertainties on the CT10, MSTW2008NLO and NNPDF2.3 [58] PDF sets. PDF uncertainties are applied only to the shape of the W+jets background, since the normalization is estimated from data.

Variation	Percentage variation (%)	
	Electron channel	Muon channel
MET+m_T (from < 60GeV to < 50GeV)	9.4	11.8
MET (from < 20GeV to < 15GeV)	11.6	14.7
$S(d_0^e)$ (from > 2.5 to > 2.7)	7.9	-
$S(d_0^\mu)$ (from > 3.2 to > 3.4)	-	9.2
χ^2 cut (from > 0.9 to < 0.85)	11.6	14.7
Efficiency statistical unc.	0.34	0.03
Fake rate statistical unc.	9.5	5.2
Sum in quadrature	22	26

Table 11.1: Impacts of the systematic uncertainty on the multijet background, in the resolved channel.

11.2 Uncertainties on Data Driven Background Estimates

The estimation of the W+jets background was presented Section 9.1, while that of background sources from non-prompt leptons (ie. multijet background) was described in Section 9.2. In the resolved channel, the uncertainty on the normalization of the multijet background was conservatively taken as 22% and 26% for the electron and muon channels respectively, while the uncertainties in the boosted channel are 12% and 13%. This is sufficient to cover variations seen based on alternative choices of the parameterization of efficiency and fake rates, the control regions, loose lepton definitions and other factors, as shown in Tables 11.1 and 11.2.

The uncertainties on the W+jets background normalization and heavy flavor scale factors listed in Tables 9.1 and 9.2 are estimated from the statistical uncertainties of the charge asymmetry method as well as systematic uncertainties on the underlying MC, detector resolution, identification, and event reconstruction. These uncertainties on the heavy flavor fraction of the W+jets background is described by three components: the

Variation	Percentage variation (%)	
	Electron channel	Muon channel
MET+m_T (from < 60GeV to < 50GeV)	5.7	1.5
MET (from < 20GeV to < 15GeV)	3.6	6.7
$S(d_0^e)$ (from > 2.5 to > 2.7)	4.5	-
$S(d_0^\mu)$ (from > 3.2 to > 3.4)	-	1.5
Large-R jet mass	5.1	0.9
Large-R jet p_T	2.3	8.0
Efficiency statistical unc.	0.49	0.08
Fake rate statistical unc.	6.0	6.6
Sum in quadrature	12	13

Table 11.2: Impacts of the systematic uncertainty on the multijet background, in the boosted channel.

$K_{b\bar{b}} = K_{c\bar{c}}$ and K_c scale factors are varied assuming full correlation (denoted WHFC0), $K_{b\bar{b}} = K_{c\bar{c}}$ is varied alone (WHFC3) and K_c is varied alone (WHFC4.)

11.3 Uncertainties Impacting the Modeling of the SM $t\bar{t}$ Background

Particular attention is paid to the modeling of the SM $t\bar{t}$ background, and several systematic uncertainties are applied to it's estimation.

The nominal expected SM $t\bar{t}$ background sample was generated by the POWHEG+PYTHIA. Uncertainty on the MC generator model is estimated by comparing the shape of this sample to those generated by MC@NLO+Herwig and POWHEG+Herwig. An additional systematic uncertainty which arises from the uncertainty on the mass of the top quark itself is estimated by generating MC samples with a top mass of 170 and 175 GeV. Uncertainty on the modeling of the initial and final state radiation (ISR and FSR) is derived by generating samples in ACERMC+PYTHIA while varying parameters in PYTHIA.

Finally, an additional uncertainty of 6.5% is introduced on the overall cross section of the $t\bar{t}$ background produced by 8 TeV proton-proton collisions.

The SM $t\bar{t}$ sample is corrected for the electroweak scale at next-to-leading order according to calculations provided by Kuhn et al. [59; 60; 61]. A 10% uncertainty is assumed on the size of this correction, but was seen to have a negligible impact on the results and is not considered in the final analysis.

11.4 *b*-tagging Efficiency Scale Factors and Uncertainties

The MV1 *b*-tagging algorithm and its respective constituents were trained on an inclusive MC sample. A series of efficiency and inefficiency scale factors are then applied to correct for differences in b-tagging efficiencies between data and MC. These scale factors are defined in terms of the measured b-tagging efficiencies in MC (ϵ_{MC}) and data (ϵ_{data}):

$$SF_{\text{eff}} = \frac{\epsilon_{\text{data}}}{\epsilon_{\text{MC}}}, \tag{11.1}$$

$$SF_{\text{ineff}} = \frac{1 - \epsilon_{\text{data}}}{1 - \epsilon_{\text{MC}}}. \tag{11.2}$$

Each MC event is then assigned a weight based on the product of efficiency and inefficiency scale factors for each jet. Provided that ϵ_{MC} is correctly measured, this procedure will not affect the total weighted number of events or the heavy flavor composition of a MC sample. However, the reweighted events will change the composition of events to more accurately reflect the b-tagging efficiency in data. In addition, the systematic uncertainty on the b-tagging efficiency can be modeled by increasing or reducing the relevant scale factors.

The *b*-tagging efficiency is parameterized in jet p_T and η. However, The MV1 algorithm is trained to tag isolated jets originating from a single parton, and it's efficiency will suffer in a crowded environment in which multiple partons are emitted in a similar direction from a collision, a scenario which is expected to be common in events containing high p_T top quarks. As this effect is present in both data and MC, the efficiency scale factors are still valid. However, the inefficiency scale factors shown in Equation 11.2 will not be correct if

the underlying efficiency is not accurately modeled. This leads to an artificial enhancement of the total event yields by up to 15% in a boosted environment, as shown in Figure 11.1a. This also leads to a severe mismodeling of b-tagging systematics.[1]

For this reason, an additional correction factor is applied to the estimated b-tagging efficiency for each jet based on ΔR_{Jfit}, the distance between the jet axis and the B-hadron candidate as identified by the JetFitter algorithm. This variable effectively discriminates between jets originating from an isolated parton and those influenced by other nearby partons which will shift the direction of the jet axis. Figure 11.1b shows that the b-tagging efficiency has a strong dependence on this variable which is not modeled by the official efficiencies parameterized in η and p_T.

Similar scale factors are considered for the efficiencies to tag a jet originating from a light flavored quarks and gluons or charm quarks, referred to as the mistag and c-tag rates respectively. The impact of systematic uncertainties is estimated by varying each of the scale factors. In the case of b-tagging efficiencies, the uncertainty was broken down into eleven components, of which four are observed to be significant. The c-tag and mistag uncertainties are treated as a single component each.

11.5 Other Uncertainties on Reconstructed Objects

Additional uncertainties are considered on the identification and reconstruction of jets, leptons, and $E_{\mathrm{T}}^{\mathrm{miss}}$ in an event. A number of sources of uncertainty on the jet energy scale (JES)[2] are considered, including those accounting for the heavy flavor composition of jets, the impact of close-by jets, pileup, and other factors. Four components are identified as having a significant impact and are treated individually, while the impact of 19 remaining sources of uncertainty are considered as a single component by evaluating their joint impact on each jet. Additionally, the impact of reducing the jet energy resolution (JER) is also considered. Similar uncertainties are included on the calibration and resolution of Large-R

[1] Incorrectly modeling inefficiency scale factors can produce situations in which the expected event yield after b-tagging moves in the opposite direction as the b-tagging efficiency.

[2] The calibration of the jet energy measurement based on the response of the ID and calorimeters.

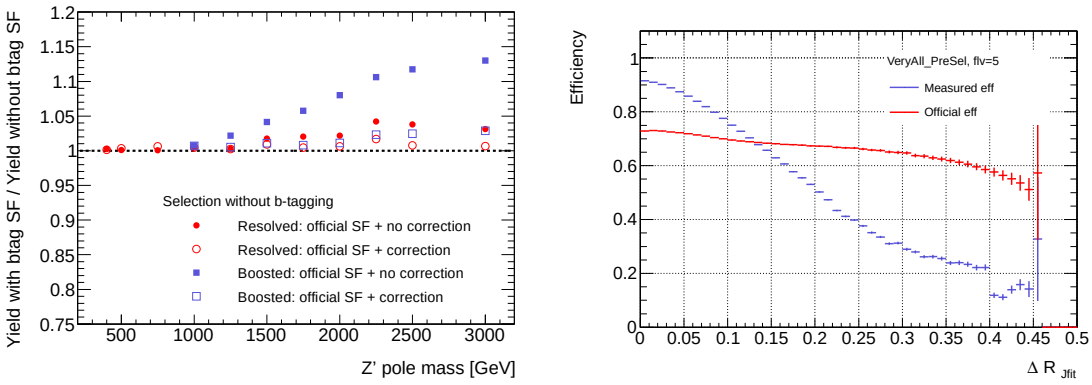

(a) (b)

Figure 11.1: Left: Impact of b-tagging scale factors on the event yield for several Z' samples before applying b-tagging or the χ^2 cut in the resolved selection. Right: b-tagging efficiency measured in Monte Carlo as a function ΔR_{Jfit} compared to the officially estimated efficiency determined by the η and p_T of a jet.

jet energy and mass scales (BoostedJES, BoostedJMS, and BoostedJER respectively.) In the case of the BoostedJES, 2 out of 16 components are considered large and the remainder are merged into a single component on a per jet basis.

Differences in the the lepton trigger and identification efficiencies between data and Monte Carlo are corrected by applying a scale factor weight to Monte Carlo events. Uncertainties on these efficiencies, including the impact of isolation and lepton-in-jet treatment, are modeled by varying these scale factors. Additional corrections are applied to the reconstruction of lepton p_T and position in the Monte Carlo to correct observed differences in the data. However, the uncertainty on this calibration is not considered due to its very small impact.

11.6 Summary of Systematic Treatment and Impact

The impact of each systematic on the expected yield of each background and on a 1.5 TeV Z' boson signal is shown in Table 11.3 and 11.4 for the resolved and boosted selections respectively.

Systematic effect	tot.bgr	$t\bar{t}$	sing.top	W+jets	Multi-Jet	Z+jets	Dibosons	ttV	Z' 1.5 TeV
Electron scale factor	0.4	0.4	0.4	0.4	0.0	0.5	0.4	0.8	0.9
Muon scale factor	0.9	1.0	1.0	0.9	0.0	0.6	1.0	1.0	1.0
$t\bar{t}$ generator	1.5	1.7	0.0	0.0	0.0	0.0	0.0	0.0	0.0
Parton shower	3.0	3.5	0.0	0.0	0.0	0.0	0.0	0.0	0.0
EW Sudakov	0.2	0.2	0.0	0.0	0.0	0.0	0.0	0.0	0.0
ISR/FSR	3.1	3.6	0.0	0.0	0.0	0.0	0.0	0.0	0.0
topmass	0.3	0.3	0.0	0.0	0.0	0.0	0.0	0.0	0.0
Jet energy res.	1.1	1.9	0.9	6.1	0.0	11.7	5.7	1.4	1.3
BoostedJES0 (Gamma-jet)	0.1	0.1	0.0	0.0	0.0	0.0	0.0	0.2	0.8
BoostedJES13 (Topology)	0.1	0.1	0.1	0.0	0.0	0.0	0.1	0.3	1.3
BoostedJES14 (DoubleRatio)	0.0	0.0	0.0	0.0	0.0	0.0	0.0	0.0	0.0
BoostedJES15 (NPV)	0.0	0.0	0.0	0.0	0.0	0.0	0.0	0.0	0.1
BoostedJES16 (μ)	0.0	0.0	0.0	0.0	0.0	0.0	0.0	0.0	0.1
BoostedJMS	0.0	0.0	0.0	0.0	0.0	0.0	0.0	0.1	2.0
$t\bar{t}$ norm	5.4	6.2	0.0	0.0	0.0	0.0	0.0	0.0	0.0
Luminosity	2.5	2.8	2.8	0.0	0.0	2.8	2.8	2.8	2.8
b-tag7	0.2	0.2	0.4	0.2	0.0	0.2	0.0	0.2	0.4
b-tag8	0.7	0.7	1.1	0.5	0.0	0.6	0.2	0.6	0.5
b-tag9	0.9	0.9	1.4	0.7	0.0	1.0	0.2	0.9	0.1
b-tag10 (Crowded Environment)	0.0	0.0	0.0	0.0	0.0	0.0	0.0	0.0	1.4
c-tag	0.3	0.1	0.1	4.9	0.0	3.8	6.0	0.1	0.9
Mistag	0.2	0.0	0.0	3.1	0.0	3.8	2.6	0.0	0.1
JES3 (Modelling1)	3.4	3.1	4.8	6.7	0.0	7.9	5.1	1.2	1.9
JES7 (Detector1)	0.4	0.4	0.7	1.1	0.0	1.5	0.6	0.2	0.3
JES12 (Eta Intercalibration)	1.1	1.0	2.0	2.2	0.0	3.5	2.5	0.1	0.8
JES20 (Pileup Rho)	3.5	3.0	4.9	8.2	0.0	9.5	6.2	1.5	2.1
Small JES Components	4.3	3.9	6.1	9.0	0.0	10.0	7.0	1.7	2.0

Table 11.3: Impact of considered systematics on the expected yield of each background and on a 1.5 TeV Z' boson in the resolved channel.

In order to improve stability in the statistical analysis, systematics are not considered in channels in which their impact (on both the shape and on the total event yield) is deemed to be negligible. In particular, the lepton scale factor uncertainties are applied only to the overall normalization. Likewise, the impact of BoostedJES and BoostedJMS systematics are not considered in the resolved channel. Finally, only the JES, BoostedJES, BoostedJMS, b-tagging, and luminosity uncertainties are applied to the signal samples.

Systematic effect	tot.bgr	$t\bar{t}$	sing.top	W+jets	multi-jet	Z+jets	Di-bosons	ttV	Z' 1.5 TeV
Electron scale factor	1.1	1.2	1.0	0.9	0.0	1.8	1.0	1.2	1.8
Muon scale factor	1.0	1.0	1.0	1.0	0.0	0.8	1.0	1.1	1.1
$t\bar{t}$ generator	7.5	8.6	0.0	0.0	0.0	0.0	0.0	0.0	0.0
Parton shower	6.1	7.0	0.0	0.0	0.0	0.0	0.0	0.0	0.0
EW Sudakov	0.4	0.5	0.0	0.0	0.0	0.0	0.0	0.0	0.0
ISR/FSR	0.7	0.8	0.0	0.0	0.0	0.0	0.0	0.0	0.0
topmass	0.7	0.8	0.0	0.0	0.0	0.0	0.0	0.0	0.0
Jet energy res.	0.4	0.5	1.2	0.1	0.0	0.5	2.8	0.8	0.9
BoostedJES0 (Gamma-jet)	5.4	5.5	5.1	4.7	0.0	6.5	4.8	3.4	0.6
BoostedJES13 (Topology)	8.7	8.9	8.1	7.6	0.0	8.2	6.9	5.6	0.7
BoostedJES14 (DoubleRatio)	0.0	0.0	0.0	0.0	0.0	0.0	0.0	0.0	0.0
BoostedJES15 (NPV)	0.1	0.1	0.2	0.1	0.0	1.1	0.6	0.0	0.0
BoostedJES16 (μ)	0.1	0.1	0.0	0.0	0.0	0.2	0.3	0.1	0.0
BoostedJMS	3.5	3.3	4.9	5.8	0.0	6.5	9.9	3.1	2.5
$t\bar{t}$ norm	5.4	6.2	0.0	0.0	0.0	0.0	0.0	0.0	0.0
Luminosity	2.6	2.8	2.8	0.0	0.0	2.8	2.8	2.8	2.8
b-tag7	0.7	0.7	1.0	0.5	0.0	0.5	0.3	0.9	1.0
b-tag8	1.4	1.5	1.9	1.0	0.0	1.2	0.6	1.6	1.5
b-tag9	0.6	0.6	1.0	0.4	0.0	0.5	0.4	0.7	0.5
b-tag10 (Crowded Environment)	2.2	2.2	3.5	1.8	0.0	1.9	0.6	3.5	12.1
c-tag	0.2	0.3	0.4	5.3	0.0	3.8	6.2	0.4	2.1
Mistag	0.3	0.1	0.0	3.2	0.0	5.8	3.4	0.1	0.0
JES3 (Modelling1)	0.1	0.1	0.5	0.1	0.0	0.1	1.5	0.1	0.2
JES7 (Detector1)	0.1	0.1	0.9	0.1	0.0	0.6	0.5	0.1	0.3
JES12 (Eta Intercalibration)	0.3	0.3	0.7	0.3	0.0	3.2	1.4	0.1	0.5
JES20 (Pileup Rho)	0.2	0.3	0.5	0.2	0.0	3.5	1.0	0.2	0.3
Small JES Components	0.1	0.2	0.9	0.1	0.0	2.8	2.2	0.2	0.4

Table 11.4: Impact of considered systematics on the expected yield of each background and on a 1.5 TeV Z' boson in the boosted channel.

Chapter 12

Results

In order to perform a statistical analysis on the results, this search utilizes HistFitter, a statistical package developed by the ATLAS collaboration based on HistFactory [62], RooStats [63], and RooFit [64]. The compatibility of the observed data with the SM hypothesis after considering systematics is discussed in Section 12.1. Section 12.2 presents 95% confidence level limits on the benchmark signal processes.

In order to improve the stability of the statistical analysis, the last two bins of each of the resolved channels are excluded due to very low statistics.

12.1 Compatibility with the Standard Model

Consistency with the SM is checked by comparing the observed data to the SM expectations. Figures 9.8 and 9.9 show the observed data and the expected nominal background for each channel and b-tagging category. The data is in reasonable agreement with the expected backgrounds. This comparison, along with the expected contribution from a 2 TeV Z' boson is also shown for the combination of all resolved channels in Figure 12.1a, for all boosted channels in Figure 12.1b and for the combination of all channels in Figure 12.1c.

In addition to comparing data to the nominal expected $m_{t\bar{t}}$ distributions, the expected background is fit to the data. The poisson likelihood function for the background only

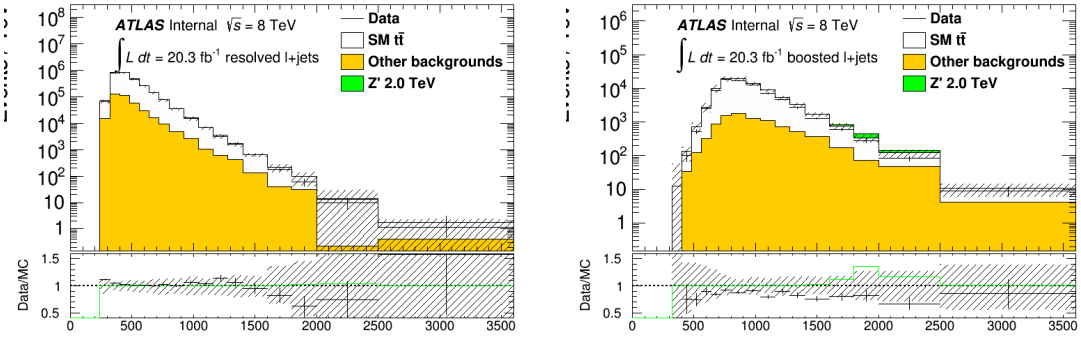

(a) Resolved Selections

(b) Boosted Selections

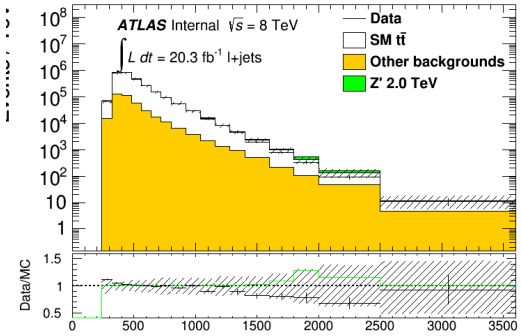

(c) All Selections

Figure 12.1: Observed vs expected $m_{t\bar{t}}$ distributions of events after fitting the systematic nuissance parameters to the observed data. Events are summed over all resolved channels (a), all boosted channels (b), and the combination of resolved and boosted channels (c). Also shown is the expected contribution from a 2 TeV Z'.

hypothesis is defined as

$$L_0(D|\Theta) = \prod_{i=1}^{N} \frac{e^{-b_i)}(b_i)^{D_i}}{\Gamma(D_i+1)}, \tag{12.1}$$

where the index i runs over all of the bins in each of the 12 channels and b-tagging categories described in Section 8. b_i and D_i denote the sum of the expected number of background events in each bin, and θ represents the collection of nuisance parameters which reflect the systematic uncertainties on the shape and size of the expected background.

A fit is performed over the nuisance parameters to maximize this likelihood function given the observed data using the Minuit2 minimization routine [65] interfaced with HistFitter. The resulting values of the systematics are shown in Figure 12.2 while Figure 12.3 shows the correlations between the fitted parameters. The observed data is compared to the expected background before and after fitting in Figures 12.4 and 12.5 for the resolved and boosted channels respectively.

12.2 Upper Limits on $t\bar{t}$ Resonance Production Cross Sections

As shown in the previous section, the observed data is broadly consistent with the Standard Model background expectation. Therefore, upper limits may be set on the production cross section of the benchmark models described in Chapter 2.

These upper cross section limits are set using an asymptotic approximation [66] to CLs technique [67], implemented in HistFitter. The poisson likelihood function for a given signal model ν is defined in similar fashion as Equation 12.1:

$$L(D|\sigma_\nu, \Theta) = \prod_{i=1}^{N} \frac{e^{-(a_{\nu,i}\sigma_\nu\mu+b_i)}(a_{\nu,i}\sigma_{\nu,i}\mu+b_i)^{D_i}}{\Gamma(D_i+1)}, \tag{12.2}$$

where the parameters σ_ν, a_ν and μ have been introduced to denote nominal cross section of the benchmark signal process, the acceptance of events for a given signal and the strength of the signal process to be tested relative to the benchmark respectively.

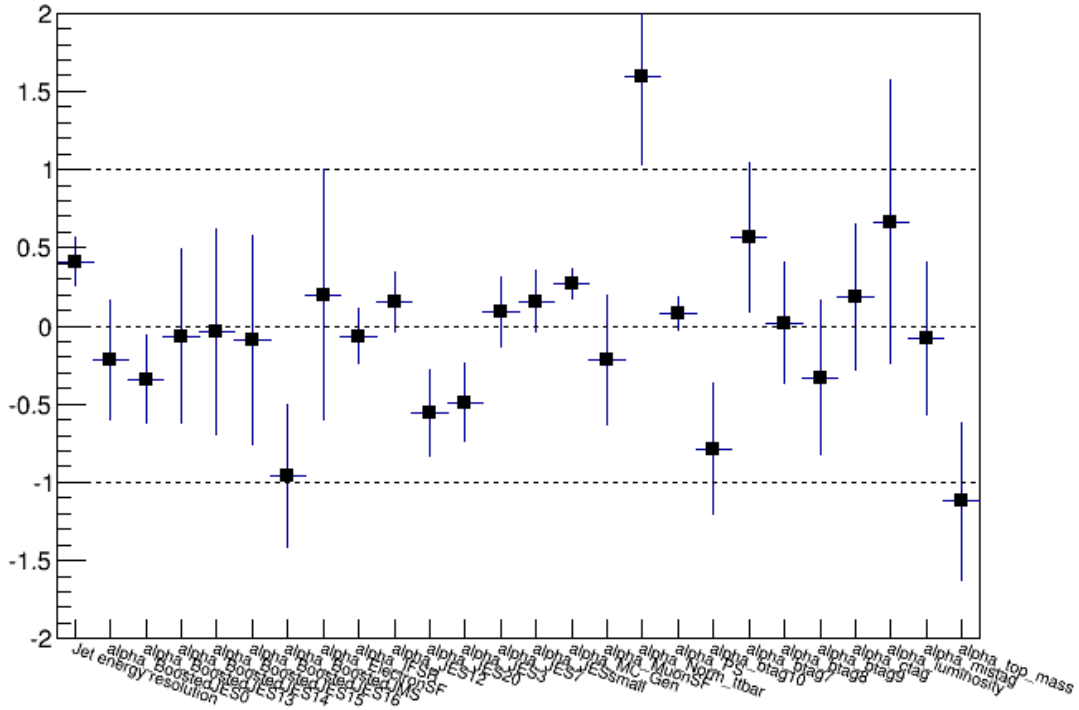

Figure 12.2: Best fit values of the nuisance parameters and their uncertainties. 0 denotes the nominal value of each systematic.

A test statistic, t_μ for evaluating the compatibility of the data with a given signal strength μ is then defined in terms of the profile likelihood ratio:

$$t_\mu = -2\ln(\lambda(\mu)), \tag{12.3}$$

$$\lambda(\mu) = \frac{L(\mu, \hat{\hat{\theta}}(\mu))}{L(\hat{\mu}, \hat{\theta})}. \tag{12.4}$$

In Equation 12.4,$\hat{\hat{\theta}}(\mu)$ is the combination of nuisance parameter values which maximizes the likelihood function for a fixed value of μ, the so-called conditional maximum likelihood estimator. Similarly $\hat{\mu}$ and $\hat{\theta}$ denote the values of the signal strength and nuisance parameters which together maximize the likelihood function subject to the condition that $0 < \hat{\mu} < \mu$. By construction, $0 <= \lambda(\mu) <= 1$, with larger values indicating better agreement between a test hypothesis and the data. Likewise, $t_\mu >= 0$, with larger values indicating greater disagreement between the data and a signal of size μ. A given observed

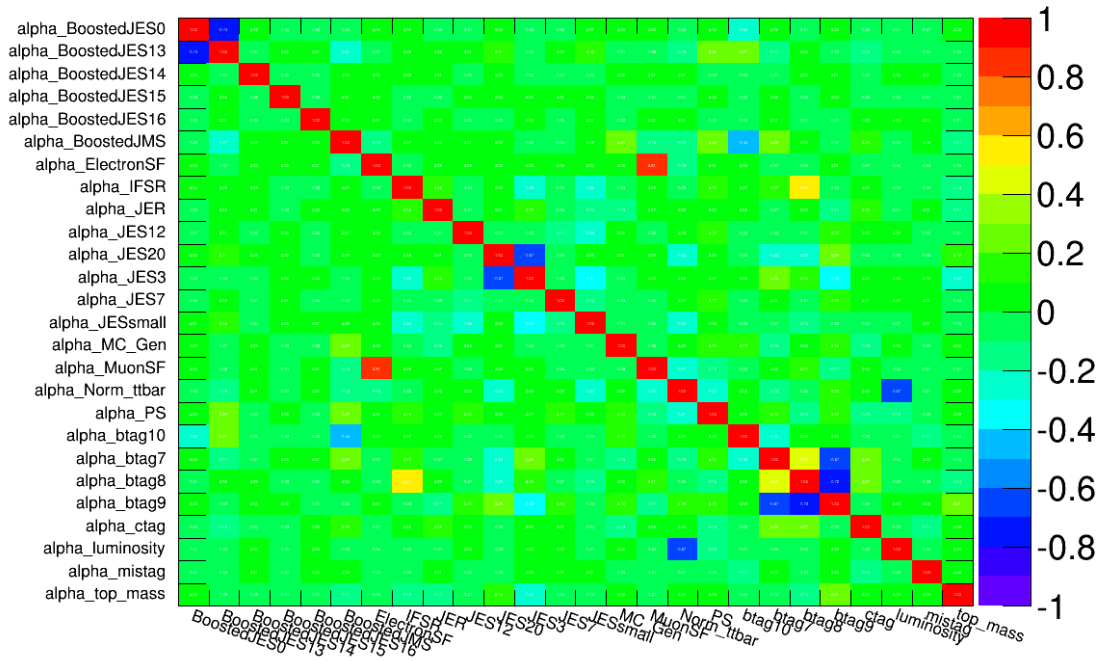

Figure 12.3: Correlation between nuissance parameters in a background only maximum likelihood fit.

value of the test statistic, $t_{\mu,obs}$, is converted into a p-value for the signal hypothesis (referred to as CL_{s+b}) with the help of $f(t_\mu|\mu)$, the conditional probability distribution function of t_μ:

$$CL_{s+b} = p(t_\mu > t_{\mu,obs}|\mu) = \int_{t_{\mu,obs}}^{\infty} f(t_\mu|\mu)dt_\mu. \tag{12.5}$$

Similarly, a p-value for the background only hypothesis, CL_b, is evaluated using an appropriate probability distribution function:

$$CL_b = p(t_\mu > t_{\mu,obs}|0) = \int_{t_{\mu,obs}}^{\infty} f(t_\mu|0)dt_\mu. \tag{12.6}$$

Traditional frequentist methods evaluate $f(t_\mu)$ by considering a series of toy experiments in which pseudo-data is generated randomly according to input models corresponding to the background only and signal plus background hypothesis. This search uses an asymptotic approach which assumes that $\hat{\mu}$ is approximately Gaussian in nature, is centered at the true signal strength (μ') and has standard deviation (σ). The following approximation was

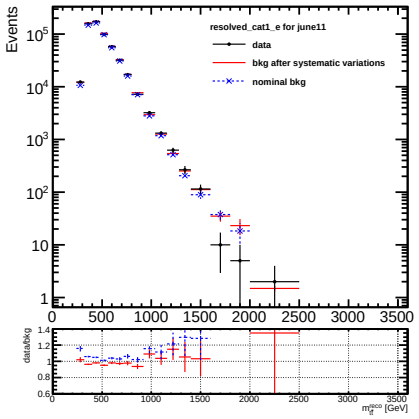

(a) Electron channel, category 1

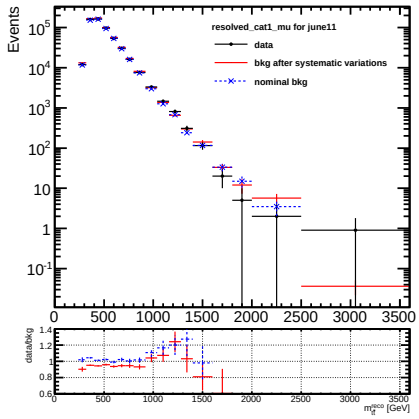

(b) Muon channel, category 1

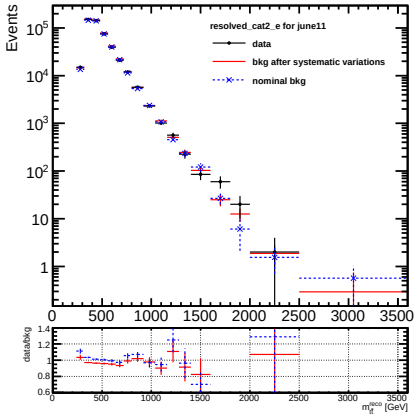

(c) Electron channel, category 2

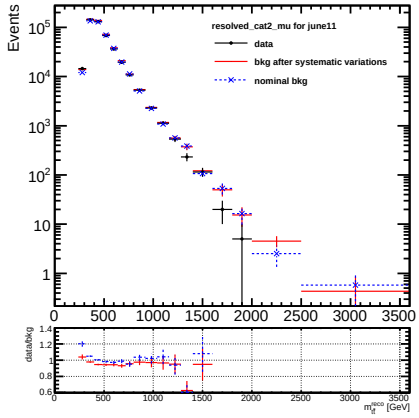

(d) Muon channel, category 2

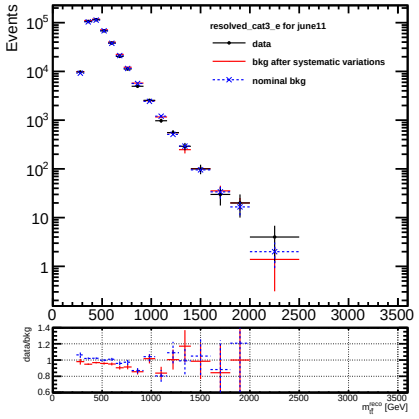

(e) Electron channel, category 3

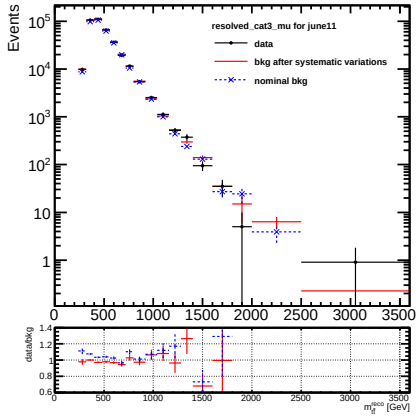

(f) Muon channel, category 3

Figure 12.4: Data and expected backgrounds before and after performing maximum likelihood fit in the resolved channel.

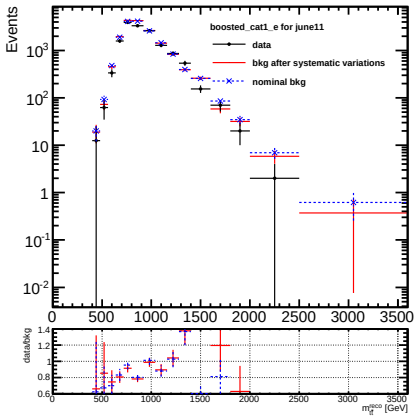

(a) Electron channel, category 1

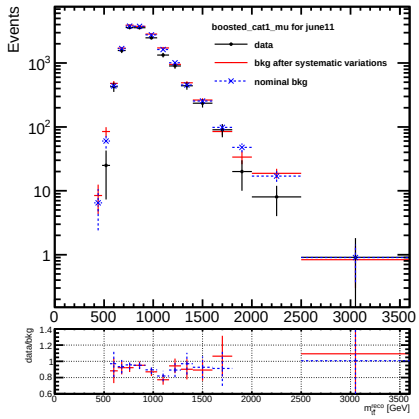

(b) Muon channel, category 1

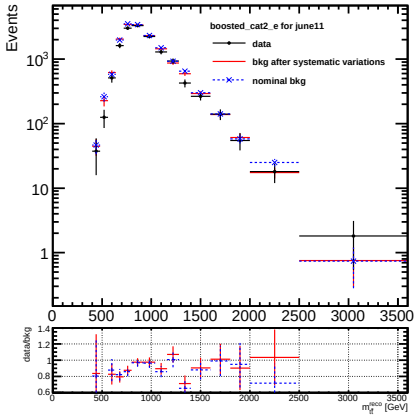

(c) Electron channel, category 2

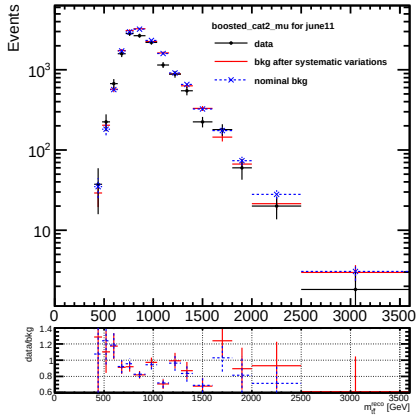

(d) Muon channel, category 2

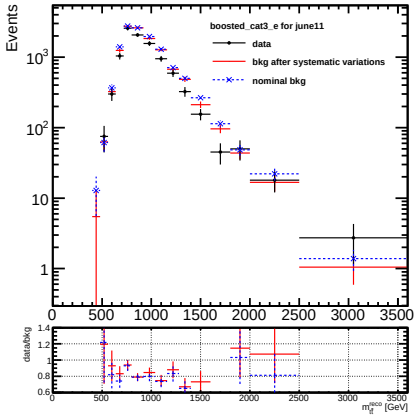

(e) Electron channel, category 3

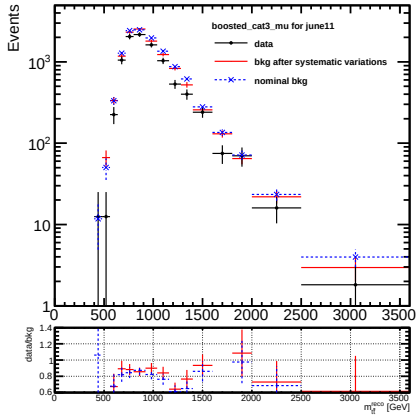

(f) Muon channel, category 3

Figure 12.5: Data and expected backgrounds before and after performing maximum likelihood fit in the boosted channel.

demonstrated by Wald [68]:

$$t_\mu \approx \frac{(\mu - \hat{\mu})^2}{\sigma^2}. \tag{12.7}$$

$f(t_\mu)$ may then be approximated as a non-central chi-square distribution with a single degree of freedom:

$$f(t_\mu) \approx \frac{1}{2\sqrt{2\pi t_\mu}}[e^{-\frac{1}{2}(\sqrt{t_\mu}+\sqrt{\Lambda})^2} + e^{-\frac{1}{2}(\sqrt{t_\mu}-\sqrt{\Lambda})^2}], \tag{12.8}$$

where Λ is the non-centrality parameter defined as

$$\Lambda = \frac{(\mu - \mu')^2}{\sigma^2}. \tag{12.9}$$

Finally, the standard deviation, σ, is found with the help of the so called Asimov data set, a representative artificial data set with no statistical fluctuations:

$$t_{\mu,Asimov} \approx \frac{(\mu - \mu'_{Asimov})^2}{\sigma_\mu^2}. \tag{12.10}$$

Values of CL_{s+b} which are close to 0 disfavor the signal hypothesis, while the background hypothesis is disfavored when CL_b is close to 1. In the CLs technique, the limit is set by considering the ratio between CL_{s+b} and CL_b:

$$CL_s = \frac{CL_{s+b}}{CL_b}, \tag{12.11}$$

and a signal strength μ will then be excluded at the 95% level if $CL_s < .05$.

This particular approach to constructing a confidence interval eliminates the possibility of excluding a signal point to which an experiment is not sensitive due to a statistical fluctuation by penalizing the effective p-value of the chosen test statistic. This makes the CLs technique a conservative choice of statistical test in the sense that the probability for a true signal to be excluded at a 95% confidence level will tend to be somewhat less than 5%. [1]

Expected and observed upper cross section limits, accounting for both statistical and systematic uncertainties, are shown in Figure 12.6. Figure **??** shows the resulting limits when only statistical uncertainties are considered. Finally, limits produced considering only the resolved or only the boosted channels are shown in Figures 12.7 and 12.8 respectively.

[1] More traditional frequentist statistical approaches guarantee that a true signal will have a 5% chance to be excluded from a 95% confidence level interval, even if the experiment has no sensitivity!

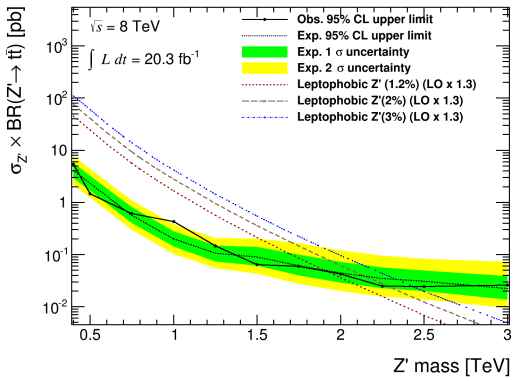

(a) Z' boson

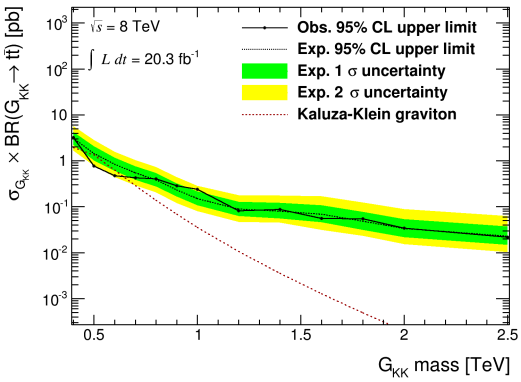

(b) Kaluza-Klein Graviton

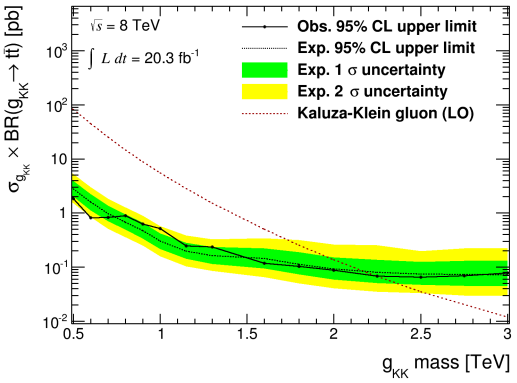

(c) Kaluza-Klein Gluon

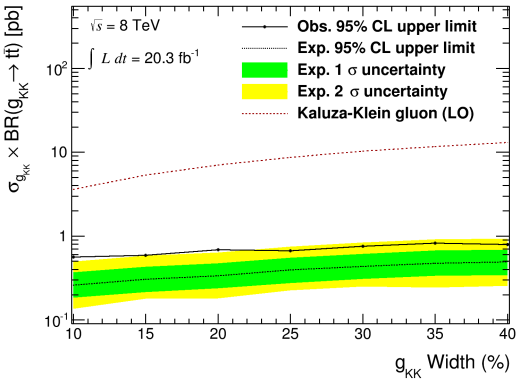

(d) Kaluza-Klein Gluon (1 TeV)

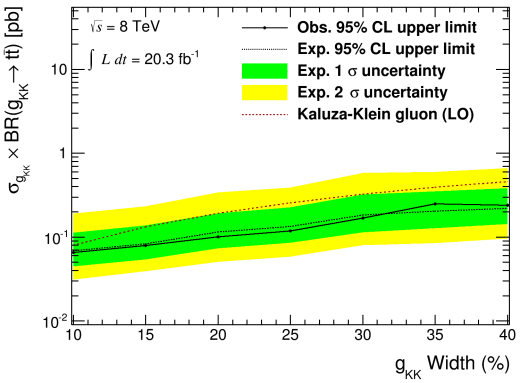

(e) Kaluza-Klein Gluon (2 TeV)

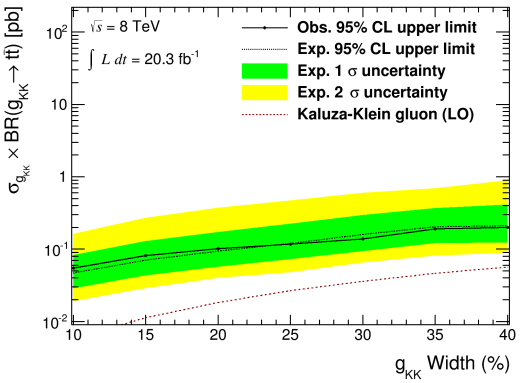

(f) Kaluza-Klein Gluon (3 TeV)

Figure 12.6: Expected and observed upper limits on the cross sections times $t\bar{t}$ branching ratios of the chosen benchmark models. Both the resolved and boosted channels are considered, and both systematic and statistical uncertainties are accounted for.

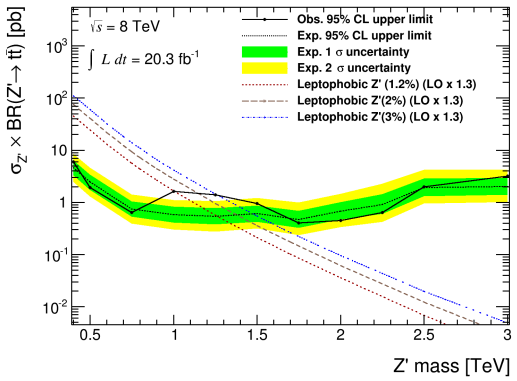

(a) Z' boson

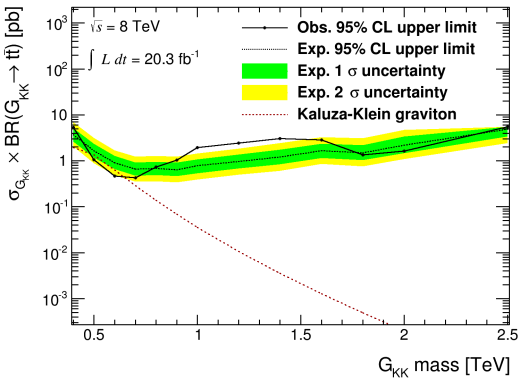

(b) Kaluza-Klein Graviton

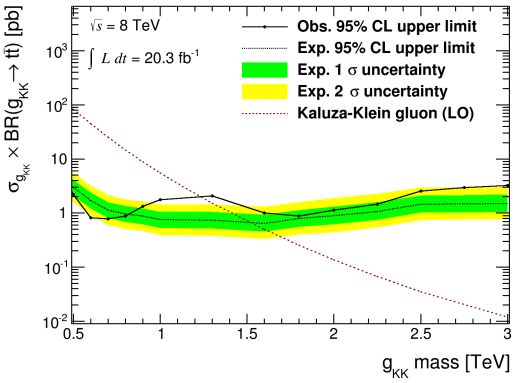

(c) Kaluza-Klein Gluon

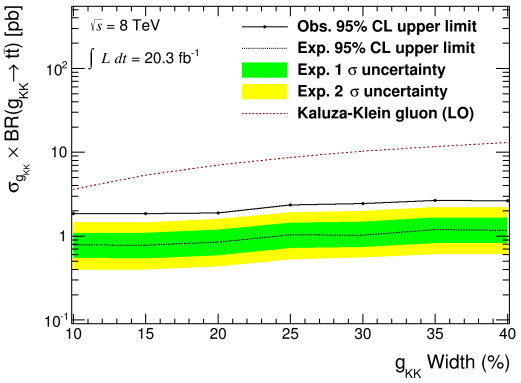

(d) Kaluza-Klein Gluon (1 TeV)

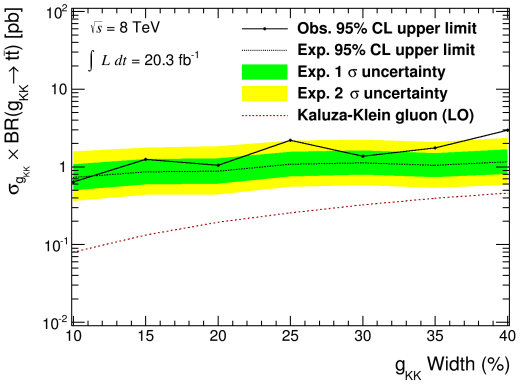

(e) Kaluza-Klein Gluon (2 TeV)

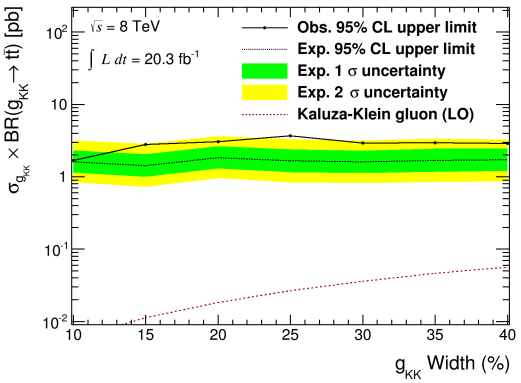

(f) Kaluza-Klein Gluon (3 TeV)

Figure 12.7: Expected and observed upper limits on the cross sections times $t\bar{t}$ branching ratios of the chosen benchmark models. Only the resolved channels are considered. Both systematic and statistical uncertainties are accounted for.

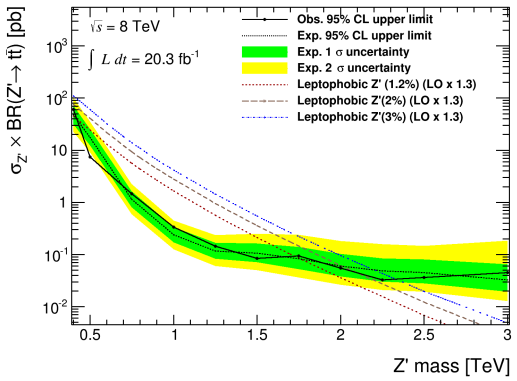

(a) Z' boson

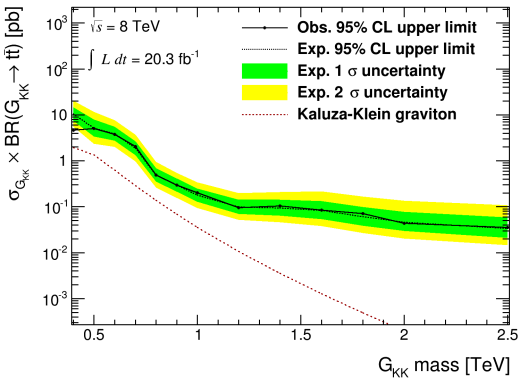

(b) Kaluza-Klein Graviton

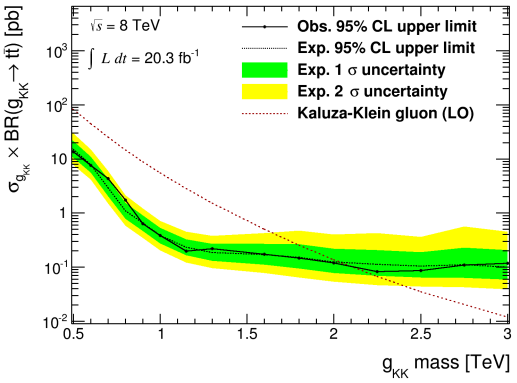

(c) Kaluza-Klein Gluon

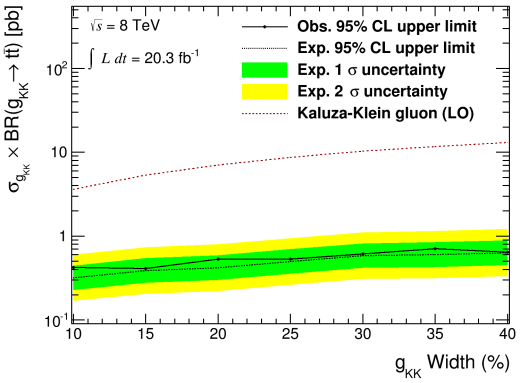

(d) Kaluza-Klein Gluon (1 TeV)

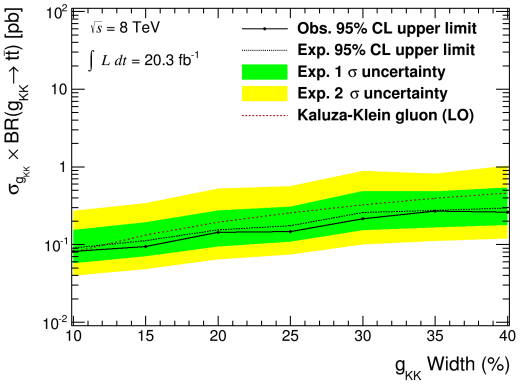

(e) Kaluza-Klein Gluon (2 TeV)

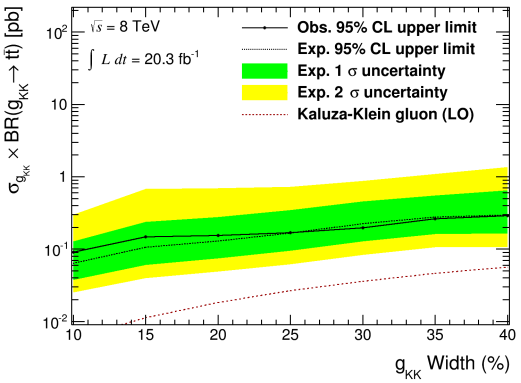

(f) Kaluza-Klein Gluon (3 TeV)

Figure 12.8: Expected and observed upper limits on the cross sections times $t\bar{t}$ branching ratios of the chosen benchmark models. Only the boosted channels are considered. Both systematic and statistical uncertainties are accounted for.

12.3 Conclusions and Outlook

A search for a new heavy resonance decaying to $t\bar{t}$ pairs over a wide range of masses utilizing 20.3 fb^{-1} of proton-proton collision data collected at the ATLAS detector at 8 TeV center-of-mass energy has been presented. The observed data is broadly consistent with the SM hypothesis after considering systematic and statistical uncertainties. As no new particle is observed, upper limits are set on the cross sections times branching ratios of several benchmark models and a wide range of potential signals.

ATLAS is expected to achieve an even greater sensitivity to such signals in the future, particularly for resonances with a mass between 2 and 5 TeV. Increasing the center-of-mass collision energy from the 8 TeV used in this analysis to 13 TeV will result drastically higher theoretical cross sections for all models considered. Meanwhile, years of future running, as well as the LHC high luminosity upgrade expected around 2020 will eventually result in more than 3000 fb^{-1} of data collected. However, in order to achieve the best possible sensitivity in such an environment, improvements must be made in a number of areas, including the efficiency of b-tagging in crowded environments and the use of substructure to identify the hadronic decays of high p_T top quarks.

Bibliography

[1] F. Abe et al. Observation of top quark production in $p\bar{p}$ collisions with the collider detector at fermilab. *Phys. Rev. Lett.*, 74:2626–2631, Apr 1995.

[2] S. Abachi et al. Observation of the top quark. *Phys. Rev. Lett.*, 74:2632–2637, Apr 1995.

[3] K. Kodama et al. Observation of tau neutrino interactions. *Phys.Lett.*, B504:218–224, 2001.

[4] Georges Aad et al. Observation of a new particle in the search for the Standard Model Higgs boson with the ATLAS detector at the LHC. *Phys.Lett.*, B716:1–29, 2012.

[5] Serguei Chatrchyan et al. Observation of a new boson at a mass of 125 GeV with the CMS experiment at the LHC. *Phys.Lett.*, B716:30–61, 2012.

[6] D. Hanneke, S. Fogwell, and G. Gabrielse. New Measurement of the Electron Magnetic Moment and the Fine Structure Constant. *Physical Review Letters*, 100(12):120801, March 2008.

[7] W. Pauli. The connection between spin and statistics. *Phys. Rev.*, 58:716–722, Oct 1940.

[8] Wolfgang Ochs. The Status of Glueballs. *J.Phys.*, G40:043001, 2013.

[9] J. Beringer et al. Review of Particle Physics (RPP). *Phys.Rev.*, D86:010001, 2012.

[10] P.A.R. Ade et al. Planck 2013 results. I. Overview of products and scientific results. 2013.

[11] Christopher T. Hill. Topcolor assisted technicolor. *Phys.Lett.*, B345:483–489, 1995.

[12] Robert M. Harris, Christopher T. Hill, and Stephen J. Parke. Cross section for topcolor Z'(t) decaying to t anti-t. 1999.

[13] Robert M. Harris and Supriya Jain. Cross Sections for Leptophobic Topcolor Z' decaying to top-antitop. 2011.

[14] Jun Gao, Chong Sheng Li, Bo Hua Li, C.-P. Yuan, and Hua Xing Zhu. Next-to-leading order QCD corrections to the heavy resonance production and decay into top quark pair at the LHC. *Phys.Rev.*, D82:014020, 2010.

[15] Fabrizio Caola, Kirill Melnikov, and Markus Schulze. A complete next-to-leading order QCD description of resonant Z' production and decay into $t\bar{t}$ final states. *Phys.Rev.*, D87(3):034015, 2013.

[16] Lisa Randall and Raman Sundrum. A Large mass hierarchy from a small extra dimension. *Phys.Rev.Lett.*, 83:3370–3373, 1999.

[17] Ben Lillie, Lisa Randall, and Lian-Tao Wang. The Bulk RS KK-gluon at the LHC. *JHEP*, 0709:074, 2007.

[18] Kaustubh Agashe, Hooman Davoudiasl, Gilad Perez, and Amarjit Soni. Warped Gravitons at the LHC and Beyond. *Phys.Rev.*, D76:036006, 2007.

[19] Oliver Sim Bruning, Paul Collier, P Lebrun, Stephen Myers, Ranko Ostojic, John Poole, and Paul Proudlock. *LHC Design Report*. CERN, Geneva, 2004.

[20] M. Benedikt, P. Collier, V. Mertens, J. Poole, and K. Schindl. LHC Design Report. 3. The LHC injector chain. 2004.

[21] A.M. Sessler, E. Wilson, and E.J.N. Wilson. *Engines of discovery: a century of particle accelerators*. World Scientific, 2007.

[22] E. Wilson and E.J.N. Wilson. *An Introduction to Particle Accelerators*. Oxford University Press, 2001.

[23] *LEP design report*. CERN, Geneva, 1984. Copies shelved as reports in LEP, PS and SPS libraries.

[24] Lucio Rossi. Superconductivity: its role, its success and its setbacks in the large hadron collider of cern. *Superconductor Science and Technology*, 23(3):034001, 2010.

[25] The ATLAS Collaboration. The atlas experiment at the cern large hadron collider. *Journal of Instrumentation*, 3(08):S08003, 2008.

[26] Vasiliki A. Mitsou. The ATLAS transition radiation tracker. 2003.

[27] Georges Aad et al. Performance of the ATLAS Trigger System in 2010. *Eur.Phys.J.*, C72:1849, 2012.

[28] W Lampl, S Laplace, D Lelas, P Loch, H Ma, S Menke, S Rajagopalan, D Rousseau, S Snyder, and G Unal. Calorimeter Clustering Algorithms: Description and Performance. Technical Report ATL-LARG-PUB-2008-002. ATL-COM-LARG-2008-003, CERN, Geneva, Apr 2008.

[29] Gavin P. Salam. Towards Jetography. *Eur.Phys.J.*, C67:637–686, 2010.

[30] Matteo Cacciari, Gavin P. Salam, and Gregory Soyez. The Anti-k(t) jet clustering algorithm. *JHEP*, 0804:063, 2008.

[31] Stephen D. Ellis and Davison E. Soper. Successive combination jet algorithm for hadron collisions. *Phys. Rev. D*, 48:3160–3166, Oct 1993.

[32] Yu.L. Dokshitzer, G.D. Leder, S. Moretti, and B.R. Webber. Better jet clustering algorithms. *Journal of High Energy Physics*, 1997(08):001, 1997.

[33] David Krohn, Jesse Thaler, and Lian-Tao Wang. Jet Trimming. *JHEP*, 1002:084, 2010.

[34] Commissioning of the ATLAS high-performance b-tagging algorithms in the 7 TeV collision data. Technical Report ATLAS-CONF-2011-102, CERN, Geneva, Jul 2011.

[35] Measurement of the b-tag Efficiency in a Sample of Jets Containing Muons with 5 fb^1 of Data from the ATLAS Detector. 2012.

[36] Measuring the b-tag efficiency in a top pair sample with 4.7 fb^{-1} of data from the ATLAS detector. Technical Report ATLAS-CONF-2012-097, CERN, Geneva, Jul 2012.

[37] Marc Lehmacher. b-Tagging Algorithms and their Performance at ATLAS. 2008.

[38] J.M. Butterworth, B.E. Cox, and Jeffrey R. Forshaw. WW scattering at the CERN LHC. *Phys.Rev.*, D65:096014, 2002.

[39] Georges Aad et al. Performance of jet substructure techniques for large-R jets in proton-proton collisions at $\sqrt{s} = 7$ TeV using the ATLAS detector. *JHEP*, 1309:076, 2013.

[40] Georges Aad et al. Performance of Missing Transverse Momentum Reconstruction in Proton-Proton Collisions at 7 TeV with ATLAS. *Eur.Phys.J.*, C72:1844, 2012.

[41] G. Aad et al. The ATLAS Simulation Infrastructure. *Eur.Phys.J.*, C70:823–874, 2010.

[42] S. Agostinelli et al. GEANT4: A Simulation toolkit. *Nucl.Instrum.Meth.*, A506:250–303, 2003.

[43] Torbjorn Sjostrand, Stephen Mrenna, and Peter Z. Skands. A Brief Introduction to PYTHIA8.1. *Comput.Phys.Commun.*, 178:852–867, 2008.

[44] Torbjorn Sjostrand, Leif Lonnblad, Stephen Mrenna, and Peter Z. Skands. Pythia 6.3 physics and manual. 2003.

[45] M. Bahr et al. Herwig++ Physics and Manual. *Eur. Phys. J.*, C58:639–707, 2008.

[46] Michelangelo L. Mangano, Mauro Moretti, Fulvio Piccinini, Roberto Pittau, and Antonio D. Polosa. ALPGEN, a generator for hard multiparton processes in hadronic collisions. *JHEP*, 0307:001, 2003.

[47] S. Catani, F. Krauss, R. Kuhn, and B.R. Webber. QCD matrix elements + parton showers. *JHEP*, 0111:063, 2001.

[48] T. Gleisberg, Stefan. Hoeche, F. Krauss, A. Schaelicke, S. Schumann, et al. Predictions for multi-particle final states with SHERPA. *Czech.J.Phys.*, 55:B529–B536, 2005.

[49] Stefano Frixione, Paolo Nason, and Carlo Oleari. Matching NLO QCD computations with Parton Shower simulations: the POWHEG method. *JHEP*, 0711:070, 2007.

[50] Stefano Frixione, Paolo Nason, and Bryan R. Webber. Matching NLO QCD and parton showers in heavy flavor production. *JHEP*, 0308:007, 2003.

[51] Johan Alwall, Pavel Demin, Simon de Visscher, Rikkert Frederix, Michel Herquet, et al. MadGraph/MadEvent v4: The New Web Generation. *JHEP*, 0709:028, 2007.

[52] Johan Alwall, Michel Herquet, Fabio Maltoni, Olivier Mattelaer, and Tim Stelzer. MadGraph 5 : Going Beyond. *JHEP*, 1106:128, 2011.

[53] B. P. Kersevan and E. Richter-Was. The Monte Carlo Event Generator AcerMC version 3.5 with interfaces to PYTHIA 6.4, HERWIG 6.5 and ARIADNE 4.1. *hep-ph/0405247*, 2008.

[54] Thorsten Chwalek. *Messung der W-Boson-Helizittsanteile in Top-Quark-Zerfllen mit dem CDF II Experiment und Studien zu einer frhen Messung des ttbar-Wirkungsquerschnitts mit dem CMS Experiment.* PhD thesis, Karlsruhe, U., Karlsruhe, 2010. Presented 12 Feb 2010.

[55] A.D. Martin, W.J. Stirling, R.S. Thorne, and G. Watt. Parton distributions for the LHC. *Eur.Phys.J.*, C63:189–285, 2009.

[56] Improved luminosity determination in pp collisions at $\sqrt{s} = 7$ tev using the atlas detector at the lhc. ATLAS-DAPR-2011-01-001, June 2012.

[57] Michiel Botje, Jon Butterworth, Amanda Cooper-Sarkar, Albert de Roeck, Joel Feltesse, et al. The PDF4LHC Working Group Interim Recommendations. 2011.

[58] Richard D. Ball, Valerio Bertone, Stefano Carrazza, Christopher S. Deans, Luigi Del Debbio, et al. Parton distributions with LHC data. *Nucl.Phys.*, B867:244–289, 2013.

[59] Johann H. Kühn, A. Scharf, and P. Uwer. Electroweak corrections to top-quark pair production in quark-antiquark annihilation. *Eur.Phys.J.*, C45:139–150, 2006.

[60] Johann H. Kühn, A. Scharf, and P. Uwer. Electroweak effects in top-quark pair production at hadron colliders. *Eur.Phys.J.*, C51:37–53, 2007.

[61] J.H. Kühn, A. Scharf, and P. Uwer. Weak Interactions in Top-Quark Pair Production at Hadron Colliders: An Update. 2013.

[62] Kyle Cranmer, George Lewis, Lorenzo Moneta, Akira Shibata, and Wouter Verkerke. HistFactory: A tool for creating statistical models for use with RooFit and RooStats. Technical Report CERN-OPEN-2012-016, New York U., New York, Jan 2012.

[63] RooStats's wiki. https://twiki.cern.ch/twiki/bin/view/RooStats/WebHome.

[64] RooFit's web page. http://root.cern.ch/drupal/content/roofit.

[65] Minuit2 Minimization Package wiki. http://seal.web.cern.ch/seal/MathLibs/Minuit2/html/.

[66] Glen Cowan, Kyle Cranmer, Eilam Gross, and Ofer Vitells. Asymptotic formulae for likelihood-based tests of new physics. *Eur.Phys.J.*, C71:1554, 2011.

[67] A L Read. Presentation of search results: the cl s technique. *Journal of Physics G: Nuclear and Particle Physics*, 28(10):2693, 2002.

[68] A. Wald. Tests of statistical hypotheses concerning several parameters when the number of observations is large. *Transactions of the American Mathematical Society*, 54(3):426–482, 1943.